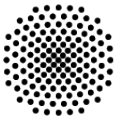

Universität Stuttgart SimTech

Tuning the properties and microstructuring of ionic liquid mixtures at surfaces through atomistic modeling

Von der Fakultät Mathematik und Physik sowie dem Stuttgart Research Centre for Simulation Technology (SimTech) der Universität Stuttgart zur Erlangung der Würde eines Doktors der Naturwissenschaften (Dr. rer. nat.) genehmigte Abhandlung.

Vorgelegt von

Takeshi Kobayashi

aus Kobe, Japan

Hauptberichterin:	Prof. Dr. Maria Fyta
Mitberichter:	Prof. Dr. Johannes. Kästner
Mitberichter:	Prof. Dr. Andreas Heuer

Tag der mündlichen Prüfung: 6.10.2021

Institute for Computational Physics
Universität Stuttgart

2021

Publication list

The following papers are published through the study in this thesis.

1. T. Kobayashi, A. Kemna, M. Fyta, B. Braunschweig and J. Smiatek, "Aqueous Mix-tures of Room-Temperature Ionic Liquids: Entropy-Driven Accumulation of Water Molecules at Interfaces", *J. Phys. Chem. C*, 2019, **123, 22**, 13795–13803

2. N. von Aspern, D. Diddens, T. Kobayashi, M. Börner, O. Stubbmann-Kazakova, V. Kozel, GV. Röschenthaler, J. Smiatek, M. Winter, and I. Cekic-Laskovic, "Fluorinated Cyclic Phosphorus(III)-Based Electrolyte Additives for High Voltage Application in Lithium-Ion Batteries: Impact of Structure-Reactivity Relationships on CEI Formation and Cell Performance", *ACS Appl. Mater. Interfaces* 2019, **11, 18**, 16605–16618

3. N. von Aspern, M. Leissing, C. Wölke, D. Diddens, T. Kobayashi, M. Börner, O. Stubbmann-Kazakova, V. Kozel, GV Röschenthaler, J. Smiatek, S. Nowak, M. Winter and I. Cekic-Laskovic, "Non-Fluorinated Phosphorus(III)-Based Electro-lytes for Advanced Lithium-Ion Battery Performance", *ChemElectroChem* 2020, **7**, 1499 – 1508

4. T. Kobayashi, H. Kraus, N. Hansen and M.Fyta, "Confined Ru-catalysts in a Two-phase Heptane/Ionic Liquid Solution: Modeling Aspects", *ChemCatChem* 2021, **13**, 739 – 746

5. T. Kobayashi, J. Smiatek and M. Fyta, "Energetic arguments on the microstructural analysis in ionic liquids" , *Adv. Theory Simul.* 2021, **4**, 2100104

Abstract

Ionic liquids (ILs) have been known to be environmental friendly, and chemically/thermally stable media for many applications. However, in order to use them in practical applications, further studies are needed, since their properties change significantly depending on the conditions such as IL species used, solute species and concentration added into them, temperature, pressure, and their interactions with surrounding entities. The experimental studies can provide the information, which is directly related to practical applications such as, for example, what kind of solute should be added to achieve a good operating voltage in supercapacitors or rechargeable batteries. However, it may require many trial and error investigations to reach reasonable conclusions regarding the best conditions for selected applications. In order to avoid this, statistical theories based on molecular or atomistic descriptions can be used to rationalize or deduce conclusions. However, the atomistic details, which are the input for

the theories, are usually difficult to obtain directly by experiments. Thus, with the help of the recent advance in computer devises and computational methods, computer simulations have been attracting intensive research attentions since they can generate the data or ensemble for the theories in order to obtain the experimental observable.

In this thesis, the focus is given on computational studies on the properties and microstructuring of the IL mixtures at surfaces in IL mixtures by means of Molecular Dynamics (MD) simulations. These are especially relevant to applications such using electrolytes in rechargeable batteries or as reaction media in catalysis. In order to obtain the basic idea of IL-solute mixtures, the study starts with simple bulk configurations of the mixtures of 1-Ethyl-3-methylimidazolium dicyanamide ($[EMIM]^+[DCA]^-$) as IL and water or dimethylsulfoxid (DMSO) as solute. The focus is given on the microstructural change in IL mixtures with respect to the solute concentration. The comparison between different approaches, namely the Kirkwood-Buff theory and the effective interaction energy reveals a good agreement between them, which also agrees with experimental observations. This way, this study highlights the potential of simulations in explaining the microstructural change in IL-solute mixtures.

Thereafter, the study moves to the IL mixtures in a confinement between flat neutral surfaces with no electrical charge, where the focus is given on the dependency of microstructuring of IL-water mixtures in front of the surface on the concentration of water and the IL species. Specifically, three different

ILs, namely $[EMIM]^+[DCA]^-$, 1-Ethyl-3-methylimidazolium tetrafluoroborate ($[EMIM]^+[BF_4]^-$) and 1-Butyl-3-methylimidazoliumtetrafluorborat ($[BMIM]^+[BF_4]^-$), are studied in order to elucidate how the difference in the cation or anion of IL affects the microstructuring. For this purpose, the translational order parameter is introduced for the entropy estimation. The results reveal that there is a strong correlation between the molecular size/shape and the hydrophobicity of the IL species, and the accumulation of the molecules at the interface. The study is further extended to the ILs-water/DMSO mixtures in confinement between charged surfaces. There, the influence of the surface charge on the microstructuring of $[EMIM]^+[DCA]^-$ and water/DMSO mixtures is discussed. For this purpose, the Lattice-gas model is introduced for the entropy estimation. The result reveals that there is a strong correlation between the excess entropy and the accumulation of the molecules at the interface. These studies are aimed to elucidate the mictrostructuring of the IL mixtures with solutes which are miscible with ILs, such as water or DMSO.

Finally, the investigations in this thesis moves to more complex applications, such as the heterocatalysis in a supported ionic liquids phase (SILP), where catalytic molecules are immobilized in the 1-Butyl-3-methylimidazolium trifluormethansulfonat ($[BMIM]^+[OTF]^-$) phase within biphasic IL and IL-immiscible heptane layers formed on top of the wet functionalized surface of silica nanopores. The purpose is to reveal the microstructural and dynamical properties of molecules which is relevant to the high performance in catalytic reactions in this template. The results indicates that a

flexible material design is possible concerning where the catalytic reactions occur. To this end, this study will contribute to elucidate the hidden microscopic pictures of molecular interactions in novel IL mixtures which otherwise is not directly accessible by experiments.

These studies will be further extended by choosing different combinations of IL species and solute molecules, which will make the outcomes more robust or be improved. Furthermore, the detailed analysis on the dynamic properties of the molecules, such as the accumulation dynamics of the molecules at the interfaces and the diffusion of the molecules within mesoporous media. By combining the static properties and the dynamic properties, clear view toward the optimal material design will be achieved. For that, an extensive collaborative research of experiments, simulations and theory is expected.

Overall, the information obtained within the framework of this doctoral dissertation is essential in designing the optimal conditions in IL mixtures in view of selected applications. The investigations carried out here provide a combined computational and analytic approach that provides a deep insight of such complex mixtures. This insight is not accessible by experiments, but can provide input for designing relevant experiments. Accordingly, this thesis paves the way for more detailed investigations in the field of ionic liquid solutions for novel complex applications.

Zusammenfassung

Ionische Flüssigkeiten (ILs) sind als umweltfreundliche und chemisch/thermisch stabile Medien für viele Anwendungen bekannt. Für ihren Einsatz in der Praxis sind jedoch weitere Studien erforderlich, da sich ihre Eigenschaften je nach den verwendeten IL-Spezies, den gelösten Spezies und der Konzentration, die ihnen zugesetzt werden, der Temperatur, dem Druck und den Wechselwirkungen mit der Umgebung erheblich verändern. Die experimentelle Untersuchungen können Informationen liefern, die für praktische Anwendungen unmittelbar relevant sind. Diese Informationen beziehen sich, zum Beispiel, auf der Art von gelösten Stoffen die hinzugefügt werden sollte, um eine gute Betriebsspannung in Elektrolyt-basierten Batterien zu erreichen. Dennoch kann es viele Versuche und Irrtümer erfordern, um einer aussagekräftige Schlussfolgerung für die beste Bedingung für ausgewählten Anwendungen zu treffen. Um dies zu

vermeiden, können statistische Theorien auf der Grundlage molekularer oder atomistischer Beschreibungen verwendet werden, um die Schlussfolgerung zu rationalisieren oder abzuleiten. Allerdings sind die atomistischen Details, die den Theorien zugrunde liegen, in der Regel nur schwer durch Experimente ermittelbar. Mit den jüngsten Fortschritten bei den Computergeräten und Berechnungsmethoden bieten Computersimulationen daher eine sehr gute Alternative. Diese können die Daten oder das Ensemble für die Theorien generieren, um die experimentellen Observablen zu erhalten. In dieser Arbeit liegt der Schwerpunkt auf einer rechnerischen Untersuchung der Eigenschaften und der Mikrostrukturierung von IL-Gemischen an Oberflächen mit Hilfe von Molekulardynamiksimulationen (MD), was besonders für Anwendungen wie Elektrolyte in wiederaufladbaren Batterien oder Reaktionsmedien in der Katalyse relevant ist.

Um eine grundlegende Vorstellung von IL-Gemischen zu erhalten, beginnt die Studie mit einfachen Bulk-Konfigurationen von Gemischen aus 1-Ethyl-3-methylimidazoliumdicyanamid ($[EMIM]^+[DCA]^-$) als IL und Wasser oder Dimethylsulfoxid (DMSO) als gelöster Stoff. Die Wechselwirkung von ionischen Flüssigkeiten (IL) mit Zusatzstoffen oder Verunreinigungen ist entscheidend für die Leistung von IL in technologischen Anwendungen. Um die Wechselwirkung zwischen diesen zu verstehen, ist ein Einblick in die mikroskopische Anordnung der Moleküle erforderlich. Daher liegt der Schwerpunkt auf der mikrostrukturellen Veränderung in IL-Mischungen in Abhängigkeit von der Konzentration der gelösten Stoffe. Es werden verschiedene

molare Anteile von DMSO und Wasser untersucht, um den Einfluss der Konzentration der gelösten Moleküle auf die Strukturierung der ILs zu klären. Zu diesem Zweck werden Kirkwood-Buff-Integrale (KBI) und effektive Wechselwirkungsenergien berechnet, um die Veränderung der Ionenstrukturen in Abhängigkeit von der Konzentration der gelösten Stoffe zu beschreiben. Der Vergleich zwischen verschiedenen Ansätzen, nämlich der Kirkwood-Buff-Theorie und der effektiven Wechselwirkungsenergie, zeigt eine gute Übereinstimmung zwischen ihnen, die auch mit experimentellen Beobachtungen übereinstimmt. Die Ergebnisse zeigen, dass DMSO-$[EMIM]^+[DCA]^-$- und Wasser-$[EMIM]^+[DCA]^-$-Gemische durch recht unterschiedliche molekulare Wechselwirkungen zwischen den Spezies definiert sind. Erhöht man die DMSO- oder Wasserkonzentration, so werden die gelösten Moleküle von den Ionen abgestoßen, während sie sich in letzterem Fall näher an den Ionen ansammeln. Die Unterschiede ergeben sich aus der Schwächung der Wechselwirkungen zwischen den Ionen durch die Anwesenheit von Wassermolekülen, während DMSO eine Verstärkung dieser Wechselwirkungen bewirkt. Dementsprechend liefert diese Studie ein tiefes Verständnis des IL-Verhaltens in Kombination mit neutralen gelösten Molekülen und ermöglicht eine angemessene Auswahl von IL-Lösungs-Kombinationen im Hinblick auf spezifische technologische Anwendungen.

Die Fortsetzung der Studie fokusiert auf IL-Mischungen zwischen flachen neutralen Oberflächen ohne elektrische Ladung. Hier liegt der Schwerpunkt auf der Abhängigkeit der Mikrostrukturierung von IL-Wasser-Mischungen

vor der Oberfläche von der Wasserkonzentration und der IL-Spezies. Konkret werden drei verschiedene ILs, nämlich $[EMIM]^+[DCA]^-$, 1-Ethyl-3-methylimidazoliumtetrafluoroborat ($[EMIM]^+[BF_4]^-$) und 1-Butyl-3-methylimidazoliumtetrafluorborat ($[BMIM]^+[BF_4]^-$) untersucht, um zu klären, wie Unterschiede im Kation oder Anion der IL-Spezies die Mikrostrukturierung beeinflusst. Zu diesem Zweck wird der translatorische Ordnungsparameter für die Entropieschätzung eingeführt. Die Ergebnisse zeigen eine entropiegetriebene Anreicherung von Wassermolekülen vor Grenzflächen mit geringen, aber technologisch relevanten Unterschieden. Es zeigt sich, dass es eine starke Korrelation zwischen der Molekülgröße/-form und der Hydrophobizität der IL-Spezies und der Akkumulation der Moleküle an der Grenzfläche gibt. Die lokale Wasserdichte hängt entscheidend vom Wassermolanteil, von lokalen Ordnungseffekten und von der Molekularstruktur der ionischen Flüssigkeiten (IL) ab. Die Ergebnisse dieser Studie ermöglichen die Definition zuverlässiger Kriterien für vorteilhafte Wasser-IL-Kombinationen im Hinblick auf verschiedene Anwendungen.

Die Studie wird weiter auf die ILs-Wasser/DMSO-Gemische im Einschluss zwischen geladenen Oberflächen ausgedehnt. Konkret werden 1-Ethyl-3-methylimidazoliumdicyanamid ($[EMIm]^+[DCA]^-$) mit Wasser- oder Dimethylsulfoxid (DMSO)-Gemischen im Einschluss zwischen zwei Grenzflächen untersucht. Die Analyse basiert auf dem Vergleich der beteiligten molekularen Spezies und des Ladungszustands der Oberflächen, die entweder positiv oder negativ geladen sind. Der Schwerpunkt liegt auf dem Einfluss un-

terschiedlicher Wasser/DMSO-Konzentrationen auf die Mikrostrukturierung und die Anreicherung der einzelnen Spezies, nämlich Kationen, Anionen und gelöste Stoffe. Thermodynamische Aspekte, wie zum Beispiel. die entropischen Beiträge zu den beobachteten Trends, werden aus den Simulationen unter Verwendung einer Gittergastheorie gewonnen. Die Ergebnisse unterstreichen deutlich die Unterschiede in diesen Eigenschaften für Wasser- und DMSO-Gemische und enthüllen die zugrunde liegenden Mechanismen und inhärenten Details. Die Bedeutung der Größe und der dielektrischen Eigenschaften der Moleküle bei der Steuerung ihrer Mikrostrukturierung vor den Oberflächen sowie ihre Wechselwirkungen mit letzteren, d. h. die Wechselwirkungen zwischen Lösung und Oberfläche wird hervogehoben. Die Analyse der molekularen Akkumulation an den Grenzflächen ermöglicht es uns vorherzusagen, ob die Akkumulation entropie- oder enthalpiegetrieben ist, was sich auf die Entfernung der molekularen Spezies von den Oberflächen auswirkt. Durch unsere Analyse lassen sich makroskopische Eigenschaften wie der elektrochemische Potenzialabfall an den Grenzflächen und die Bedingungen für die Beibehaltung eines stabilen elektrochemischen Fensters ermitteln. Das Ergebnis zeigt, dass es eine starke Korrelation zwischen der Überschussentropie und der Anhäufung von Molekülen an der Grenzfläche gibt. Diese Untersuchung zielt darauf ab, die Mikrostrukturierung von IL-Mischungen mit gelösten Stoffen, die mit ILs mischbar sind, zu untersuchen. Die Studie ist von großer Bedeutung, da sie ein grundlegendes Verständnis für die effiziente und gezielte Entwicklung von elektrochemischen Elementen liefert.

Schließlich geht die Arbeit zu einem Beispiel für realistische Anwendungen über, nämlich der Katalyse in einer unterstützten ionischen Flüssigkeitsphase (SILP). Hier werden katalytische Moleküle in der 1-Butyl-3-methyl-imidazoliumtrifluormethansulfonat-Phase ($[BMIM]^+[OTF]^-$) innerhalb von zweiphasigen IL- und IL-unmischbaren Heptan-Schichten immobilisiert werden, die auf der nassen funktionalisierten Oberfläche von Siliziumdioxid-Nanoporen gebildet werden. Es wird ein Modellierungsansatz für atomar aufgelöste Studien von katalytischen Systemen in mesoporösem Siliziumdioxid mit Hydroxyl- und funktionellen Gruppen an der Oberfläche vorgeschlagen. Ziel ist es, die mikrostrukturellen und dynamischen Eigenschaften der Moleküle aufzudecken, die für die hohe Leistung bei katalytischen Reaktionen in dieser Vorlage relevant sind. Zunächst wird ein Kraftfeld für den Ru-basierten divalenten Katalysator entwickelt. Zweitens wird sein Solvatationsverhalten in einem Zweiphasensystem aus Heptan und IL untersucht. Drittens werden die statischen und dynamischen Eigenschaften des eingeschlossenen Systems analysiert. Mit Hilfe klassischer Molekulardynamiksimulationen können auf dieser Art experimentell nicht zugängliche Eigenschaften untersucht werden, die für eine Optimierung eines SILP-Systems zur Durchführung einer ringschließenden Metathesereaktion wichtig sind. Die Ergebnisse zeigen, dass ein flexibles Materialdesign für die katalytischen Reaktionen möglich ist. Zusammenfassend, wird diese Doktorarbeit dazu beitragen, die verborgenen mikroskopischen Abbildungen der molekularen Interaktionen in neuartigen IL-Mischungen zu erläutern, die sonst nicht direkt durch

Experimente zugänglich sind. Die durch diese Arbeit gewonnenen Informationen, sowie die Modellierungsaspekte und analytische Methoden, können dazu verwendet werden, die optimalen Bedingungen für die IL-Mischungen für ausgewählte Anwendungen zu erläutern und definieren.

Contents

Listing of figures

List of Tables

Acknowledgments

Throughout the research for this dissertation I have received a great deal of support and assistance. I would first like to thank my supervisor, Apl. Prof. Maria Fyta, whose patience and kindness have been always navigating me to a right direction since I started my master's thesis in her group. You gave me a freedom to sharpen my thinking, which brought my work to a higher level.

I would also like to greatly thank my second supervisor, Priv.-Doz. Dr. Jens Smiatek, whose broad knowledge and the enthusiasm has encouraged and motivated me to be actively engaged in this subject during my master's and PhD study.

I would like to acknowledge my colleagues at Institute for Computational Physics at University of Stuttgart for their wonderful collaboration. I would particularly like to single out the head of our institute, Prof. Christian Holm, who gave me a lot of opportunity to have fruitful discussion inside and outside of our group. My colleagues always create inspiring but also friendly environment of our institute, which has brought me an exciting and comfortable life here.

I would also like to thank my external collaborators outside of our Institute, Dr. Seishi Shimizu, Joshua. E. S. J. Reid, Andre Kemna, Prof. Björn Braunschweig, Natascha von Aspern, Hamzeh Kraus, Apl. Prof. Niels Hansen, Felix Ziegler, and Prof. Michael Buchmeiser for their valuable work throughout my studies. It was a great pleasure for me to obtain different view points by interacting with you. I also would like to thank Prof. Johannes Kästner and Prof. Andreas Heuer for accepting the role of the reporter of my thesis, and Prof. Martin Dressel for accepting the role of the head of my defense committee.

Financial funding is gratefully acknowledged from the Deutsche Forschungsgemeinschaft through the SFB 716 and SFB 1333, and also the department of Physics at the University of Stuttgart.

I would also like to thank my classmates and friends, who has supported me and made my life in Germany always exciting and very comfortable.

In the end, I would like to thank my parents, my brother, and my grand parents for their patience, understanding, and a great care of me to let me come to Germany for studying. You are always there for me. I could not have completed this dissertation in Germany without the support of you.

The research in this thesis was carried out in the framework of the Graduate School Simulation Technology (GS Simtech). Part of the sentences in this thesis is reproduced from (T. Kobayashi, J. E. S. J. Reid, S. Shimizu, M. Fyta and J. Smiatek, *Phys. Chem. Chem. Phys.*, 2017, **19**, 18924 DOI: 10.1039/C7CP03717A)[104] with permission from the PCCP Owner Societies ,and under the copyright 2021 Wiley, used with permission from (T. Kobayashi, H. Kraus, N. Hansen, M. Fyta, *ChemCatChem* **2021**, 13, 739)[102] ,and under the copyright 2021 Wiley, used with permission from (Kobayashi, T., Smiatek, J. and Fyta, M. (2021), Energetic Arguments on the Microstructural Analysis in Ionic Liquids. Adv. Theory Simul., 4: 2100114. https://doi.org/10.1002/adts.202100114)[105] ,and reprinted with permission from (T. Kobayashi , A. Kemna, M. Fyta, B. Braunschweig, and J. Smiatek, *J. Phys. Chem. C* 2019, 123, 22, 13795−13803)[103] under the opyright 2019 American Chemical Society.

Abbreviation list

IL(s)	:	Ionic liquid(s)
RTIL(s)	:	Room temperature ionic liquid(s)
DMSO	:	Dimethylsulfoxid
MD simulation	:	Molecular dynamics simulation
IF(s)	:	Interface(s)
DFT	:	Density functional theory
KS ansatz	:	Kohn-Sham ansatz
KS equation	:	Kohn-Sham equation
LDA	:	Local density approximation
GGA	:	Generalized gradient approximation
KB theory	:	Kirkwood-Buff theory
KBI(s)	:	Kirkwood-Buff integrals(s)
rdf(s)	:	Radial distribution function(s)
PMF(s)	:	Potential of mean force(s)
$[EMIM]^+$	:	1-Ethyl-3-methyl-imidazolium
$[BMIM]^+$	:	1-Butyl-3-methylimidazolium
$[DCA]^-$	:	Dicyanamide
$[BF4]^-$	:	Tetrafluoroborat
$[OTF]^-$	:	Trifluormethansulfonat
SILP	:	Supported ionic liquid phase

1

Introduction

Ionic Liquids (ILs) are multipurpose liquids which constitute of complex combination of cations and anions like normal salts such as sodium chloride (NaCl). What makes them different from normal salts is the fact that they can stay in a liquid state under relatively low temperature (~150°C) compared to the normal salts (~800°C for NaCl). Especially, ILs which can

stay in a liquid state under room temperature are called room temperature ionic liquids (RTILs). ILs have been long studied due to their potential use for a wide range of technological applications[59]. These applications range from electrolytes, fuel cells, batteries, carbon captures, etc[56,61,60]. The first IL (ethanolammonium nitrate) was reported back in 1888[69] and then in 1914 first RTIL (ethylammonium nitrate) was reported[211]. Despite these early finding of ILs and RTILs, the air stable and water stable 1-ethyl-3-methylimidazolium ($[EMIM]^+$) based RTILs were first invented in 1992[224]. After then, much attention was put on the ILs, and the research on ILs are now still growing and attracting the attentions from the point of views of the wide range of applications in biology, electrochemistry, environmental study and engineering, etc. One of the important applications of ILs is the electrolytes in rechargeable batteries such as Lithium ion batteries. Moreover, as another important application ILs are used as reaction solvents in catalytic reactions. Therefore, the study in this thesis is purposed in view of these applications.

There are two subsets of ILs. One is protic ILs (PILs) and the other is aprotic ILs (AILs). PILs are made by mixing of a Brønsted acid and a base, such as ethylammonium nitrate ($[C_2H_5NH_3]^+[NO_3]^-$) and ethanolammonium nitrate ($[HOC_2H_4NH_3]^+[NO_3]^-$). The proton moves from the acid to the base to form the cation and the anion. After the synthesis of these acid and base, water is removed to purify the ILs. Therefore, the producing process is simple. PILs are expected to be useful, for instance, as proton conductors in fuel cells[118,141]. On the other hand, AILs substitute the protonic site in the PILs by

other groups, typically alkyl groups, and the synthesis is not as simple as PILs. The detail of synthesis methods can be found in Ref.[217]. Common cations for AILs are imidazolium such as 1-ethyl-3-methylimidazolium ($[EMIM]^+$), pyrrolidinium such as 1-Butyl-1-methylpyrrolidinium ($[Pyr_{14}]^+$) , quatenary ammonium such as bis(2-ethylhexyl)dimethylammonium ($[BEDEMA]^+$) and piridinium such as 1-butyl-4-methylpyridinium ($[B4MPY]^+$), etc. Common anions are hexafluorophosphate ($[PF_6]^-$), tetrafluoroborate ($[BF_4]^-$), bis(trifluoromethylsulfonyl)imide ($[TFSI]^-$), etc. These AILs are extensively studied in view of the application as the electrolytes in lithium ion batteries[132].

The basic properties of ILs are low flammability, low volatility and also thermal stability. These features made ILs be considered as good alternatives to conventional organic solvents which are usually toxic and flammable[58]. The other advantage of ILs over other solvents is that depending on the combination of cations and anions, the thermal properties like viscosity, melting point, glass transition can be fine tuned[59]. These are just a few aspects of the variety of technological and industrial applications of ILs. The study on these applications is in progress and at the same time study on the basic mechanism behind these applications and the relevant restrictions[31,91,80,96,97,214,185,89,138].

Here, some advantages and some relevant questions or difficulties which should be addressed are listed,

- thermal stability - identifying melting points and boiling points, elucidating the dependency of properties on temperature

- chemical stability - to what extent they are stable for specific purpose, for example, for the electrolytes in fuel cells
- low volatility - difficulty in distillation, leads to the difficulty in purification
- low toxicity - identifying the remaining toxicity and how toxic it is
- solubility - which ILs solvate inorganic solutes and which ILs solvate organic solutes

In order to answer all these questions above, an interplay of experimental, theoretical and computational study is essential, and elucidating the hindered microscopic mechanisms is the crucial task for the optimal design of ILs for specific purposes.

Focusing on the chemical stability and the solubility, one of the restrictions is the miscibility with water. Regarding the water solubility, ILs can be classified into hydrophobic or hydrophilic ILs. Generally speaking, hydrophobicity or hydrophylicity is controlled by the choice of the anion. For example, $[BF_4]^-$ and $[Cl]^-$ are thought to be hydrophilic, on the other hand, $[TFSI]^-$ and $[PF6]^-$ are thought to be hydrophobic[85]. However, the choice of the cation also affects the overall hydorophobicity/hydrophylicity of ILs[82,20]. Even the hydrophobic ILs show some water affinities[85], and because of the high affinity of ILs with water, some water molecules can be mixed in during production or application process[57]. It is reported that even a small portion of water can affect negatively the expected properties of ILs[220,221].

In view of the use for electrolytes, the residual water decreases the viscosity of ILs[222], which leads to the increase of conductivity[223]. These are the positive side of the water molecules in IL solutions. On the other hand major drawback is narrowing the electrochemical windows. In Ref.[177], the narrowing in both anodic and cathodic potential is reported with the narrowing of total $\approx$ 1.5 V for 1-butyl-3-methylimidazolium tetrafluoroborate ($[BMIM]^+[BF_4]^-$) in presence of wgt.3% of water. Therefore, investigation on the mechanism of the influence of water molecules on the structure of IL-water mixture is a crucial task to realize the practical use of ILs as electrolytes. Compared to water, DMSO is also polarized but aprotic which means that there is only little proton transfer (hydrogen bonds) between ILs and solutes, although there is still possibility to form weak hydrogen bonds between ILs and DMSO[199]. The IL-DMSO mixures are also extensively studied due to its chemical stability[4,90,213,124,162,235,199]. These studies highlight that the water can change the ionic structure by well dissolving the ions while DMSO does keep the ionic structures. Thus, one can expect that there is a distinct difference in the microscopic structure between water and DMSO, even though both are still mixable with ILs. The study on the different solutes (water/DMSO) provide us with an insight about whether we should use water or DMSO, in other words protic or aprotic solutes for specific purposes.

Now the question is why and how solute molecules (water/DMSO) affect the properties of ILs, in other words, how water/DMSO molecules

behave in ILs and affect the structures of ILs. There have been several studies on the effect of water molecules in ILs. In Ref.[180], regarding the miscibility with water, it is pointed out that ILs with $[BF4]^-$ as the anion can be both water soluble and insoluble depending on the cation. And it is said that the longer the alkyl chain of the cation is, the less the solubility of water is. In Ref.[77], the computer simulations are performed for IL-water mixtures at $x_{H_2O} = 0.25, 0, 50, 0.75$. It is shown that at $x_{H_2O} \leq 0.50$, 40% of the water molecules are isolated each other and no large water clusters or channels are observed. Even at $x_{H_2O} = 0.75$, 20-30% of water molecules are still isolated each other, but at the same time water channels starts to form. Other computer simulations show that at high water mole fractions $x_{H_2O} > 0.80$, the structure of ILs is destroyed by water clusters, and this leads to the strong increase of diffusivity of the IL-water mixture[91]. An Experimental result shows that at $x_{H_2O} = 0.10$, the small water clusters start to form and grow till $x_{H_2O} = 0.70$. There, the formation of large scale water clusters starts to disturb the structure of ILs[63]. Also, in Ref.[31], it is noted that in the dilute range of water content in RTILs, most of the water molecules don't form clusters, but bind anions forming anion-water-anion bridge. As a whole, there are two questions which should be answered. Regarding the behavior of water molecules, the question is if water molecules dispersed or clustered in ILs as discussed in Ref.[44,126]. And regarding the effect of water molecules, the question is if water molecules weaken the structure of ILs as discussed in Ref.[62]. Regarding the influence of DMSO, experimentally it is proposed

that DMSO forms weak hydrogen bonds with $[EMIM]^+$ cations when bis(trifluormethylsulfonyl)imid ($[TFSI]^-$) is used as the anion. Increasing the concentration of DMSO leads to loosing the cation-anion interaction due to these hydrogen bonds between DMSO and cations [199]. Further experimental study which compares water and DMSO revealed that adding DMSO into $[BMIM]^+[Cl]^-$ strengthen the cation-anion interaction [162]. In Ref. [124], the same conclusion is drawn by comparing water and DMSO-IL mixtures discussing the influence on the diffusion behavior of ions in the solutions. It is often said that the anion species mainly affect the IL properties. However, in the combined study of simulation and experiment pointed out that there is also the influence of the difference in cations [213]. The computational study also highlights that there is not much difference in the interactions of DMSO with cations and anions while water shows much stronger interaction with anions than with cations [235].

All the research mentioned above aims to elucidate the bulk properties of IL-solute mixtures. However, in practical applications, we have to consider the confinement effect in which the interfaces (IFs) between IL solutions and the other materials such as electrodes, protein/DNA or nanopores exist and thus, the performance of the ILs highly relies on the properties of IL solutions at these IFs [231,64,87,164,26,55].

In more detail, previous computational and experimental studies reported that water accumulate at IFs at highly charged electrodes, which

invoke electrochemical decomposition processes and hence cause a significant degradation of electrochemical cells[64,43,123]. In contrast to this disadvantage, the advantage of the accumulation of water at IFs at silver electrodes was shown to facilitate CO_2 electroreduction mechanisms, and accordingly a higher efficiency of degradation processes is established[165]. As a consequence, whether the occurrence of the accumulation of water molecules at charged or uncharged interfaces is considered as a desired or undesired effect depends highly on the specific technological purpose. So far these studies mentioned above are mostly done on the properties of low-concentrated solute molecules in ILs. However, also the opposite case of highly concentrated solutes in ILs has received considerable attention. As a representative example, a lot of research effort was devoted to aqueous or hydrated ILs, which either increase or decrease the structural stability of proteins[38,135,39,148,234,181,187,122,144,173]. Recent explanations for these use preferential binding and exclusion mechanisms at IFs in terms of a statistical thermodynamics[187,49,144]. With regard to previous theoretical, numerical, and experimental approaches for solute-IL mixtures at various mixing ratios[180,6,225,91,176,174,195,182,175,232,32,10,80,35,161,201,17,119,121,120,160,104,145,64,215,43,93], the question is whether the accumulation of water molecules occurs only at charged IFs[64,43,93] or whether it can also occur at uncharged IFs. Moreover, what causes the structural differences for different IL-solute combination[93,133,134,50,163] is unclear. The answers to these questions pave a rational way towards an improved use of IL solutions for various technological

applications.

Specifically speaking, a very important manifestation of the structural change under confinement can be seen in the layering structures of IL solutions in front of IFs. Several layers in parallel to the surfaces are formed[29,53,129,228] due to the Coulomb or dispersion interactions between the surfaces and the molecules in the solutions. For RTILs mixtures, the type of solute can play a crucial, whether it is negative or positive, role on the RTIL properties. For a theoretical treatment of the layering of liquid solutions in front of charged surfaces, the "classical" Gouy-Chapman model was developed for dilute electrolyte mixtures for the electric double layer (EDL) in front of charged surfaces[36] . As this cannot be directly applied to the case of RTILs which is a concentrated electrolyte, several other theories based on the Gouy-Chapman theory have been developed to describe concentrated RTIL capacitors[107]. The presence and influence of neutral solutes (or solvents) is typically included in the theory through a background permittivity or a void not accessible by the ions[230].

Although, these theories could provide some insight on IL solutions, still many effects governed by the atomistic details are missing. On the atomistic scale, the charges are also carried by the atoms in the neutral species. This occurs especially at IFs, where either positively or negatively charged atoms can accumulate. In order to cover the gap and compare to the Gouy-Chapman based theories, computational study by means of all-atom Molecular Dynam-

ics (MD) simulations is needed. Through a comparison of different solutes, namely water or DMSO at different concentrations, the influence of the solute on the microstructural characteristics of the IL solution in front of charged surfaces can be further analyzed in addition to the results from the previous attempts[231,164,87,85,148,3]. Specifically, the distinct features in the molecular distributions, clustering of the solutes, and the interactions of the solutes with the IFs in terms of the enthalpic or entropic effect should be clarified as a fundamental level of understanding. For this purpose, the results from the MD simulations can be used and compared the Lattice-gas model[107], which approaches the IL mixtures through a free energy ansatz. This theory can be extended to also include the distribution of molecules in front of the neutral surfaces.

These fundamental studies mentioned above are aimed to elucidate the microscopic behavior of ILs-solute mixtures in bulk or confinement in relatively simple configurations, which highlights the fundamental properties of IL solutions. In this thesis, the study goes further in view of practical applications which consist of multiple components including bulk, surface, solutes and solvents. As a representative technological application, the ILs in catalysis is studied in this thesis. The advantage of the confinement in the catalytic reactions has been discussed in last few years, where the catalytic reaction rate or selectivity is enhanced by the distinct heterogeneous geometry, which consists of mesoporous silica materials with surface-anchored functional groups[74,127,212]. A specific example is an immobilized Rh-complex on SBA-15 particles, where 1-octene hydroformulation rate was enhanced compared to the homogeneous

analogue. The explanation for this was given as the suppression of the formation of inactive forms of the catalyst inside the pores[128]. Other examples are olefin or cyclooctane metathesis reactions carried out in mesoporous silica materials[25,156] or synergetic effects between multifunctional groups anchored in close proximity in confined spaces[229], which show high selectivity. Selectivity and conversion of reactions can be highly affected by the spatial distribution and the mobility of reactants and products which may be controlled by the various factors such as molecular size, shape, polarity, pore geometry, properties of the pore surface, and the interaction between the constituents of the system.

For the application and rational design of functionalized mesoporous materials, establishing a reliable model which can predict how pore dimension and surface functionalization influence the properties of the fluid under confinement is essential[18]. However, due to the complex interplay between the constituents in the mesoporous media, it is still a challenging task to experimentally observe the properties of fluids inside the pores such as the solvent composition and phase behavior. This makes it difficult to find an optimize or tune the configuration of the system. The dynamics of the molecules within the mesoporous media has a crucial importance in heterogeneous catalysis. It can be affected by various macroscale factors such as grain boundaries and particle packing, as well as by mesoscale factors such as particle size and connectivity of pores. These factors are in the end built uopn the microscale factors such as the atomic level interaction between the constituents[84].

Therefore, there is a growing interest in computational modeling studies of relevant systems in order to provide a fundamental molecular-level description of confinement effects[78,71,100,66,233,21,86,98,150]. These studies contributed to an unified description of diffusion inside porous media[110] or to rationalizing the effect of surface chemistry on olefin metathesis in confined geometries[236]. Among the mesoporous catalysts, an important example is supported ionic liquid phase (SILP) catalysis[46,209,125,216,52,13,207,151,67,79]. MD simulations could allow us to provide a fundamental insight into SILP catalysis, relevant for electrochemical systems or the water-gas shift reaction[24,198,210]. Due to the complexity of the system, coarse-grained models can be used in order to run significantly larger length and time scales than models with atomistic resolution[72,7,200]. Nevertheless, It is still essential to further extend the microscopic knowledge by increasing the complexity of the studied systems in an atomistic scale. Thus, in this thesis a study of a linker-free incorporation of a Ru-based catalyst inside a wet functionalized mesoporous media filled with a two phase fluid consisting of heptane and an ionic liquid is carried out. To this end, the above mentioned studies provide an insight on the microscopic description of the relevant technological applications. This leads to the optimal tuning of the parameters relevant to the performance of the system involving ILs at the surface, and efficient use of the materials which overcome the environmental problems in terms of re-usability, safety and the energy conversion efficiency.

2

Computational Methods

In this chapter, the computational methods used in this study are outlined. In section 2.1, the basics of the Molecular Dynamics simulations are explained including the methods used in the simulations. In section 2.2, the concept of density functional theory (DFT) is introduced. Since the purpose of the DFT calculation in this study is limited to the generation of the input parameters

(force-field) of MD simulations, only the basics relevant to this is explained in detail.

2.1 Molecular Dynamics Simulations

Here, the basic idea or concept of Molecular Dynamics (MD) simulations is described in terms of the advantages as well as the limitation. There is other simulation methods such as Monte Carlo (MC) simulations. However, for the research carried out in this thesis where the dynamic properties of the system such as diffusion constant or ionic conductivity are relevant, MD simulations are the most useful tools.

Since the dynamics of a many-particle system which has more than three particles is in principle impossible to solve analytically, we have to use computer simulations. In MD simulations, particles follow the Newton's second law, $\mathbf{F}_i = m_i \mathbf{a}_i$, where $\mathbf{F}_i$, m_i and $\mathbf{a}_i$ denote the force, mass, and acceleration of the ith particle, respectively. The force $\mathbf{F}_i$ acting on the ith particle can be derived from the derivative of the potential V($\mathbf{x}$, t) with respect to the ith particle's position $\mathbf{x}_i$, which leads to the equation of motion of ith particle,

$$\mathbf{a}_i = \frac{d^2\mathbf{x}_i}{dt^2} = \frac{\mathbf{F}_i}{m_i} = -\frac{1}{m_i}\frac{dV(\mathbf{x},t)}{d\mathbf{x}_i} \tag{2.1}$$

Note that, the potential $V(\mathbf{x}, t)$ depends on the collective positions of all the particles $\mathbf{x}$ and also t when there are time-dependent external fields. The main task of MD simulations is to solve this equation of motion for all the atoms

involved in the dynamics. Accordingly, using the relation $\frac{d\mathbf{x}_i(t)}{dt} = \mathbf{v}_i(t)$ and $\frac{d\mathbf{v}_i(t)}{dt} = \mathbf{a}_i(t)$, integrating Eqn.(2.1) with respect to time yields the equation of motion of the system,

$$\mathbf{x}_i(t) = x_i(0) + \frac{d\mathbf{x}_i(t)}{dt}t \tag{2.2}$$

$$\mathbf{v}_i(t) = v_i(0) + \frac{d\mathbf{v}_i(t)}{dt}t, \tag{2.3}$$

where $\mathbf{x}_i(t)$ and $\mathbf{v}_i(t)$ are the position and velocity of ith particle at time t. The positions and velocities of the particles can be determined by giving the values of initial positions and velocities of ith particle $\mathbf{x}_i(0)$ and $\mathbf{v}_i(0)$ and the potential $V(\mathbf{x}, t)$.

The initial particle positions or the initial configuration can be specified in an empirical or a random way depending on the system. They can be also determined by using *ab initio* calculations which will be explained later in this chapter. The potential $V(\mathbf{x}, t)$, which is called a force field in MD simulations, can be also determined in an empirical way or by *ab initio* calculations. In the MD simulations, the interaction between particles are treated in a classical way using several approximations.

- A particle is treated as a point-like particle located at a certain point in space.
- A mass and electrical charge are assigned to this point-like particle.

- The interaction between particles are calculated by predefined interaction parameters which consist of bonded and non-bonded interaction parts.

Accordingly, the potential is divided into two part, bonded interactions part V_{bonded} and non-bonded interactions part $V_{\text{non-bonded}}$.

$$V_{\text{total}} = V_{\text{bonded}} + V_{\text{non-bonded}} \tag{2.4}$$

The bonded interactions are further divided into the bond, angle and improper/proper dihedral interactions as depicted in FIG.2.1. The non-bonded

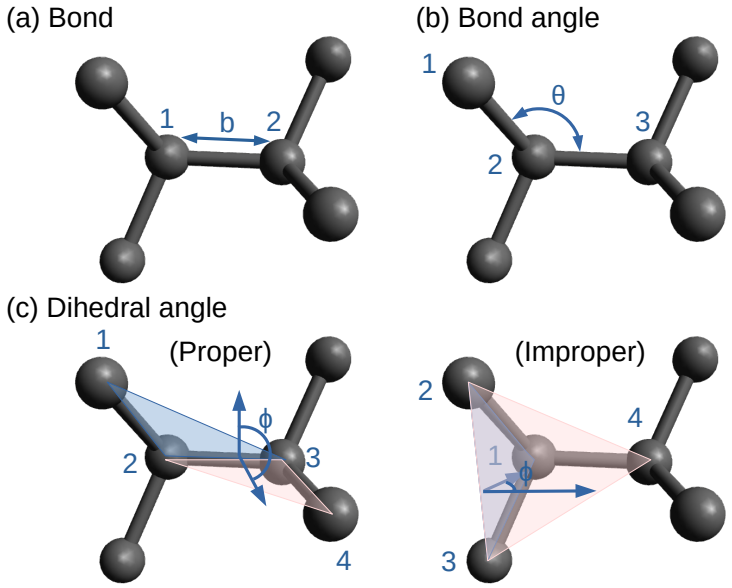

Figure 2.1: Schematic explanation of bonded interactions in a MD simulation. (a) Bond, (b) bond angle, (c) (left) proper dihedral angle, and (right) improper dihedral angle.

interactions are also divided into two parts. One is the Coulomb interaction, derived from the electrostatic interaction which is written as,

$$V_{\text{coul}}(r) = \frac{q_1 q_2}{4\pi\varepsilon_0 r} \tag{2.5}$$

where, q_1 and q_2 are the electronic charges of atom 1 and atom 2 respectively, ε_0 is the vacuum permittivity, and r is the distance between atom 1 and atom 2. The another is the dispersion interactions which stem from, for example, Van der Waals interactions. However, these description are also the approximation, which should be fitted to empirical data or *ab initio* calculations. Most commonly used potential for the dispersion interaction is Lenard-Jones (LJ) potential which is written as,

$$V_{\text{LJ}}(r) = 4\varepsilon \left[\left(\frac{\sigma}{r}\right)^{12} - \left(\frac{\sigma}{r}\right)^{6} \right] \tag{2.6}$$

where, ε and σ are fitting parameters which should be defined for each pair of atoms. There are different force fields which parameterize these potentials described above depending on the purpose or the system of study. Those parameters are quite system dependent, thus even for the same atoms or molecules, care should be taken about whether it is in liquid, gas, or solid state and the molecular combination of the system of interest. Once the potential is determined, the equation of motion Eqns.(2.1), (2.2), and (2.3) can be solved numerically.

2.1.1 The Leapfrog integration

In order to solve Eqns.(2.2) and (2.3) numerically, the leapfrog integration is used by following equations.

$$x_i(t+\Delta t) = x_i(t) + \Delta t v_i(t+\frac{1}{2}\Delta t) \quad (2.7)$$

$$v_i(t+\frac{1}{2}\Delta t) = v_i(t-\frac{1}{2}\Delta t) + \frac{F_i(t)}{m}\Delta t \quad (2.8)$$

Both positions and velocities are integrated by time step Δt, but the velocity used for the position calculation is shifted by $\frac{1}{2}\Delta t$. In a same way, the acceleration used for the calculation of the velocity is also shifted by $\frac{1}{2}\Delta t$. The schematic explanation of the algorithm is depicted in Fig.2.2.

Eqns.(2.7) and (2.8) can be solved iteratively by giving the initial atomic positions at $t = 0$, $\vec{x_i}(0)$ and the initial velocities at $t = -\frac{1}{2}\Delta t$, $\vec{v_i}(-\frac{1}{2}\Delta t)$. The force $\vec{F_i}(t)$ acting on atom i is calculated at each time t by adding all the contribution from neighboring atoms by

$$\vec{F_i}(t) = \sum_j \vec{F_{ij}}(t) = -\frac{\partial V_{total}}{\partial x_i} \quad (2.9)$$

2.1.2 Velocity rescaling temperature coupling

For most of the cases, the simulations are performed under constant temperature. Therefore, to maintain the constant temperature, it is necessary to implement the temperature coupling scheme called thermostat. There are several

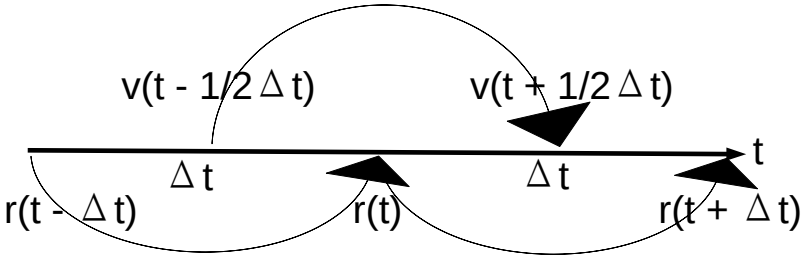

Figure 2.2: Schematic explanation of the leapfrog integration in MD simulations.

thermostats used in MD simulations, such as Berendsen thermostat[16], Andersen thermostat[5], Nosé-Hoover thermostat[142,83], and the velocity-rescaling thermostat[27]. In this thesis, the velocity-rescaling thermostat is used exclusively. Therefore, only the detail of the velocity-rescaling thermostat is explained.

In the scheme of the velocity rescaling temperature coupling, the system is virtually coupled to a heat bath such that the temperature decays exponentially to the reference temperature T_0. In order to achieve this, the kinetic energy $K = \frac{N_f}{2} k_B T$ is updated at each time step as

$$dK = (K_0 - K)\frac{dt}{\tau_T} + 2\sqrt{\frac{K_0 K}{N_f \tau_T}}dW, \tag{2.10}$$

where τ_T is a time constant, which can be set as a parameter, N_f is the number of degrees of freedom, $K_0 = \frac{N_f}{2}k_B T_0$ and dW is the Wiener noise.

2.1.3 Pressure coupling

The simulations are not performed only under constant temperature but also under constant pressure. To guarantee the constant pressure during the simulation, several coupling methods are used such as Brendsen [116], Parrinello-Rahman [146,143], and Martyna-Tuckerman-Tobias-Klein (MTTK) pressure couplings [131]. Here the Brendsen and Parrinello-Rahman pressure couplings are used in thesis. Thus, only these methods are explained in detail below.

Berendsen pressure coupling

In a similar manner as the Brendsen temperature coupling, the pressure of the system is corrected at each time step so that it converges to the reference pressure P_{0ij} as

$$\frac{dP_{ij}}{dt} = \frac{P_{0ij} - P_{ij}}{\tau_p}, \tag{2.11}$$

where τ_p is a coupling constant which can be set as a parameter and i, j are x, y or z. Accordingly, at each time step, the position of the atoms and the box size

are rescaled by scaling factor matrix

$$\mu_{ij} = \delta_{ij} - 3\frac{\Delta t}{\tau_p}\beta_{ij}\left(P_{0ij} - P_{ij}(t)\right), \tag{2.12}$$

where β_{ij} is the compressibility of the simulation box, which is in case of water 4.6×10^5 bar^{-1}, and δ_{ij} is the Kronecker delta. Accordingly, the position of atoms and the box length $\vec{l} = l_x, l_y, l_z$ are corrected as follows.

$$\mathbf{r}_i(t + \Delta t) = \boldsymbol{\mu}\mathbf{r}_i(t) \tag{2.13}$$

$$\vec{l}(t + \Delta t) = \boldsymbol{\mu}\vec{l}(t) \tag{2.14}$$

The box volume is also corrected as

$$V(t + \Delta t) = det(\boldsymbol{\mu})V(t) \tag{2.15}$$

Due to the work done by the pressure coupling, this energy should be subtracted at each time step by

$$-\sum_{i,j}(\mu_{ij} - \delta_{ij})P_{ij}V = \sum_{i,j} 2(\mu_{ij} - \delta_{ij})\Xi_{ij} \tag{2.16}$$

where Ξ_{ij} is the virial of the system.

This method aims to correct the pressure so that the average pressure is kept at the reference pressure $\mathbf{P}_0$, but does not yield correct *NPT* ensembles. Therefore, the ensemble average calculated by the simulation trajectories may

not be correct. Accordingly, it is mostly used for the system equilibriation, where only the final output of the simulation matters.

Parrinello-Rahman pressure coupling

In the frame of the Parrinello-Rahman pressure coupling, the simulation box cell vector matrix $\mathbf{b} = \{\mathbf{b}_1, \mathbf{b}_2, \mathbf{b}_3\}$ is corrected with respect to the time as follows,

$$\frac{d^2\mathbf{b}}{dt^2} = V\mathbf{W}\mathbf{b}'^{-1}(\mathbf{P} - \mathbf{P}_0), \tag{2.17}$$

where $\mathbf{b}'$ is the transpose matrix of $\mathbf{b}$, and $\mathbf{W}$ is the coupling matrix which determine how strongly each component is coupled to the external pressure $\mathbf{P}_0$ expressed in an explicit form as

$$\mathbf{W}^{-1}{}_{ij} = \frac{4\pi^2\beta_{ij}}{3\tau_p^2 L} \tag{2.18}$$

with L is the longest simulation box length. The Hamiltonian of the system is modified to

$$H = U + K + \sum_i P_{ii}V + \sum_{i,j}\frac{1}{2}W_{ij}\left(\frac{db_{ij}}{dt}\right)^2, \tag{2.19}$$

where U and K are the potential and kinetic energy of the system respectively. Accordingly, the equation of motion must be modified as

$$\frac{d^2\mathbf{r}_i}{dt^2} = \frac{\mathbf{F}_i}{m_i} - \mathbf{b}^{-1}\left[\mathbf{b}\frac{d\mathbf{b}'}{dt} + \frac{d\mathbf{b}}{dt}\mathbf{b}'\right]\mathbf{b}'^{-1} \cdot \frac{d\mathbf{r}_i}{dt} \tag{2.20}$$

In contrast to the Berendsen pressure coupling, this methods yields the correct *NPT* ensemble. Therefore it is used for the final production run which generates the trajectory for the calculation of the thermodynamics properties.

2.2 Density Functional Theory

As mentioned in the previous section, the potential of the atoms or molecules can be derived from the non-empirical methods such as *ab initio* calculations. *Ab initio* calculations are based on the quantum physics which is described by Schödinger equation, and hence, in general, the system consists of the atoms with nuclei and electrons.

The time dependent Schödinger equation of the system can be written as

$$i\hbar\frac{\partial\Phi}{\partial t} = \widehat{H}\Phi \tag{2.21}$$

where $\widehat{H}$ is the Hamiltonian of the system, $\hbar = h/2\pi$ with h the Planck constant, and Φ is the wave function of the total system. Using the explicit form of $\widehat{H}$ of the N particle system including both electrons and nuclei, Eqn.(2.21) is described as,

$$i\hbar\frac{\delta\Phi}{\delta t} = \left\{\sum_{i=1}^{N} -\frac{\hbar^2}{2m_i}\nabla^2 + \left(\sum_{i=1}^{N} V(\mathbf{r}_i) + \sum_{i=0}^{N}\sum_{j<i} U(\mathbf{r}_i, \mathbf{r}_j)\right)\right\}\Phi \tag{2.22}$$

Where V is the potential applied on the particles located at position $\mathbf{r}_i$ and $U(\mathbf{r}_i, \mathbf{r}_j)$ is the interaction energy between the particles i and j. Except for Hy-

drogen atom, it is impossible to solve the Eqn.(2.22) analytically. Therefore, several approximations have been developed. There are mainly two methods used in computational physics or chemistry. One is the Hartree-Fock method and the another is Density Functional Theory (DFT). Due to the computational cost and the accuracy, DFT is more widely used in the computational physics. Therefore, in this thesis only the basics of DFT is explained. The technical detail, such as computational implementation and several variants, should be referred in Ref. 8,12.

Regarding the relation of DFT with MD simulations, as the system which is simulated by MD consists of several ten thousands to several million atoms, the number of degrees of freedom of the system (positions and momenta of all the nuclei and electrons) is too enormous to solve the equation Eqn.(2.22) within a reasonable computational time. This is why the MD simulations are developed to encompass the basic statistical properties of the dynamics and the statics of the system by approximating the detail of the dynamics of the electrons as described in the previous chapter. For the approximation used in MD simulations, following properties are needed;

1. the optimized positions of the atoms within a molecule,
2. the charge distribution within a molecule,
3. the description of bonded and non-bonded interaction between atoms.

These properties can be derived either through empirical ways or by DFT calculations. DFT calculations can be used for the electronic structure determi-

nation of materials as well, such as electronic conductivity. However, in this thesis, they are exclusively used for the above mentioned purposes. For the first property, the optimized positions are derived by the ground state nucleus positions. For the second property, usually electron density is calculated from DFT calculations. However, using the CHELPG program[23,197], the partial charge are assigned on each atom in a molecule. The third property can also be calculated by the energy change with respect to relevant variables such as bond lengths, bond angles, and dihedral angles. In the study in this thesis, the first and the second properties are calculated explicitly for a certain molecule, and the third properties are approximated from previous similar work or very crude approximation which will be explained in the corresponding part in this thesis.

Regarding the approximations used to solve the Eqn.(2.22) , the first important approximation is the Born-Oppenheimer approximation[22]. In this approximation, nuclei are much heavier than electrons and thus, the velocities of nuclei are much lower than that of electrons. Therefore, electrons move instantaneously together with nuclei and the dynamics of the electrons only depends on the positions of the nuclei but not on the momentum of the nuclei. Accordingly the wave function Φ of the system can be decomposed into the product of the wave functions of the nuclei and the electrons.

$$\Phi = \Phi_n(\mathbf{R})\Phi_e(\mathbf{R}, \mathbf{r}), \tag{2.23}$$

where $\mathbf{R}$, $\mathbf{r}$ are the positions of the nuclei and electrons respectively and Φ_n,

Φ_e are the wave functions of the nuclei and the electrons respectively. Now the dynamics of the system is decomposed into nuclei part and electron part. Explicitly, it is written as,

$$i\hbar\frac{\partial\Phi_e}{\partial t} = \widehat{H}_e\Phi_e \tag{2.24}$$

with

$$\widehat{H}_e = \sum_{i=1}^{N_e} -\frac{\hbar^2}{2m_i}\nabla_{\mathbf{r}}^2 + \frac{1}{2}\sum_{i\neq j}^{N_e,N_e}\frac{1}{|\mathbf{r}_i-\mathbf{r}_j|} + \frac{1}{2}\sum_{i\neq j}^{N_e,N_n}\frac{Z_j}{|\mathbf{r}_i-\mathbf{R}_j|} + \frac{1}{2}\sum_{i\neq j}^{N_n,N_n}\frac{Z_iZ_j}{|\mathbf{R}_i-\mathbf{R}_j|} \tag{2.25}$$

for the electron part, where N_e and N_n are the number of the electrons and nuclei respectively, and Z_i is the electric charge on ith nucleus. And for the nuclei part,

$$i\hbar\frac{\partial\Phi_n}{\partial t} = (\widehat{T}_n + \widehat{H}_e)\Phi_n \tag{2.26}$$

$$\widehat{T}_n + \widehat{H}_e(\mathbf{R}) = \sum_{i=1}^{N_n} -\frac{\hbar^2}{2m_i}\nabla_{\mathbf{R}}^2, + \widehat{H}_e(\mathbf{R}) \tag{2.27}$$

,where $\widehat{T}_n$ is the kinetic energy of the nuclei. The nuclei moves on the ground state potential surface created by the electrons. This way, solving Eqn.(2.22) becomes simple. First Eqn.(2.24) is solved with fixed nuclei positions $\mathbf{R}$ and then Eqn.(2.26) is solved using the potential $\widehat{H}_e(\mathbf{R})$ obtained. However, due to the massive number of electrons involved in the dynamics, it is still not possible to calculate completely the wave functions of the nuclei and the electrons. The

nuclei part Eqn.(2.26) is sometimes solved by classical Newton's equations due to significantly slow motions of the nuclei compared to the electrons. However, the electron part Eqn.(2.24) needs to be treated in a quantum mechanical way. Therefore, in the reminder of this section, only the electron part is discussed. The main complexity of solving equation Eqn.(2.24) and (2.25) arises from the number of the degrees of freedom which is $3N_e$. In order to simplify the solution, the number of the degrees of freedom should be reduced, where the density functional theory (DFT) comes in. DFT is based on the Hohenberg–Kohn theorems which guarantee,

1. The external potential v_{ext} is uniquely determined by the ground state electron density $n(\mathbf{r})$.

2. There is an energy functional of $E_v(n(\mathbf{r}))$ which gives the ground state energy and the ground state electron density $n(\mathbf{r})$ at its global minimum.

Based on these theorems, the ground state energy E_G can be written as a functional of $n(\mathbf{r})$,

$$E_G(n(\mathbf{r})) = T_s(n(\mathbf{r})) + J(n(\mathbf{r})) + E_{XC}(n(\mathbf{r})) \tag{2.28}$$

where $T_s(n(\mathbf{r}))$ is the kinetic energy and $J(n(\mathbf{r}))$ is the electron-electron Coulomb interaction energy , and $E_{XC}(n(\mathbf{r}))$ is exchange–correlation energy which contains any other interaction energies. $E_{XC}(n(\mathbf{r}))$ is proven to exist

but the exact form of it is not known at all. Therefore, several approximations are needed for $E_{XC}(n(\mathbf{r}))$. The main advantage here is the significant decrease of the number of degrees of freedom from $3N_e$ to 3. In this frame work, there were some attempts for this approximation such as Thomas-Fermi model[202,65]. However, there was still a problem in accuracy of the calculations.

To overcome this difficulty, Kohn-Sham proposed Kohn-Sham (KS) ansatz in 1965 [106]. According to the KS ansatz, the interacting many particle systems have the same ground state electron density $n_0(\mathbf{r})$ and ground state energy E_0 with an auxiliary non-interacting particles system with orbitals Φ_i for ith particle. In this auxiliary system, the kinetic energy of the system is calculated by

$$T_s(n(\mathbf{r})) = \sum_i^N \int \Phi_i^*(\mathbf{r}, s) \left(-\frac{1}{2}\nabla^2 \right) \Phi_i(\mathbf{r}, s) d\mathbf{r} ds, \tag{2.29}$$

which is the sum of the kinetic energy of each electrons and spin s, and the electron density $n(\mathbf{r})$ is written as

$$n(\mathbf{r}) = \sum_i^N \sum_s \Phi_i^*(\mathbf{r}, s) \Phi_i(\mathbf{r}, s) \tag{2.30}$$

Note that, the atomic unit $\hbar = e = m_e = 4\pi/\varepsilon_0$ is used for simplicity. There-

fore, the total energy in the Kohn-Sham ansatz is written explicitly as

$$\begin{aligned} E_{KS}(n(\mathbf{r})) &= T_s(n(\mathbf{r})) + J(n(\mathbf{r})) + E_{XC}(n(\mathbf{r})) + V_{\text{ext}}(n(\mathbf{r})) \quad (2.31) \\ &= \sum_i^N \int \Phi_i^*(\mathbf{r}, s) \left(-\frac{1}{2}\nabla^2 \right) \Phi_i(\mathbf{r}, s) d\mathbf{r} ds \\ &\quad + \frac{1}{2} \int \int \frac{n(\mathbf{r}) n(\mathbf{r}')}{|\mathbf{r} - \mathbf{r}'|} d\mathbf{r} d\mathbf{r}' + E_{XC}(n(\mathbf{r})) \\ &\quad + \int v_{\text{ext}}(\mathbf{r}) n(\mathbf{r}) d\mathbf{r}, \end{aligned}$$

where the basis set Φ_i must be orthonormal as

$$\int \Phi_i^*(\mathbf{r}, s) \Phi_j(\mathbf{r}, s) d\mathbf{r} ds = \delta_{ij}, \quad (2.32)$$

and $V_{\text{ext}}(n(\mathbf{r}))$ is the potential energy due to the external potential by the nuclei, and $T_s(n(\mathbf{r}))$,$J(n(\mathbf{r}))$, $E_{XC}(n(\mathbf{r}))$ are the kinetic energy, the Coulomb interaction energy between electrons, the exchange-correlation energy of the auxiliary non-interaction N electron system in the KS ansatz. Note that, $T_s(n(\mathbf{r}))$, $J(n(\mathbf{r}))$ and $E_{XC}(n(\mathbf{r}))$ in Eqn.(2.32) are not necessarily same as the corresponding terms in Eqn.(2.28). The KS energy $E_{KS}(n(\mathbf{r}))$ must take the minimum value at the ground state density $n_0(\mathbf{r})$. Therefore, $\frac{\delta E_{KS}(n(\mathbf{r}))}{\delta n(\mathbf{r})} = 0$ must be satisfied under the constraint of the conservation of the particle number $\int n(\mathbf{r}) d\mathbf{r} = N$. This yields following N independent Kohn-Sham(KS) equa-

tions.

$$\left[-\frac{1}{2}\nabla^2 + v_{\text{ext}}(\mathbf{r}) + v_{\text{Hartree}}(\mathbf{r}) + v_{\text{xc}}(\mathbf{r})\right]\Phi_i(\mathbf{r},s) = \varepsilon_i\Phi_i(\mathbf{r},s), \qquad (2.33)$$

where $v_{\text{ext}}(\mathbf{r})$ is the external potential from the nuclei , and $v_{\text{Hartree}}(\mathbf{r}) = \frac{\partial J((\mathbf{r}))}{\partial n(\mathbf{r})} = \int \frac{n(r')}{|\mathbf{r}-\mathbf{r}'|}dr'$ is the electron-electron Coulomb interaction potential, and $v_{\text{XC}}(\mathbf{r}) = \frac{\partial E_{XC}((\mathbf{r}))}{\partial n(\mathbf{r})}$ is the exchange-correlation potential which contains the difference between the many interacting particles system and the N single particle systems in KS ansatz, and finally ε_i is the eigenvalues of the KS equation. In computation, it is reasonable to decompose the wavefunctions $\Phi_i(\mathbf{r},s)$ into limited number of basis sets for the calculations[8,12]. The exchange-correlation potential $v_{\text{XC}}(\mathbf{r})$ term can be approximated by several methods such as the local density approximation (LDA), the generalized gradient approximation (GGA), and their mixture, namely hybrid functionals, as well as many others. LDA assumes that the exchange-correlation energy $v_{\text{XC}}(\mathbf{r})$ at a position $\mathbf{r}$ is as same as the case in the homogeneous gas which has the electron density of $n(\mathbf{r})$. On the other hand, GGA includes the correction of the gradient of the ground state electron density gradient, namely $\nabla n(\mathbf{r})$. LDA can provide relatively good results. However, it depends on the system of interest and it is not always guaranteed that the GGA has the better results than LDA. It also depends on the balance between the accuracy of the computation and the computational costs. Note that the eigenvalues ε_i of Eqn.(2.33) do not have any physical meanings. Details of further applications, limitations

and variants of functionals are out of this scope. Therefore, those explanations must be referred to Ref. 8,12.

2.2.1 Self-consistent calculations

As the problem now is simplified into solving the Eqn.(2.33), it can be solved numerically by the self-consistent calculations with appropriate exchange-correlation functionals and the basis sets. As a initial guess, the electron density $n(\mathbf{r})$ should be given, which is usually the superposition of the single atom electron densities. For the geometry optimization, which is the main purpose of the use of DFT calculation in this thesis, the initial position of atoms should be given. The self-consistent calculation with geometry optimization follows.

1. Calculate the effective Kohn-Sham potential $v_{KS} = v_{\text{ext}}(\mathbf{r}) + v_{\text{Hartree}}(\mathbf{r}) + v_{\text{xc}}(\mathbf{r})$ in Eqn.(2.33) by substituting the electron density $n(\mathbf{r})$.

2. Use v_{KS} calculated above to solve the KS equations in Eqn.(2.33).

3. Use the obtained $\Phi_i(\mathbf{r}, s)$ for the calculation of the new electron density $n(\mathbf{r})$.

4. If the criteria such as difference in force, energy, electron density, etc, then move to the next step. Otherwise move the nuclei and start from step 1.

As a result, the optimized geometry of the atoms which has the minimum ground state energy is obtained. In this thesis later in Chapter. 7, the optimized geometry of the catalyst molecule using this methods is used for the force field development for the MD simulations.

3

Theory

In this chapter, several theories which are relevant to the study in this thesis are explained.

3.1 Kirkwood-Buff Theory

Acknowledgement : Part of the sentences in this section is reproduced from (T. Kobayashi, J. E. S. J. Reid, S. Shimizu, M. Fyta and J. Smiatek, *Phys. Chem. Chem. Phys.*, 2017, **19**, 18924 DOI: 10.1039/C7CP03717A)[104] with permission from the PCCP Owner Societies.

3.1.1 Kirkwood-Buff theory

A consistent description for IL-water mixtures, based on thermodynamic and statistical mechanics arguments is provided by the Kirkwood-Buff (KB) theory, which was originally developed as a molecular theory of solutions and solution mixtures[101,76,140,37,15,191,192,184,179,166,167,193,168,194,186,11,152,187]. It has to be noted that the KB theory does not assume any restrictions on the molecular structure of the solute molecules and the ion species, such that the theory is applicable for all systems in the liquid state. For different ion species, the introduction of an indistinguishable ion approach is necessary[113,191]. Hence, cations and anions have to be considered as one single species, which is denoted as *ions* in the following. In this context, simulations allow us to study the binding of species to individual ions in more detail and to obtain results which are inaccessible to inverse KB approaches, as it will be pointed out in the remainder of this chapter.

In this thesis, focus is given on the analysis of the binding behavior between the ions, as denoted by the index '2' and solute molecules with the index '1'.

In this way, three local binding modes according to ion-ion, solute-solute and ion-solute binding can be defined. For the analysis, the KB integral, which is the most essential ingredient of the KB theory is defined as

$$G_{ij} = 4\pi \int_0^\infty r^2 [g_{ij}(r) - 1] \, \mathrm{d}r \tag{3.1}$$

which can be approximated by

$$G_{ij} \approx G_{ij}(r_c) = 4\pi \int_0^{r_c} r^2 [g_{ij}(r) - 1] \, \mathrm{d}r \tag{3.2}$$

where $g_{ij}(r)$ corresponds to the radial distribution function between two species i and j, and r_c is a finite cutoff distance as defined through $g_{ij}(r) = 1$ for all values $r \geq r_c$ [37,192,152]. The KB integrals can be interpreted as excess volumes corresponding to the non-ideal distribution of molecular species with the requirement of symmetry, $G_{ij} = G_{ji}$. In contrast to an ideal gas, real molecules of species k have a fixed size a_k, such that all values $G_{ij}(a_k) < 0$ for $r \leq a_k < r_c$ expressing the excluded volume of the molecule. Moreover, one can find $G_{ij}(a_k) < G_{ij}(a_n)$ for $a_k > a_n$. The corresponding number of excess particles or molecules can be calculated by $N_{ij}^{xs} = \rho_j G_{ij}$ with the bulk number density ρ_j and the additional requirement $N_{ij}^{xs} \neq N_{ji}^{xs}$. Although the original KB theory and the KB integrals were formulated in order to describe molecular fluctuations in the grandcanonical μVT ensemble, it was shown that identical expressions can be derived equivalently in several other ensembles and

specifically in the NVT and the NpT ensemble [15,153]. A more detailed overview on the KB theory should be referred to Refs. 15,76,140,152,179.

More detailed approaches to study charged systems in terms of the KB theory can be found in Refs. 113,114,115,116,169 and for ILs in Refs. 161,160. Hence, assuming that IL cations and anions contribute equivalently, one can define the ion-ion KB integral G_{22} in presence of cations $(+)$ and anions $(-)$ according to [218,73,68]

$$G_{22} = \left(\frac{n_+}{n_\pm}\right)^2 G_{++} + \left(\frac{n_-}{n_\pm}\right)^2 G_{--} + \frac{n_+ n_-}{n_\pm^2}(G_{+-} + G_{-+}) \tag{3.3}$$

with $n_\pm = n_+ + n_-$ and $G_{+-} = G_{-+}$, where n_j with $j = +, -$ denotes the number of ion species or stoichiometric coefficients in the corresponding ion dissociation/association equilibrium. The resulting KB integral for ion-solvent interactions is defined by

$$G_{21} = G_{12} = \frac{n_+}{n_\pm} G_{+1} + \frac{n_-}{n_\pm} G_{-1} \tag{3.4}$$

with $G_{21} = G_{\pm 1} = G_{1\pm}$.

Based on the KB integrals, one can define a preferential binding coefficient [152,179]

$$\nu_{ji} = \rho_i (G_{ji} - G_{jj}) \tag{3.5}$$

with $i, j = 1, 2$ and $i \neq j$. For values $\nu_{ji} > 0$, one can observe a preferential binding of species i to species j according to the relation [152,179]

$$\nu_{ji} = N_{ji}^{xs} - \frac{\rho_i}{\rho_j} N_{jj}^{xs} \tag{3.6}$$

and equivalently, a preferential exclusion for $\nu_{ji} < 0$ [187]. The preferential binding coefficient at a temperature T with the Boltzmann constant k_B is also connected with the transfer free energy [187]

$$F_{ji}^{*} = -k_B T \nu_{ji} \tag{3.7}$$

which estimates the free energy that is needed to bring two species infinitely apart in close contact.

Although the KB integrals and the KB theory can be derived from rigorous statistical mechanical arguments, some problems in their computational evaluation remain unresolved. The KB integrals need to show a good convergence at large distances in order to provide reasonable values. Recently, several techniques were proposed in order to achieve this aim and to introduce further modifications in computer simulations [172,111,171,70,40]. An older approach also corrects the values of KB integrals in closed systems [117]. Accordingly, it is possible to deduce reliable results even from non-convergent KB integrals. Specifically, for long-range ordered fluids like ILs [119], the evaluation of these values is a challenging task. Fortunately, if the underlying radial distribution func-

tion $g_{ij}(r)$ is well-behaved at large distances, *i. e.* showing regulatory oscillations with approximately constant periods, the values of $G_{ij}(r)$ for $r \gg 1$ nm oscillate around a constant number as well. In this respect, the running average $\bar{G}_{ij}(r)$ in this region fluctuates around G_{ij} and establishes the relation $\bar{G}_{ij}(r) \approx G_{ij}$. The fluctuations can be used to determine the standard deviation of G_{ij}.

Another problem arises due to the constraints of the indistinguishable ion approach, which prohibits a more detailed analysis of the solute binding behavior to the individual ion species, namely cations and anions separately. The limitations of the KB integrals for standard simulation approaches [172,111,171] can be circumvented by introducing the local/bulk partition coefficient [41,184,183],

$$K_{ij}^{p} = \frac{\langle N_{pi}(r)\rangle / \langle N_{pj}(r)\rangle}{N_i / N_j} \tag{3.8}$$

with $i, j, p = 1, 2, +, -$, and the definition $\langle \cdots \rangle$ for the average local number of molecules of species i in comparison to species j around molecules of species p. The total number of molecules is defined by the relation $N_i = \rho_i \cdot V$ with volume V and the cumulative local number of molecules

$$N_{ij}(r) = 4\pi\rho_j \int_0^r r^2 g_{ij}(r)\mathrm{d}r \tag{3.9}$$

can be used to calculate coordination numbers $N_{ij}(d)$ around specific molecules by integration of Eqn. (3.9) up to a specific distance d, usually in-

cluding the first solvation shell.

Although a direct connection between the local/bulk partition coefficient and the KB theory is questionable[183], a preferential exclusion or a preferential binding mechanism of species indeed can be explained[119,48,136,178]. For instance, at short distances in the local region around the reference molecule, values of $K_p > 1$ and $K_p < 1$ indicate a preferential binding or a preferential exclusion behavior, respectively. Hence, it is possible to compute different local/bulk partition coefficients in order to distinguish between cation and anion properties. Accordingly, the local/bulk partition coefficient provides a simple and reliable analysis tool for binding properties in computer simulations[119,187].

3.1.2 Inverse Kirkwood-Buff theory

Whereas the direct KB approach relies on an evaluation of the known radial distribution function, the inverse KB theory focuses on thermodynamic and experimental data for the calculation of the KB integrals in several mixtures[14,15] and thus also in water-IL solutions[161,160]. In the following, the derivation of KB integrals for binary solutions and more specifically for IL-solute mixtures is briefly sketched. More detailed information can be found in Refs. 161,160. Using the well-known relation for the derivative of the solute chemical activity[152,161]

$$a_{11} = \left(\frac{\partial \mu_1}{\partial \ln \rho_1}\right)_{T,p} = \left(\frac{\partial \ln a_1}{\partial \ln \rho_1}\right)_{T,p} = \frac{1}{1 + \rho_1 (G_{11} - G_{12})} \tag{3.10}$$

with μ_1 the chemical potential and a_1 the activity of solute, one can define a chemical equilibrium according to $\mu_1^V = \mu_1$. This would be the chemical potential of the solute vapor phase,

$$\mu_1^V = \mu_1^{\text{int}} + k_B T \ln \rho_1^V \Lambda_1^3 \tag{3.11}$$

with the solute vapor phase density ρ_1^V. Most importantly, the intramolecular contributions μ_1^{int} and the momentum partition function Λ_1^3 do not depend on the solute liquid phase bulk number density and thus Eqn. (3.10) can be rewritten according to

$$\rho_1 (G_{11} - G_{12}) = \left(\frac{\partial \ln \rho_1}{\partial \ln \rho_1^V} \right)_{T,p} - 1 \tag{3.12}$$

as it was outlined in Ref. 161. An equivalent expression for the solute-ion KB integral in agreement with Eqn. (3.1) can be derived from the relation

$$(\rho_1 G_{11} + 1) V_1 + \rho_2 G_{12} V_2 - RT\kappa_T = 0 \tag{3.13}$$

where V_1, V_2 denote partial molar volumes of the species and κ_T the isothermal compressibility with the molar gas constant R. From the relation above, the corresponding KB integrals can be written as

$$G_{12} = -V_1 \left(\frac{\partial \ln \rho_1}{\partial \ln \rho_1^V} \right) + k_B T \kappa_T \tag{3.14}$$

for the ion-solute,

$$G_{11} = \frac{1}{n_1}\left(n_2 V_2 \frac{\partial \ln \rho_1}{\partial \ln \rho_1^V} - 1\right) \tag{3.15}$$

for the solute-solute KB integral and

$$G_{22} = -V_1\left(1 - \frac{1}{\rho_2 V_2}\right)\left(\frac{\partial \ln \rho_1}{\partial \ln \rho_1^V}\right) - \frac{1}{\rho_2} + k_B T \kappa_T \tag{3.16}$$

for the ion-ion KB integral, respectively. For the evaluation of the KB integrals in the inverse KB approach, one needs experimental values for the solute and ion bulk number densities ρ_1,$\rho_2$in the liquid mixtures, values for the solute vapor densities ρ_1^V at specific mole fractions and the corresponding values for the partial molar volumes of solute and ions V_1, V_2 in combination with the isothermal compressibility κ_T of the solution.

As an alternative, a much more compact formulation of the KB integrals can be derived by introducing the derivative of the solute chemical potential with respect to the solute mole fraction x_1, which reads

$$B = \frac{x_1}{k_B T}\left(\frac{\partial \mu_1}{\partial x_1}\right)_{T,p} = \left(\frac{\partial \ln a_1}{\partial \ln x_1}\right)_{T,p} \tag{3.17}$$

as it was outlined in detail in Ref. 160. Due to the fact, that the data for the inverse KB integrals rely on the original formulation, the outlined approach formulated in Ref. 161 is used. By doing so, a crucial point is the numerical evaluation of $(\partial \ln \rho_1 / \partial \ln \rho_1^V)$ in addition to the extraction of the correspond-

ing values. A meaningful approach in order to establish a useful protocol was recently presented in Refs. 161,160.

Additionally, KB integrals are also reasonable measure to explain the microscopic structure of the solution considering its relation with the partial structure factors. The global properties of the solution can be studied through the partial structure factors at different length scales. In particular, the use of partial structure factors was already established for IL/solute mixtures[91] according to the expression

$$S_{ij}(q) = 1 + \frac{4\pi\rho_j}{q} \int_0^\infty r \sin(qr)[g_{ij}(r) - 1]\, \mathrm{d}r \tag{3.18}$$

with $q = 2\pi/r$. This is equivalent to

$$S_{ij}(\vec{q}) = 1 + \rho_j \hat{G}_{ij}(\vec{q}) \tag{3.19}$$

with the corresponding Fourier-transformed KB integrals

$$\hat{G}_{ij}(\vec{q}) = \int_V [g_{ij}(\vec{r}) - 1]\, e^{-i\vec{q}\vec{r}}\, \mathrm{d}\vec{r}, \tag{3.20}$$

which can be further modified in terms of Fourier-transformed excess numbers of particles with $\hat{N}^{\mathrm{xs}}(\vec{q}) = \rho_j \hat{G}_{ij}(\vec{q})$, such that Eqn. (3.19) then reads $S_{ij}(\vec{q}) = 1 + \hat{N}^{\mathrm{xs}}(\vec{q})$. The above introduced relations highlight the fact that the partial structure factor is closely related to the functional form of the KB integrals (Eqn. (3.1)) and thus also accounts for excess quantities.

These protocols were used for the comparison of KB integrals between the simulation by direct KB integrals and the experiments by inverse KB integrals in Ref. 104 and showed a good agreement, which enhanced the validity of this protocol and also the simulation methods used in this thesis.

3.1.3 Mean square displacement of molecules

In order to study the dynamic behavior of the considered species in solution, one can calculate the mean-square displacement (MSD) of the center of mass for the corresponding molecules according to $\langle \Delta r^2(t) \rangle = \langle (\vec{R}_{cm}(t) - \vec{R}_{cm}(t_0))^2 \rangle$, which is related to the Einstein expression

$$\langle \Delta r^2(t) \rangle = 6 D_{cm} \lim_{t \to \infty} t \tag{3.21}$$

with the diffusion coefficient D_{cm} and the center-of-mass positions $\vec{R}_{cm}$ at long times $t \to \infty$. The introduction of the parameter α according to [51]

$$\sqrt{\langle \Delta r^2(t) \rangle} \sim t^{\alpha} \tag{3.22}$$

allows us to distinguish between different diffusion regimes. Diffusive behavior, as indicated by $\alpha = 0.5$, dominates for long times according to the Einstein expression, and a different value of $\alpha \neq 0.5$ can be observed at shorter times or for glass-like liquids [51]. Although the diffusion properties are usually estimated by the diffusion constant D_{cm} introduced above, the poor statistics of

the data available for the long time regime in Eqn.(3.21) is problematic in large scale simulations or in the simulations which involves macro-molecules such as proteins due to the limited simulation time or limited number of these macro-molecules. In this case, the MSD profiles can be used to estimate the differece in the diffusion behavior between different species in the solution.

3.2 Effective Interaction Energies

Acknowledgement : Copyright 2021 Wiley. Part of the sentences in this chapter is used with permission from (Kobayashi, T., Smiatek, J. and Fyta, M. (2021), Energetic Arguments on the Microstructural Analysis in Ionic Liquids. Adv. Theory Simul., 4: 2100114. https://doi.org/10.1002/adts.202100114).

The KB integrals (KBIs) provide an important insight on how each species in the IL solutions, namely cation, anions, and solute, preferably interacts each other from the information of molecular configuration around each species. Intuitively, it can be speculated that if the molecules preferably interact each other, the interaction energy between those molecules is low. Therefore it is natural to try to relate KBIs and the interaction energy between the species.

In order to provide a detailed analysis of this energetic contributions to the preferential interactions between the species, the respective conservative long- and short range interactions between the different molecules in the IL-solute mixtures is described by "effective interaction energy". The term "effective"

comes from the fact that the influence of the concentration of the molecules is removed, which may hinder the change of the interaction energy caused by the microstructural change. The argument discussed here is reliable based on the force field methodology which already has shown its merits in the context of atomistic MD simulations for a broad range of systems. In the following, the indices i, j denote different species, namely cation, anion or solute. In atomistic MD simulations, the intermolecular potentials are typically represented by long-range (long) and short-range (short) interactions due to the cut-off radius of the direct calculation of the pair-wise interactions. It has to be noted that the interaction energies between molecules are typically evaluated between the interaction between atoms of molecules but here this point is neglected and assume short- and long range interactions as the sum of molecular interactions between the atoms of distinct species. The total interaction energy between molecules i and j per unit volume is expressed by

$$E_{ij} = E_{ij}^{\text{short}} + E_{ij}^{\text{long}} \tag{3.23}$$

$$= (E_{ij}^{\text{short,LJ}} + E_{ij}^{\text{short,Coul}}) + E_{ij}^{\text{long}} \tag{3.24}$$

where both the short-range interaction energy E_{ij}^{short} and long-range interaction energy E_{ij}^{long} are taken into consideration, respectively. Furthermore the short range interaction is divided into Lennard-Jones part $E_{ij}^{\text{short,LJ}}$ and Coulomb part $E_{ij}^{\text{short,Coul}}$. In order to provide a reliable estimate of interaction energies, 1 nm is set as a cut-off distance for the short-range interaction both for

Lennard-Jones and Coulomb interactions after which a bulk behavior can be observed as shown in section III 'Results'. In order to assess the interaction between each species in the solution, the effective interaction energy γ_{ij} between distinct molecular species i and j is defined through

$$\gamma_{ij}^{LJ/Coul} = \begin{cases} \dfrac{E_{ij}^{\text{short,LJ/Coul}}}{n_i n_j/2}, & i = j \\ \dfrac{E_{ij}^{\text{short,LJ/Coul}}}{n_i n_j}, & i \neq j \end{cases} \tag{3.25}$$

where n_i, n_j are the numbers of species per unit volume. For $i = j$, a factor of 1/2 is needed to avoid double counting. The effective interaction energy is actually an indication of how well each species interacts with the other species and thus an indicator of the local arrangement within a cutoff-distance. Thereby, this parameter allows us to condense all relevant information on the local arrangement onto a single value. In view of non-identical mole fractions, Eqn.(3.25) is normalized with respect to a mean interaction energy per pair of species. The spatial short-range mean interaction energy between species i and j, E_{ij}, can otherwise also be expressed using the molecular distribution of species i around species j (or similarly as the distribution of species j around species i) as

$$E_{ij}^{\text{short,LJ/Coul}} = \begin{cases} \dfrac{1}{2} n_i \displaystyle\int_0^{r_{cut}} 4\pi r^2 E_{ij}^{LJ/Coul}(r) n_{ij}(r) dr, & i = j \\ n_i \displaystyle\int_0^{r_{cut}} 4\pi r^2 E_{ij}^{LJ/Coul}(r) n_{ij}(r) dr, & i \neq j \end{cases} \tag{3.26}$$

where $E_{ij}(r)$ is the average interaction energy between one molecule of species i and one molecule of species j separated by a distance r. The prefactor n_i is included as the species of type i are used as a reference. In order to take into account all molecules from species of type i and j within the volume slice, the corresponding value with the local number density $n_{ij}(r)$ of species j around one molecule of species i is multiplied. Substituting Eqn.(3.26) into Eqn.(3.25) by taking also into account the definition of the radial distribution function $g_{ij}(r_{ij})$ of species j around species i, and also the cutoff radius $r_{cut} = 1$ nm for the short-range interaction yields

$$\gamma_{ij}^{LJ/Coul} = \begin{cases} \frac{1}{2} \int_0^{r_{cut}} 4\pi r^2 E_{ij}^{LJ/Coul}(r) g_{ij}(r) dr, \; i = j \\ \int_0^{r_{cut}} 4\pi r^2 E_{ij}^{LJ/Coul}(r) g_{ij}(r) dr, \; i \neq j \end{cases} \tag{3.27}$$

Eqn.(3.25) and Eqn.(3.27) are different expressions for the same entity assuming homogeneous solutions. Notably, Eqn.(3.27) introduces a fixed reference position due to the introduction of the radial distribution function, whereas Eqn.(3.25) considers a bulk volume-like behavior. From the simulations, E_{ij}^{short} can be calculated directly , thus, $\gamma_{ij}^{LJ/Coul}$ using Eqn.(3.25). $\gamma_{ij}^{LJ/Coul}$ can be also expressed in a different way by Eqn.(3.27) using the radial distribution functions $g_{ij}(r)$. These values, γ_{ij}^{LJ} and γ_{ij}^{Coul} at a certain molecular concentration, indicate by definition how much are the contributions of Lennard-Jones and Coulomb interactions in a local interaction between molecules i and j at the corresponding molecular concentration. By accessing the change of

these values with respect to the molecular concentration, one can estimate the change of the contributions of Lennard-Jones interactions and Coulomb interactions to the preferential interaction between each species.

3.3 Lattice-gas Model

In order to study the molecular structure in front of the surface, the Lattice-gas models [107] for both neat ILs, as well as IL solutions are discussed. Of interest are the free energies of the species in the solutions and the corresponding chemical potentials. The respective theories are used together with the data from the simulations in order to evaluate the behavior and structuring of the species in the solution close to charged and neutral IFs. In this framework, the system is sliced into slabs parallel to the surface (xy-plane) at the distance z from the surface. Furthermore, each slab is divided into sites which can be occupied by the species, namely cations, anions and solute molecules. The schematic view of each slab is sketched in FIG. 3.1.

3.3.1 Free Energy Calculations

Within the framework of the Lattice-gas model [107], the free energy F of the IL mixtures can be calculated through

$$F = e\Phi(N_+ - N_-) + B_+N_+^2 + B_-N_-^2 + CN_+N_- - k_BT\ln W, \quad (3.28)$$

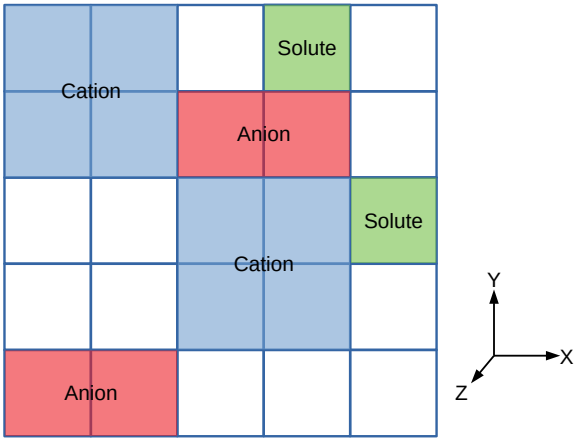

Figure 3.1: A schematic view of the slab in xy plane. The slab is divided into lattice. Different species can occupy different number of sites depending on their molecular size.

where Φ is the mean field electrostatic potential, N_+ and N_- are the numbers of the cations and the anions, respectively, B_+ and B_- and C are the coefficients for the cation-cation, anion-anion and cation-anion interactions, and $k_B \ln W = S$ is the mixing entropy of the mixture. The latter can be expressed as

$$S = k_B \ln W = k_B \ln \frac{N!}{(N - n_+N_+ - n_-N_-)!(n_+N_+)!(n_-N_-)!}, \quad (3.29)$$

where k_B is the known Boltzmann constant and N the number of the total available sites for each species within the slab parallel to the xy plane, and n_+ and n_- are the number of the sites occupied by a cation and an anion, respectively.

The Lattice-gas theory was originally developed for the ions in dilute electrolytes, but can be extended to describe also a neutral solute in the mixture,

along the same lines. Accordingly, the free energy F can be written as

$$\begin{aligned} F &= e\Phi(N_+ - N_-) + \sum_i (U_i^{\mathrm{IF}} N_i) - \vec{d}\cdot\vec{E}N_s + B_+ N_+^2 \\ &\quad + B_- N_-^2 + B_s N_s^2 + \sum\sum_{i\neq j} C_{ij} N_i N_j - TS, \end{aligned} \tag{3.30}$$

where, in addition to the notation used in Eqn.(3.28), the subscript s denotes the solute, and $i,j = +, -, s$, and $\vec{d}$ is the mean dipole moment of the solute molecules, and $\vec{E}$ is the mean electric field, and N_s is the number of the solutes, and B_s is the coefficient of the solute-solute interaction, and C_{ij} is the coefficient of the interaction between the species i and j. In order to express the non-Coulomb interactions between all species in the solution and the surface, the interaction energy between one molecule of species i with the surface, U_i^{IF} needs to be added. The entropy now reads as

$$\begin{aligned} S &= k_B \ln W \\ &= k_B \ln \frac{N!}{(N - n_+N_+ - n_-N_- - n_sN_s)!(n_+N_+)!(n_-N_-)!(n_sN_s)!}, \end{aligned} \tag{3.31}$$

where, in addition to the notations used in Eqn.(3.29), n_s is the number of the sites occupied by a solute molecule.

3.3.2 Chemical Potentials

The chemical potentials of each species can be calculated from the derivatives of free energy (Eqn.(3.31)) with respect to the number N_i of each species using

the Stirling formula ($\ln N! \approx N \ln N + N$)

$$\begin{aligned}
\mu_+ &= \frac{dF}{dN_+} \qquad (3.32)\\
&= e\Phi + U_+^{\mathrm{IF}} + 2B_+N_+ + C_{+-}N_- + C_{+s}N_s \\
&\quad -k_BT\ln\frac{n_+N_+}{N - n_+N_+ - n_-N_- - n_sN_s} \\
\mu_- &= \frac{dF}{dN_-} \qquad (3.33)\\
&= -e\Phi + U_-^{\mathrm{IF}} + 2B_-N_- + C_{+-}N_+ + C_{-s}N_s \\
&\quad -k_BT\ln\frac{n_-N_-}{N - n_+N_+ - n_-N_- - n_sN_s} \\
\mu_s &= \frac{dF}{dN_s} \qquad (3.34)\\
&= -\vec{d}\cdot\vec{E} + U_s^{\mathrm{IF}} + 2B_sN_s + C_{+s}N_+ + C_{-s}N_- \\
&\quad -k_BT\ln\frac{n_sN_s}{N - n_+N_+ - n_-N_- - n_sN_s}
\end{aligned}$$

In a well equilibrated system, the chemical potentials of each species are the same everywhere in the solution. By equating the chemical potential in bulk μ_i^{bulk} and at the IF μ_i^{IF}, setting the interaction term $2B_iN_i + \sum_{j\neq i} C_{ij}N_j = E_i$, and using the relations for $\Phi = 0, \vec{d}\cdot\vec{E}^{\mathrm{bulk}} = 0$ and $U_i^{\mathrm{bulk}} = 0$ in the bulk, the following relations can be obtained:

$$\begin{aligned}
\Delta H_+ - T\Delta S_+ &= (E_+^{\mathrm{bulk}} - E_+^{\mathrm{IF}}) - e\Phi^{\mathrm{IF}} - U_+^{\mathrm{IF}} \qquad (3.35)\\
&\quad -k_BT\ln\frac{N_+^{\mathrm{bulk}}\cdot(N - n_+N_+^{\mathrm{IF}} - n_-N_-^{\mathrm{IF}} - n_sN_s^{\mathrm{IF}})}{N_+^{\mathrm{IF}}\cdot(N - n_+N_+^{\mathrm{bulk}} - n_-N_-^{\mathrm{bulk}} - n_sN_s^{\mathrm{bulk}})} \\
&= 0,
\end{aligned}$$

$$\begin{aligned}\Delta H_- - T\Delta S_- &= (E_-^{\text{bulk}} - E_-^{\text{IF}}) + e\Phi^{\text{IF}} - U_-^{\text{IF}} \\ &= -k_B T \ln \frac{N_-^{\text{bulk}} \cdot (N - n_+ N_+^{\text{IF}} - n_- N_-^{\text{IF}} - n_s N_s^{\text{IF}})}{N_-^{\text{IF}} \cdot (N - n_+ N_+^{\text{bulk}} - n_- N_-^{\text{bulk}} - n_s N_s^{\text{bulk}})} \\ &= 0,\end{aligned} \tag{3.36}$$

$$\begin{aligned}\Delta H_s - T\Delta S_s &= (E_s^{\text{bulk}} - E_s^{\text{IF}}) + \vec{d} \cdot \vec{E}^{\text{IF}} - U_s^{\text{IF}} \\ &\quad -k_B T \ln \frac{N_s^{\text{bulk}} \cdot (N - n_+ N_+^{\text{IF}} - n_- N_-^{\text{IF}} - n_s N_s^{\text{IF}})}{N_s^{\text{IF}} \cdot (N - n_+ N_+^{\text{bulk}} - n_- N_-^{\text{bulk}} - n_s N_s^{\text{bulk}})} \\ &= 0,\end{aligned} \tag{3.37}$$

where $\Delta H_+ = (E_+^{\text{bulk}} - E_+^{\text{IF}}) - e\Phi^{\text{IF}} - U_+^{\text{IF}}$, $\Delta H_- = (E_+^{\text{bulk}} - E_+^{\text{IF}}) - e\Phi^{\text{IF}} - U_+^{\text{IF}}$, $\Delta H_s = (E_s^{\text{bulk}} - E_s^{\text{IF}}) + \vec{d} \cdot \vec{E}^{\text{IF}} - U_s^{\text{IF}}$, and $\Delta s_i = k_B \ln \frac{N_i^{\text{bulk}} \cdot (N - n_+ N_+^{\text{IF}} - n_- N_-^{\text{IF}} - n_s N_s^{\text{IF}})}{N_i^{\text{IF}} \cdot (N - n_+ N_+^{\text{bulk}} - n_- N_-^{\text{bulk}} - n_s N_s^{\text{bulk}})}$. In these, $-\Delta H_i$ and $-T\Delta S_i$ are the excess enthalpic and excess entropic contributions to the chemical potentials at the IF compared to the bulk solutions. Accordingly, by calculating either excess entropic contribution or excess enthalpic contribution, one can know the other contribution. In this thesis, by calculating the excess entropic contribution $-T\Delta S_i$, the structural change at the IF with respect to the solute concentration is accessed in terms of whether the change is governed by the enthalpic change or entropic change.

4

Ionic Liquids in Bulk

4.1 Motivation

Here, the motivation is to find a way to describe the microscopic structural change of IL-solute mixtures with respect to the solute concentration. For this purpose, Kirkwood-Buff integrals (KBIs) and effective interaction energies are

calculated to describe the change of ionic structures with respect to the solute concentrations. As introduced in the previous chapter 3, Kirkwood-Buff (KB) theory is a solution theory, from which Kirkwood-Buff integrals (KBIs) are derived to describe the preferential interactions between the species in the solution, namely between cations, anions, and solutes. The difficulty of using KB theory for the computational study arises from the fact that there has not been any direct comparison of KB integrals between experiments and simulations, which validates the simulation methods in terms of describing the preferential interactions between species in the solution. In my master thesis, a direct comparison between experimental data and simulation data were attempted in collaboration with J. E. S. J. Reid and S. Shimizu from the University of York, UK[104] with successful agreement between the derivation from the experimental data and the simulation data. In this PhD thesis, further theoretical framework is developed by means of effective interaction energies. While KB integrals contain the microstructural information through the radial distribution functions (rdfs), the effective interaction energies contain further information of the interaction energy between the species. Since the validity of KBIs in terms of describing the preferential binding between the species is already confirmed in Ref. [104], the comparison between the KBIs and the effective interaction energies highlights the validity of the argument of effective interaction energy discussed in Ref. [105]. The KBIs have difficulty in convergence due to the fluctuation of the rdfs in a long distance, while the effective interaction energy does not have such an issue. Therefore, more robust and stable analysis

can be done using effective interaction energy.

In this chapter, the mixtures of $[EMIM]^+[DCA]^-$ as IL, and water/DMSO as solutes with different solute concentrations between $x_{sol} = 0$ to 0.875 are studied. The atomic structures and the detail of the simulation setups are written in FIG.4.1 and A.1 respectively. Due to the statistical problem arising from the limitation on the size of the simulation box and the computational time which leads to a poor convergence of the single KBI calculation, the united ions (cations and anions) is used for the KBIs calculations. The focus here is given on the preferential binding coefficient G_{12} - G_{22} (in Eqn.(3.5), where G_{12} is the KB integral between ions and solutes (water/DMSO), and G_{22} is the KB integral between ions and ions. The cut-off length of the integration in Eqn.(3.2) is set to 1.5 nm. After the comparison between KBIs and the effective interaction energies, further analysis is done in order to elucidate the microstructural changes behind of the KBIs and effective interaction energy observations.

4.2 Results

4.2.1 KB integrals and effective interaction energies

For the comparison between KBIs and the effective interaction energies, first, the preferential binding coefficient G_{12} - G_{22} was calculated in FIG.4.2, where G_{ij} is the KBI between species i and j. There is a distinct difference between the DMSO mixtures and the water mixtures. As the solute concentration in-

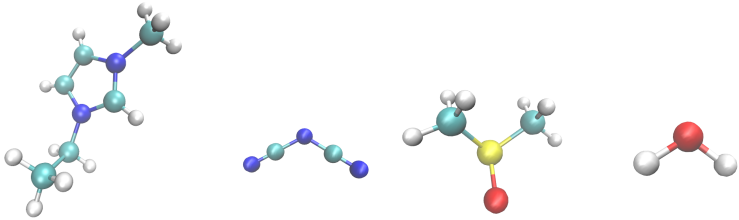

(a) (b) (c) (d)

Figure 4.1: The atomic structures of (a) $[EMIM]^+$, (b) $[DCA]^-$, (c) DMSO and (d) water. The carbon (C), nitrogen (N), oxygen (O), and hydrogen (H) atoms are colored in cyan, blue, red, and white, respectively. Copyright 2021 Wiley. Used with permission from Ref. 105.

creases, DMSO is more excluded from the ions, which can be seen from the decreasing trend of the red line in FIG.4.2. The opposite case is for the water mixtures. Water accumulates near the ions with respect to the water concentration. These results indicate that DMSO keeps the ionic structure intact, while water disturbs or breaks it.

In order to verify the above mentioned observation in terms of an energetic argument, the total effective interaction energies $\gamma_{ij} = \gamma_{ij}^{LJ} + \gamma_{ij}^{Coul}$ are calculated between each species in the IL-solute mixtures at different solute concentrations using Eqn.(3.25). The calculated values are shown in FIG.4.3. As clearly seen on the purple lines which refer to the cation-anion interactions, the values decrease for the DMSO mixtures, while the values increase for the water mixtures. These results indicate that the addition of DMSO into IL increases the strength of ionic structure and the addition of water does the opposite. This shows a fairly good agreement with the analysis of the KB integrals in FIG.4.2.

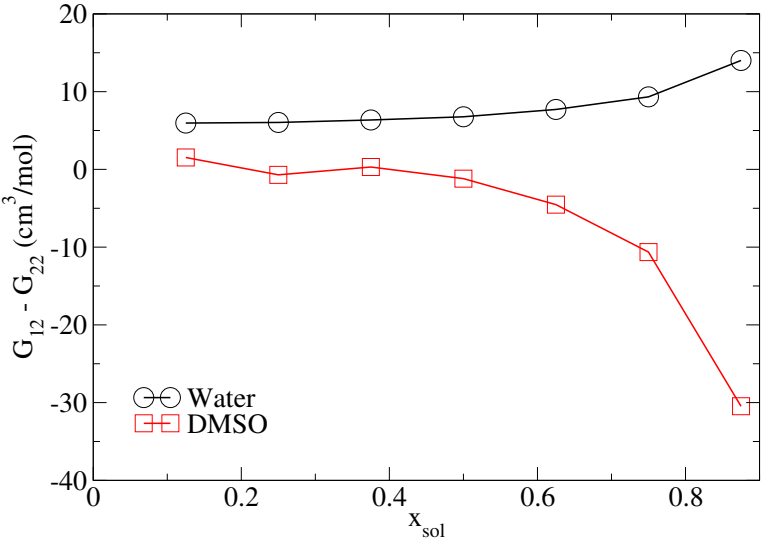

Figure 4.2: The preferential binding coefficient of solutes G_{12} - G_{22}. Black line with black symbols is water mixtures and red line with red symbols is DMSO mixtures. The subscripts are 1: solutes(water/DMSO) and 2: ions.

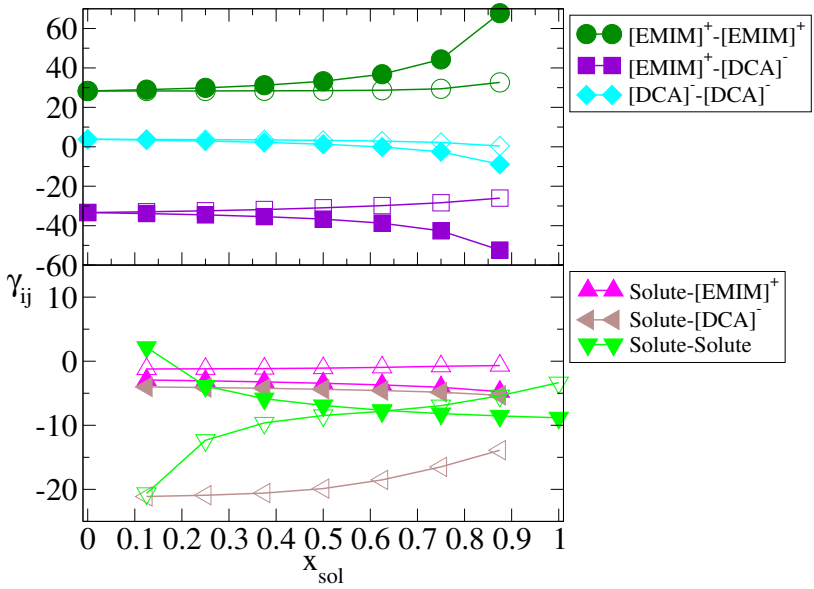

Figure 4.3: The total effective interactions $\gamma_{ij}(\mathrm{kJ}\cdot\mathrm{nm}^3/\mathrm{mol})$ between the species in the bulk DMSO-$[EMIM]^+[DCA]^-$ (filled symbols) and water-$[EMIM]^+[DCA]^-$ (open symbols) mixtures at different solute concentrations. The species types and their combinations are labelled according to the legends. Copyright 2021 Wiley. Used with permission from Ref. 105.

This also agrees with experimental observations[99]. This way, the effective interaction energy γ_{ij} can be used as a measure to estimate the change of ionic structure in IL-solvent mixtures. These calculations of KB integrals and effective interaction energies show a good agreement, which highlights the validity of the framework of the effective interaction energy and that these are very useful method to analyze the change of ionic structure in the IL-solute mixtures. In the following, the further detailed analysis regarding the microstructural change with respect to the solute concentration is made.

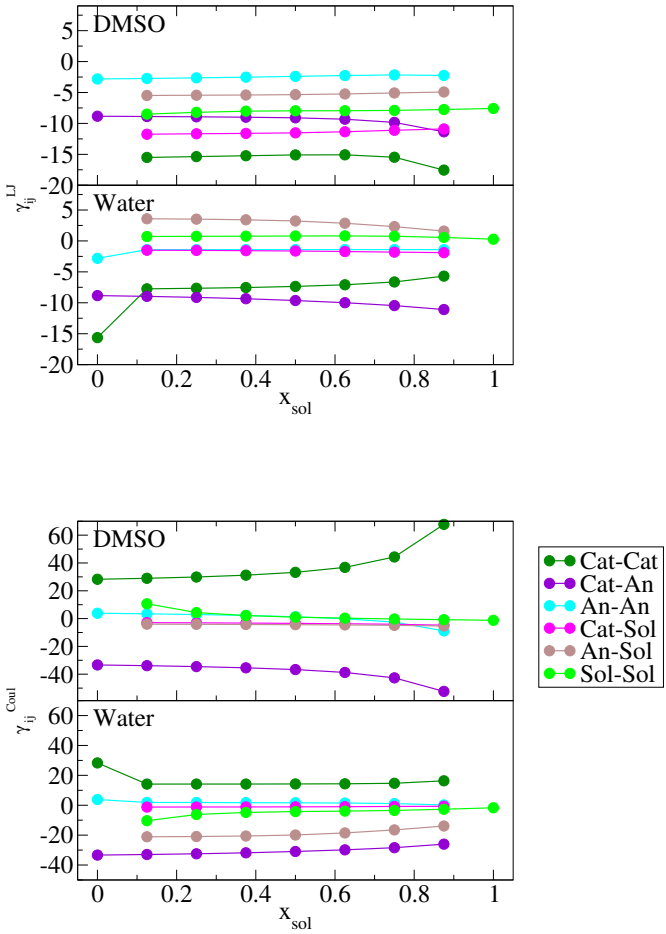

Figure 4.4: The effective interactions (top) $\gamma_{ij}^{LJ}(\mathrm{kJ}\cdot\mathrm{nm}^3/\mathrm{mol})$ and (bottom) $\gamma_{ij}^{Coul}(\mathrm{kJ}\cdot\mathrm{nm}^3/\mathrm{mol})$ between the species in the bulk DMSO-$[\mathrm{EMIM}]^+[\mathrm{DCA}]^-$ and water-$[\mathrm{EMIM}]^+[\mathrm{DCA}]^-$ mixtures at different solute concentrations. The species types and their combinations are labeled according to the legends. Copyright 2021 Wiley. Used with permission from Ref. 105.

First, the effective interaction energies between the species in the solutions as calculated through Eqn.(3.25) are further divided into the contributions from Lennard-Jones and Coulomb interactions. The results of the bulk solutions for all IL mixtures throughout the solute concentration range are summarized in Fig.4.4. As a first observation, in the Fig. 4.4 (top) the DMSO has stronger LJ interaction with other species due to the larger size than water molecule. The main difference between the DMSO mixtures and the water mixtures is found in the cation-cation interaction (dark green lines with circle symbols). While the DMSO mixtures show decreasing trend, the water mixtures show the opposite. Note, that the cation-DMSO interaction almost coincides with the anion-DMSO interaction in the bottom panel of this figure and these two lines seem to overlap. For the Coulomb interaction in the Fig. 4.4 (bottom), the interaction involving DMSO is decreasing while the water interaction is increasing with respect to the solute concentration. Moreover, the cation-cation interaction increases in the DMSO mixtures while in the water mixtures it decreases at $x_{\mathrm{sol}} = 0.125$ and reaches plateau. The cation-anion interactions show the opposite trends between the DMSO and water mixtures, which decreases in the DMSO mixtures and increases in the water mixtures. Furthermore, the strong anion-solute interaction in the water mixtures should be attributed to the hydrogen bonds between water and the anions as explained in the reminder of this chapter.

The comparison between the LJ and Coulomb interactions provides an insight on the strong contribution of LJ interaction to the difference in cation-

solute interactions between the DMSO and water mixtures. The cation-solute Coulomb interactions show a negligible difference, while the cation-DMSO has stronger LJ interaction than the cation-water. The repulsive DMSO-DMSO Coulomb interaction is significantly compensated by LJ interactions. Due to its small size water has negligible LJ interactions with other species. Water interacts mostly through Coulomb interactions with anions forming hydrogen bonds. According to these observations, the local ionic structure represented by the cation-anion interaction is strengthened in the DMSO mixtures by adding DMSO and weakened in the water mixtures by adding water. In the DMSO mixtures, DMSO tend to strongly interact by the interactions such as dipole-charge or dipole-dipole interactions with other molecules in a longer range than water molecules do. This is due to the fact that the dipole moment of 4.42D for DMSO is larger than the value of 2.35D for water, as calculated from the simulations. Note, that the respective experimental values are 3.960D for DMSO and 1.855D for water [1]. Although these values from simulations deviate from the experimental values, the difference between DMSO and water must be still captured. These trends in the dipole moments and the strong hydrogen bonds between water and anions are linked with the observation that the solute molecules in the second solvation shell around each species contribute more to the dipole interactions in the case of DMSO compared to water. DMSO interacts with other molecules equally within a distance of 1 nm. Water, though, interacts strongly in the close vicinity but weaker in larger distances. Therefore adding solutes does not require a rearrangement of the

local ionic structure in the case of the DMSO mixtures, but requires a local rearrangement of ions in the water mixtures as discussed later in this chapter.

4.2.2 Radial distribution functions

These trends can be confirmed by the radial distribution functions (rdfs) depicted in Fig.4.5. In the (top) panel of this figure the rdfs for cations-anions are depicted, while in the (bottom) panel the ion-ion rdfs are shown. For the latter, united ions description is used, where both the cations and anions are considered as ions. The cation-anion rdfs capture the interaction between direct cation-anion pairs. On the other hand, the ion-ion rdfs provide more insights into the total ionic structure of the IL mixtures by including also the contributions from the cation-cation or anion-anion rdfs. An comparison of the cation-anion rdfs in the (top) panel reveals an interesting trend in the first peaks. For water and DMSO the first peaks in the cation-anion rdfs are found at 0.4 nm at $x_{\mathrm{sol}} > 0.625$ in water mixtures and 0.6 nm for the rest of the cases. At first, this shows the more closely bound ion-pair in water compared to the case in DMSO. However, in the case of DMSO mixtures, the cation-anion rdfs have their first peaks at the same position for all DMSO concentrations. The first peaks increase with the DMSO concentration, showing that the cation-anion ion pairing persists. This can be seen in a decreasing cation-anion effective interaction energies for DMSO mixtures in Fig.4.3 (dark green line with filled circle symbols). In the case of the water mixtures, increasing the concentration of water leads to a shift of the first cation-anion peaks to shorter distances

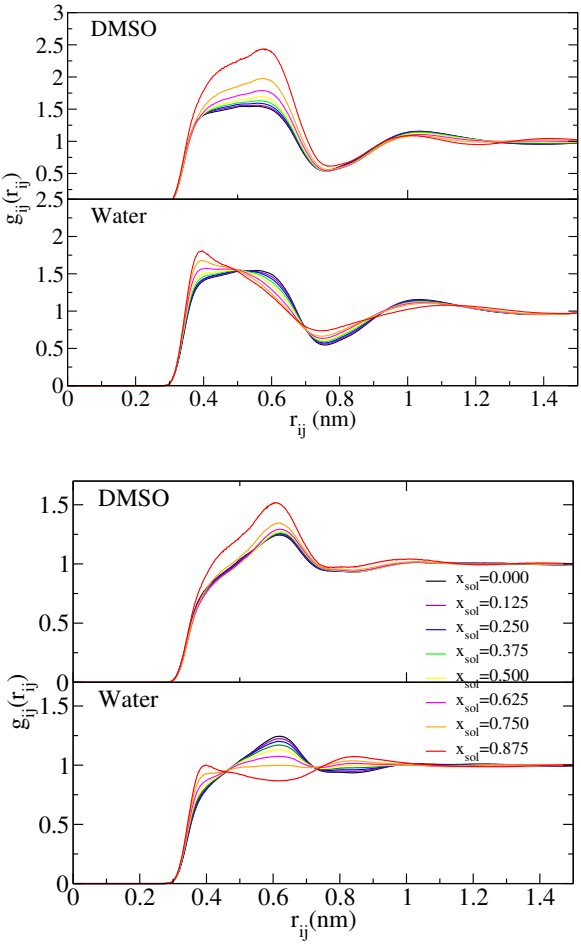

Figure 4.5: The (top) cation-anion and (bottom) ion-ion radial distribution functions in the DMSO-$[EMIM]^+[DCA]^-$ and the water-$[EMIM]^+[DCA]^-$ mixtures for the whole range of solute concentrations as described in the legend. Copyright 2021 Wiley. Used with permission from Ref. 105.

(0.6 nm -> 0.4 nm), while the number of the molecules within the first peak (0.3 $\sim$ 0.7 nm) remains almost constant, which indicates that the amount of associated cation-anion pairs decreases in the same manner as the decrease of ionic concentration in bulk. The water molecules, which increase in number, are mixed with the ILs, so that they only change the favorable orientation between the cations and the anions, which reflects the shift of the first peak. The change in effective cation-anion interaction confirmed through the results in Fig.4.4 is based on the persistent ion pairs in the DMSO mixtures and the orientational change in the water mixtures. Further analysis on the rdfs between center of mass of the cation and each atom in anion (atomic labels are shown in Fig. 4.9) reveals additional details on the orientational change of anions around the cation in Fig. 4.6.

Based on this figure, as the solute concentration increases, the peaks of the rdfs between cation and each atom in the anion in DMSO-mixtures increase in the same manner. On the other hand, in water mixtures, there is distinct difference in the rdf between cation and N4/N5 atom in the anion compared to the rdfs between cation and the N1 or C2/C3 atoms. The first and the second peaks around 0.2 nm and 0.35 nm decrease and the third peak at 0.4 nm increases by increasing water concentration. This implies that the N4/N5 atoms lose the capability to interact with the cations in the high water concentration of $x_{sol} = 0.875$. This relates to the fact that the over-accumulation of the water molecules around those atoms disturb the interaction between cation and the anions. This is explained more in detail in the following preferential position

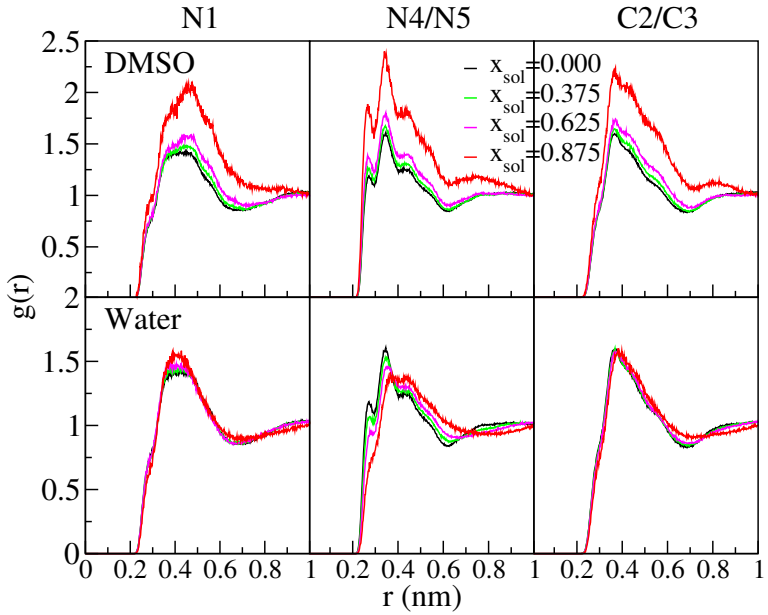

Figure 4.6: The radial distribution functions between center of mass of the cation and the atoms in the anion. (Top panels) DMSO-$[EMIM]^{+}[DCA]^{-}$ mixtures and (bottom panels) water-$[EMIM]^{+}[DCA]^{-}$ mixtures. The results for the cation-N1 atoms (left) , cation-N4/N5 atoms (center) and cation-C2/C3 atoms (right) for each mixture are depicted as a function of the solute concentrations defined in the legend. Copyright 2021 Wiley. Used with permission from Ref. 105.

analysis later in the chapter. In the ion-ion rdfs in the (bottom) panel in Fig. 4.5 for the water mixtures, the first peak shifts to shorter distances at high water concentrations (0.6 nm -> 0.4 nm), while the peak height converges to unity. This shift of the first peak and the decreasing peak value attribute to the change in the favorable orientation between cations and anions and the weakened ionic interactions including all cation-anion, cation-cation and anion-anion interactions. On the other hand, in DMSO mixtures, no shift of the peak position (0.6 nm) is observed, while the height increases by increasing DMSO concentration. This trend implies that the cation-anion pair and the interactions between these pairs remain stable even by increasing DMSO concentration.

4.2.3 Potential of mean forces

Next, in order to estimate the free energy with respect to the distance between the ions, the potentials of mean forces (PMF) between cation and anion, and between ion and ion are calculated from the radial distribution functions in Fig.4.7 using the following equation

$$A(r) = -k_B T \ln \frac{g_{ij}(r)}{g_{ij}(r = \infty)} \tag{4.1}$$

with the Boltzmann constant k_B. As observed in this figure, in DMSO mixtures, a steep minimum at $r = 0.6$ nm occurs throughout the whole DMSO concentration range for both PMFs between cation and anion, and between ion and ion. As discussed in Ref. 149, this indicates that the ions are more

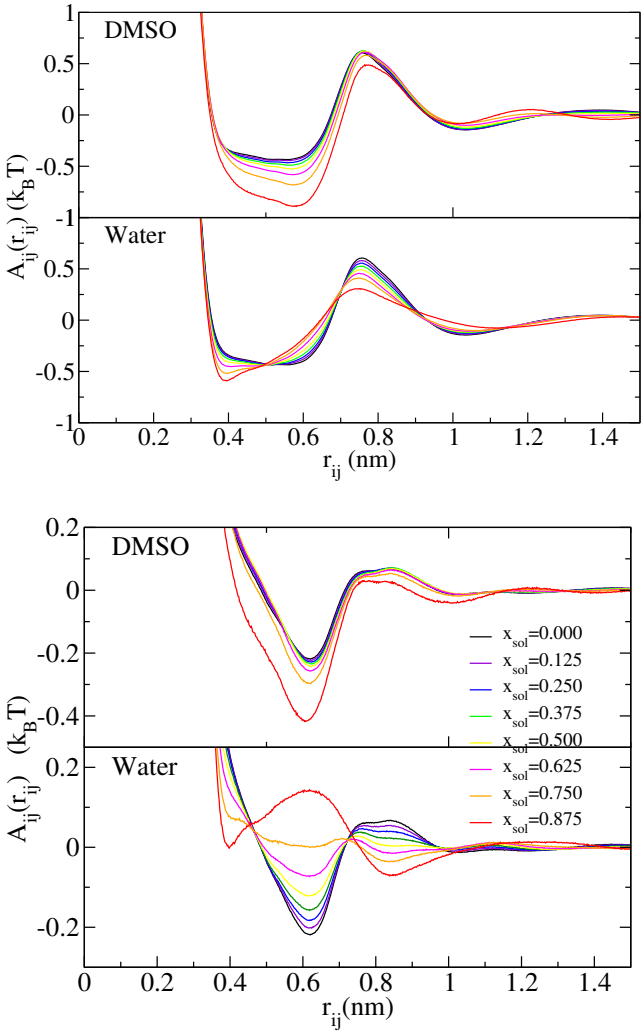

Figure 4.7: The potential of mean force between (top) cation and anion, and (bottom) ion and ion in the DMSO-$[EMIM]^+[DCA]^-$ and the water-$[EMIM]^+[DCA]^-$ mixtures for the whole range of solute concentrations as described in the legend. Copyright 2021 Wiley. Used with permission from Ref. 105.

associated at higher solute concentrations. A comparable behavior can be observed in IL-water mixtures for cation-anion PMF. However, for the ion-ion PMF water mixtures shows distinct difference. Up to $x_{sol} = 0.625$, where the ions show a pronounced negative PMF at the nearest minimum at $r = 0.6$ nm, while at $x_{sol} = 0.750$, the local minimum at $r = 0.6$ nm has a positive value and a new local minimum shows up at $r = 0.4$ nm, which naturally reflects the shift of the first peak of the rdf due to the relation between rdfs and PMFs. As a consequence, at this higher concentration, the local minimum at $r = 0.6$ nm turns to be a local maximum and the local minimum at $r = 0.4$ nm becomes more apparent. Furthermore, the value is always higher than unity, which explain the reason why ions are dispersed in the water mixtures at high water concentrations. Accordingly, higher water concentrations induce a significant rearrangement of the local composition around the ions. These results are in a quite good agreement with experimental observation [158].

4.2.4 Local/Bulk partition functions

Based on Eqn.(3.8), the local/bulk partition functions of solute around cation and anion for both mixtures are calculated in Fig.4.8. Both DMSO and water mixtures reveal a decreasing trend in the height of the peaks (~0.5 nm for DMSO mixtures and ~0.3 nm for water mixtures) with respect to the solute concentration. This indicates a saturation of solute molecules near the ions even for very diluted mixtures ($x_{sol} = 0.125$). Regarding the decreasing values, it can thus be concluded that the added solute molecules tend to be located in

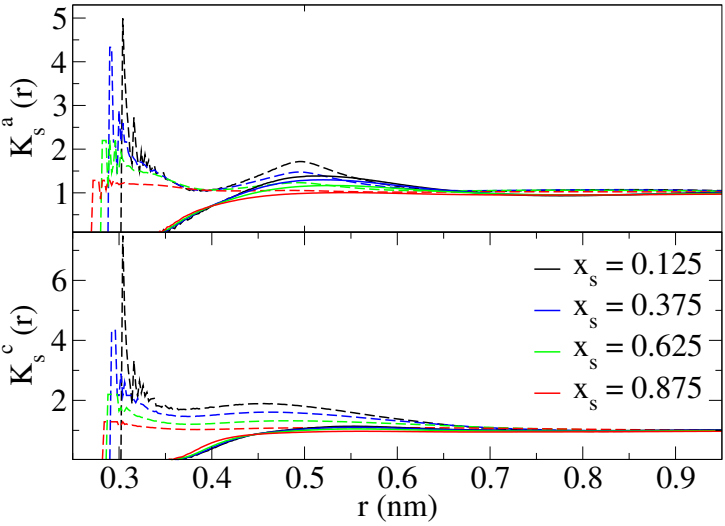

Figure 4.8: The local/bulk partition functions of solute molecules around cations (bottom) and anions (top) at different solute mole fractions. The solid lines correspond to the DMSO mixtures and the dashed lines to the water mixtures.Copyright 2021 Wiley. Used with permission from Ref. 105.

the bulk region instead in close distance to the individual reference molecules, namely ions in both the water and DMSO mixtures. However, there still exist distinct differences between DMSO mixtures and water mixtures. For example, because of the small size of the water molecules, these accumulate more than the DMSO molecules around the ions, which reflects the difference in the height of the first peaks. In addition, while $K^{i}_{sol} > 1$ holds even at the highest water concentration indicating the persistent preferential binding of water molecules to the ions, $K^{i}_{sol} < 1$ holds for the DMSO mixtures at the highest DMSO concentration $x_{\mathrm{sol}} = 0.875$ indicating the repelled behavior of DMSO molecules from the ions. These results support the conclusions obtained from the analysis in the effective interaction energies and their difference between the DMSO and water mixtures showing strengthened ion-ion interactions in the DMSO mixtures and the weakened ion-ion interactions in the water mixtures.

4.2.5 Preferential molecular positions

These observations are further related to the orientation of the species around other species. Distinct difference is again observed between DMSO and water mixtures as evident from Fig.4.10 for the solute molecules around the anions. In this figure, the preferential positions of the solute molecules around the anions are shown. Note, that in this and the following figures about the preferential positions, the probability depicted is calculated by the number of occurrences at each rectangular grid point with 0.1 nm distances and divided

by the total number of occurrences within 0.8 nm from the center of mass of the reference molecule. It is evident that the solutes accumulate differently in DMSO mixtures and water mixtures. In DMSO mixtures, DMSO molecules accumulate near the negative side of the dipole moment direction in anions at the whole DMSO concentrations. The dipole moment is calculated by

$$\vec{\mu} = \sum_i q_i(\vec{x_i} - \vec{x_c}), \tag{4.2}$$

where q_i is the partial charge of atom i in a molecule and $\vec{x_i}$ is the position of this atom. x_c is the center of mass of the molecule. The partial charges and the direction of the dipole moments are shown in Fig.4.9. The calculated values of $|\vec{\mu}|$ for each species are 1.77D for $[EMIM]^+$, 0.90D for $[DCA]^-$, 4.42D for DMSO, and 2.35D for water.

In water mixtures, the water molecules accumulate near the highly negatively charged atoms, namely N4/N5/N1 atoms. This difference between the DMSO and water mixtures arises from the different sizes of DMSO and water. The smaller water molecule can more flexibly reorient and find the positions, and thus interacts strongly with charged atoms. For the larger DMSO molecule, the interactions with neighboring ions are more dispersion interaction orientated, and thus orientational preferences are absent. Closer look at the localization effect reveals that it is stronger at low water concentrations, while it decreases as more water is added into the mixtures. The accumulation close to the two nitrogen atoms (N4/N5 atoms in Fig.4.9), can be understood

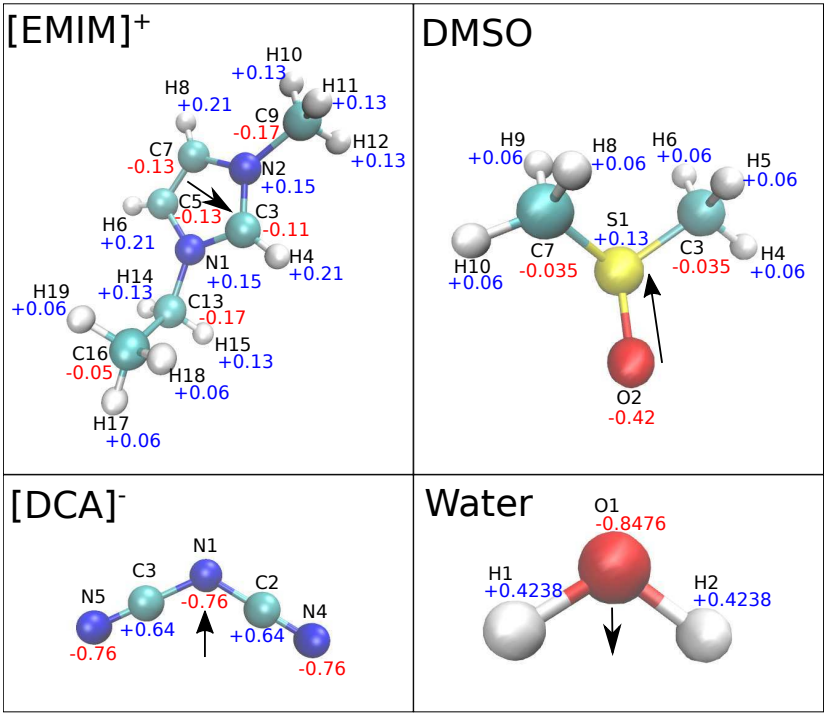

Figure 4.9: The partial charge distribution in the molecules. The dipole moments are shown as arrows on each molecule. Copyright 2021 Wiley. Used with permission from Ref. 105.

based on the fact that the hydrogen atom in water has the largest positive charge and these two nitrogen atoms in $[DCA]^-$ has the region of the highest negative charge including neighboring C2/C3 carbon atoms. In combination with the small size of water, these atoms interact strongly and form hydrogen bonds. The average numbers of the hydrogen bonds between the N4/N5 atom or N1 atom in $[DCA]^-$ and water molecule for different water concentrations are calculated in Table 4.1. At lower water concentrations, each water molecule forms nearly two hydrogen bonds with the N4 or N5 atom of $[DCA]^-$, which indicates that most of the water molecules are trapped between two $[DCA]^-$ molecules by forming hydrogen bonds with them. Apparently at lower solute concentration up to $x_{sol} = 0.5$ the water molecules accumulate near the N4/N5 atoms about ten times as much as near the N1 atoms. At high solute concentrations, the water accumulation near N4/N5 atom seems to be weakened compared to the increased accumulation near the N1 atoms, which is reflected at the ion-ion structural changes observed in the rdfs (Fig.4.5). This region has a total negative charge greater than -1 and interacts strongly with the cations. In fact, this charge is about -1.1838e arising from the N1 atom in $[DCA]^-$, the H1(H2), and O1 in water in Fig.4.9. In this way, water mediates the interaction between cation and anion due to the high electronegativity and chemical hardness, which leads to the strong affinity to the anion [188,189,190] and further leads to a weak cation-anion interaction in water mixtures. On the other hand, due to the smaller electronegativity, the preferential position of the species does not change in DMSO mixtures, leading to the cation-anion interaction remain-

ing strong. In the case of the preferential position of solute molecules around the cations, the results in Fig. 4.11 reveal that the positions of the highly localized area are clearly different between the DMSO and water mixtures. For water mixtures they are in plane of the imidazolium ring in the cation, while the DMSO accumulate at the top/bottom of the imidazolium ring. For the water molecules the localized area can be interpreted as near the nitrogen atoms in anions localized in Fig. 4.13 (anions around the cation) implying that these localization is mediated by the accumulation of water around the anion due to the much stronger interaction of water with anions. Accordingly, it can be concluded that the weakening of the ionic structure in the water mixtures occurs due to the strong accumulation of water around anions, thereby leading to the weak cation-anion interactions.

Table 4.1: The average numbers of hydrogen bonds per N4/N5 atom or N1 atom in $[DCA]^-$ molecules and water molecules at different water concentrations. For the atom labeling refer to Fig.4.9.

	Mole fraction of solute x_{sol}						
	0.125	0.250	0.375	0.500	0.625	0.750	0.875
Number of hydrogen bonds per N4/N5 atom	0.132	0.295	0.503	0.764	1.085	1.490	2.073
per N1 atom	0.008	0.020	0.039	0.074	0.149	0.320	0.705
per water molecule	1.900	1.833	1.741	1.603	1.391	1.100	0.693

Regarding the preferential position of the anions around the cations in Fig. 4.13, at $x_{sol} = 0.000$, the preferential position of the anion is close to that of

Table 4.2: The average numbers of hydrogen bonds per C5/C7 atom or C3 atom in $[EMIM]^+$ molecules and water molecules at different water concentrations. For the atom labeling refer to Fig.4.9.

	Mole fraction of solute x_{sol}						
	0.125	0.250	0.375	0.500	0.625	0.750	0.875
Number of hydrogen bonds per C5/C7	0.014	0.029	0.046	0.068	0.094	0.127	0.175
per C3 atom	0.013	0.028	0.047	0.071	0.101	0.141	0.201

the highest positively charged region as depicted in Fig. 4.9. This preference does not change qualitatively with respect to the DMSO concentration. However, in the water mixtures at the highest water concentration ($x_{sol} = 0.875$), the localization area of anion is shifted to the top/bottom of the imidazolium ring. This shift reflects the peak shift of the cation-anion rdfs in Fig. 4.5. On the other hand, the preferential positions of the cations are close to the negatively charged side of the anion in Fig. 4.12. These preferential positions do not change with the addition of either DMSO or water even at high concentrations other than at the highest water concentration at $x_{sol} = 0.875$. At $x_{sol} = 0.875$ in the water mixtures, the preferential position is localized more on the top/bottom of the plane of the anion triangle, which is again the manifestation of the peak shift of the cation-anion RDFs in Fig. 4.5.

In order to analyze the DMSO-cation interactions, the average number of weak hydrogen bonds (C-H–O) between C3, C6 and C7 atoms in $[EMIM]^+$ as the donor and O2 atom in DMSO as the acceptor in Fig. 4.9 (the donor-acceptor distance is < 0.32 nm and the angle is $< 90°$ as stated in Ref. 196) is calculated. In Table. 4.2 the average number of weak hydrogen bonds between

$[EMIM]^+$ (C6/C7/C3) and DMSO (O2) for different DMSO concentrations is summarized. Although there is a slight difference between the C6 and C7 atoms in $[EMIM]^+$ due to the asymmetric shape of $[EMIM]^+$, these atoms are treated similarly due to the systematic constraint. It has been reported that the attachment of DMSO to these atoms via weak hydrogen bonds weakens the cation-anion interaction in the imidazolium-based ionic liquids [199]. The simulation results reveal the similar trends to the result from Ref. 199 regarding an increasing trend of average hydrogen bonds with respect to the DMSO concentration. However, the simulation results conclude the opposite, which is that the attachment of DMSO to the cations does not weaken the anion-cation interaction but the anion-cation interaction is strengthen even if the attachment of DMSO to cations increases. The increasing hydrogen bonds stems from the increasing DMSO concentration. Anion-cation interactions are not disturbed by this due to the nature of the DMSO-cation interactions as inferred from Fig. 4.4, in which the Lennard-Jones contribution is much higher than the Coulomb contribution in the cation-DMSO interaction due to the large size of the cation and DMSO. As a final remark, the structural change around each molecule in DMSO-$[EMIM]^+[DCA]^-$ mixtures with respect to the solute concentration is negligible as can be observed from the Figs. 4.10, 4.11, 4.12 and 4.13.

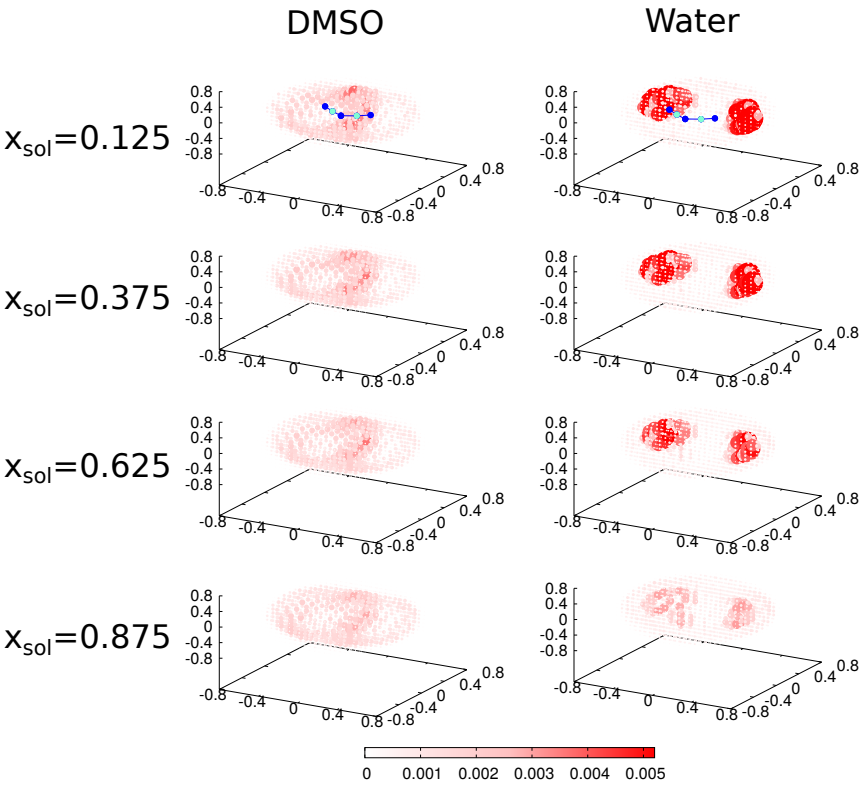

Figure 4.10: The preferential positions of the solute molecules around the anion for both solutes at different concentrations as denoted by the legends on the left. The red colors and larger spheres denote a higher occurrence probability of the molecules. Copyright 2021 Wiley. Used with permission from Ref. 105.

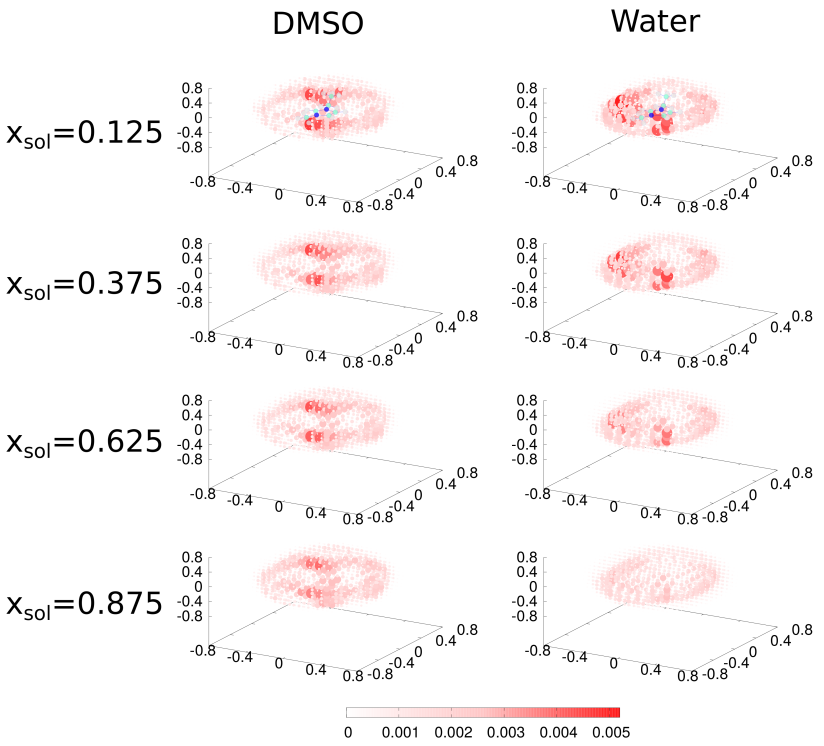

Figure 4.11: The preferential positions of the solute molecules around the cation for both solutes at different concentrations as denoted by the legends on the left. The red colors and larger spheres denote a higher occurrence probability of the molecules. Copyright 2021 Wiley. Used with permission from Ref. 105.

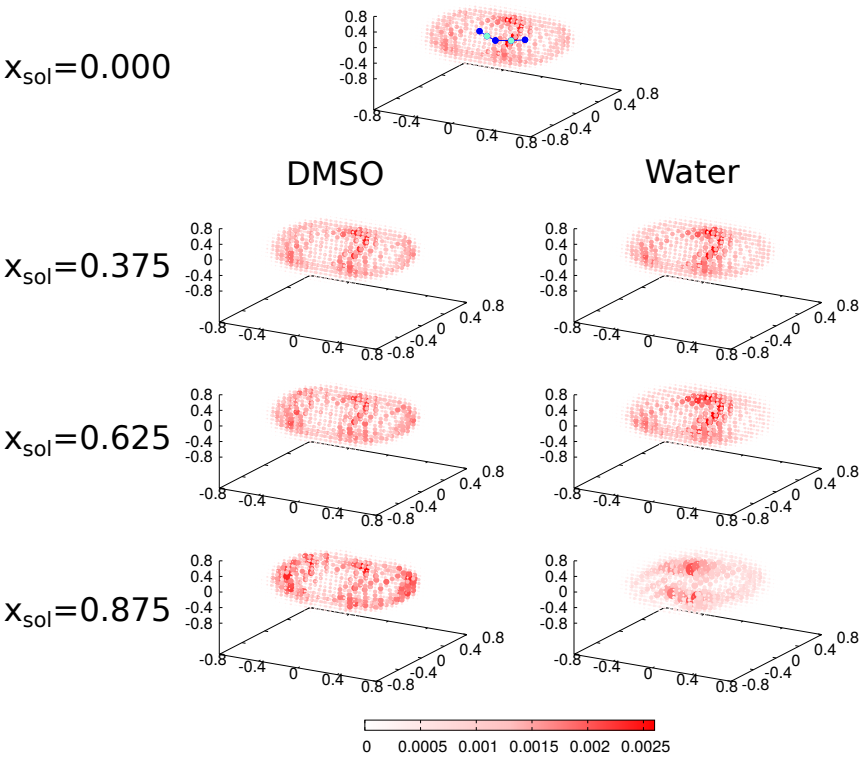

Figure 4.12: The preferential positions of the cations around the anion for DMSO-$[EMIM]^{+}[DCA]^{-}$ and water-$[EMIM]^{+}[DCA]^{-}$ mixtures at different solute concentrations as denoted by the legends on the left. The red colors and larger spheres denote a higher occurrence probability of the molecules. Copyright 2021 Wiley. Used with permission from Ref. 105.

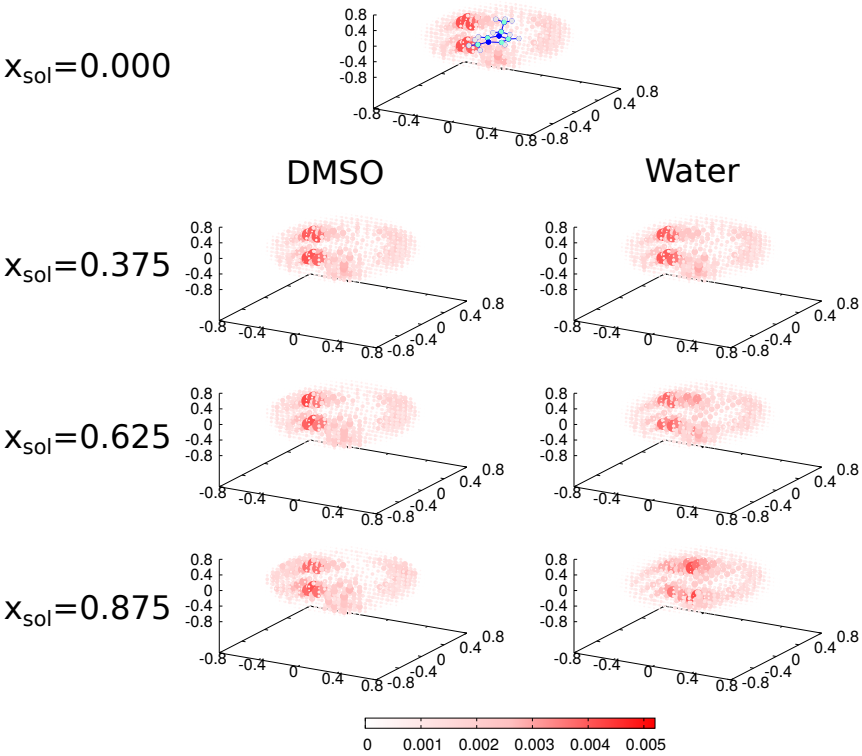

Figure 4.13: The preferential positions of the anions around the cation for DMSO-$[EMIM]^{+}[DCA]^{-}$ and water-$[EMIM]^{+}[DCA]^{-}$ mixtures at different solute concentrations as denoted by the legends on the left. The red colors and larger spheres denote a higher occurrence probability of the molecules. Copyright 2021 Wiley. Used with permission from Ref. 105.

4.3 Summary and Conclusions

In this chapter, the microstructural change in bulk DMSO-$[EMIM]^+[DCA]^-$ mixtures and water-$[EMIM]^+[DCA]^-$ mixtures with respect to the solute concentration is studied. The preferential binding behaviors of the molecules calculated by Kirkwood-Buff theory and the effective interaction energy draw the same conclusion, which proves the validity of the argument of the effective interaction energy. The DMSO mixtures and water mixtures show distinct differences in the microstructural changes. It is revealed that in DMSO mixtures the cation-anion interactions increase by adding DMSO, but decrease in water mixtures by adding water. This attributes to the fact that the cation-anion pairs are weakly bonded in water mixtures at high water concentrations and strongly bonded in DMSO mixtures even at high DMSO concentrations. These differences can be explained by the higher electronegativity and chemical hardness of water compared to DMSO leading to the strong interaction of water with $[DCA]^-$ by hydrogen bonds disturbing the cation-anion interaction. These results highlight the fact that the charge distributions of the molecules play an important role in the interaction between the species in IL-solute mixtures, which in the end leads to the dispersion oriented interaction of DMSO with other molecules and strong hydrogen-bonded interaction of water with anions, which in the end mediate the anion-cation interactions in the mixtures. In principle, the solute molecules, which have a high electronegativity like water,

interact strongly with ions containing highly charged atoms (in this case $[DCA]^-$) by the Coulomb interaction or hydrogen-bonds in this case. On the other hand, the solute molecules, which have a low electronegativity such as DMSO interact with the charged particles by the dispersion interactions leading to the weak disturbance on the ion-pair, which is interacting by the strong Coulomb interaction. Accordingly, as a main finding, in order to maintain an optimal interaction between ions, the solute molecules with low electronegativity such as DMSO is a proper choice for practical applications requiring the persistence of ion pairs. On the oder hand, in order to break an interaction between ions, the solute molecules with high electronegativity such as water is a proper choice. These results serve an important insight onto the optimal design of IL-solute combination and the solute concentration for specific purposes.

5

Ionic Liquids in Confinement between Neutral Surfaces

5.1 Motivation

In this chapter, the focus is given on the microscopic structure of IL-solute mixtures in confinement between flat, structure-less, and neutral surfaces, especially on the structural change at the interfaces (IFs) with respect to

the solute concentration. Specifically, the mixtures of $[EMIM]^+[DCA]^-$, $[EMIM]^+[BF_4]^-$ and $[BMIM]^+[BF_4]^-$ as ILs and water as solute with water concentration in the range of $x_{H_2O} = 0$ to 1 between flat, uncharged, silicon surfaces separated by the distance of 14.5 nm are studied in order to analyze the structure of three different ILs. A snapshot of the simulation and the molecules studied in this chapter is shown in FIG.5.1. The other simulation details are explained in Appendix. A.2. In case of the practical applications

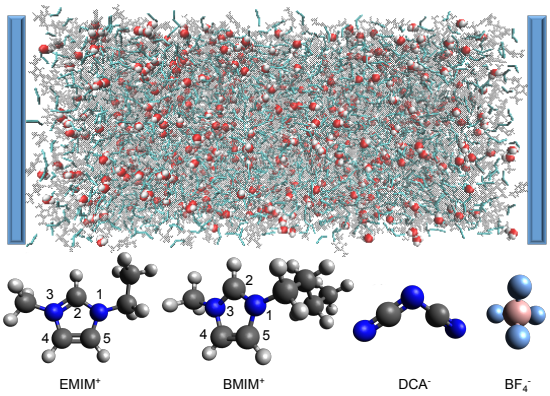

Figure 5.1: Top: A snapshot of a water-$[EMIM]^+[DCA]^-$ mixture with a water mole fraction of $x_{H_2O} = 0.25$. The uncharged silicon walls are represented through the blue boxes on either ends of the figure. Water molecules are shown in a van-der-Waals representation, whereas $[DCA]^-$ is colored in cyan and $[EMIM]^+$ in gray. Bottom: The molecular structures of the $[BMIM]^+$ and $[EMIM]^+$ cations with labels for atoms in the imidazolium ring. The molecular structure of the anions $[DCA]^-$ and $[BF4]^-$ is depicted on the right side. Hydrogen, nitrogen, and carbon atoms are colored in white, blue, and gray, respectively. The fluoride atoms in $[BF4]^-$ are represented as light blue spheres, whereas the central boron atom is colored in light red. Reprinted with permission from Ref. 102.

of the ILs, the reactions occurring at IFs play a significant role. A representative example within battery applications is the IFs between electrodes and

electrolytes. The red-ox reactions occurring at these IFs, as well as the transport properties of the electrolyte, govern the total performance of the battery. The microscopic structure at IFs is a basis of the red-ox reactions and thus, the study of the structure is attracting research attention. Furthermore, the addition of solutes into ILs causes a structural change at the IFs, in a similar manner as bulk ILs discussed in the previous chapter. Despite that the charged surface is more realistic for the battery application, which is discussed in the next chapter, the study of the neutral surfaces itself has importance in some applications such as lubricants for example. In terms of fundamental research, the accumulation behavior of solutes should be divided into the influence of the physical existence of the surface, and other surface properties, one of which is the surface charge in this thesis, in order to elucidate the microscopic mechanism of the accumulation of solutes at the IF. All outcomes in this chapter highlight entropically-driven accumulations of water molecules in front of neutral surfaces. It is revealed that the local water density depends crucially on the water concentration, local ordering effects, and the molecular structure of the ionic liquids (ILs). Additionally, the influence of hydrophobicity/hydrophilicity and the size of the ions play important roles as well. The outcome of this study defines a reliable criteria for beneficial water-IL combinations in view of selected applications.

5.2 Results

5.2.1 Local normalized atomic number density and the water/ion fractions at interface

First, in order to explain the basic difference between different ILs, the local normalized atomic number densities $\rho_{IL}^{N}(z) = \rho_{IL}(z)/\rho_{IL}^{bulk}$ of the combined cations and anions of three different neat ILs ($x_{H_2O} = 0$), are shown in Fig. 5.2, where ρ_{IL}^{bulk} denotes the ion density in the middle of the box (bulk phase at $z \approx 7.25$ nm from the surface) and $\rho_{IL}(z)$ is the local ion number density at a distance z from the wall. This figure reflects the difference of the molecular structure between different ILs at the solid-liquid interface. As can be seen, layer structures described as the density peaks disappear around $z \approx 1.5 - 2$ nm converging to the bulk behavior, which shows a good agreement with previous findings for other ILs[119,121]. At the first peak ($z \approx 0.25$ nm from the surface), the highest ion density can be observed for $[EMIM]^+[DCA]^-$, followed by $[EMIM]^+[BF_4]^-$ and then $[BMIM]^+[BF_4]^-$. Additionally, $[EMIM]^+[DCA]^-$ also shows shortest distances between the peaks, which points to the highest ionic packing fraction of $[EMIM]^+[DCA]^-$. Since the density profiles for $[EMIM]^+[BF_4]^-$ and $[BMIM]^+[BF_4]^-$ show a similarity, it can be inferred that anions may determine the different density distributions and packing fractions. Furthermore, it should be noted that the height of the first peak at around $z \approx 0.25$ nm in $[EMIM]^+[DCA]^-$ is significantly higher ($\rho_{IL}^{N}(z) \approx 2.5$) compared to the other ILs ($\rho_{IL}^{N}(z) \approx 2.0$). This can

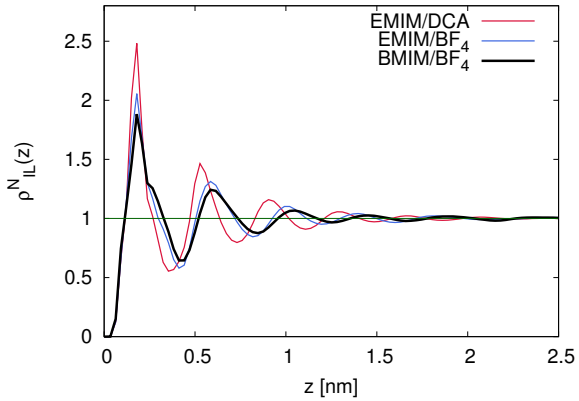

Figure 5.2: Normalized local atomic number density $\rho_{IL}^{N}(z)$ of the combined cation and anion species in neat ILs with $x_{H_2O} = 0$ at distances z from the wall for $[EMIM]^+[DCA]^-$ (red line), $[EMIM]^+[BF4]^-$ (blue line), and $[BMIM]^+[BF4]^-$ (black line). The green horizontal line shows ideal bulk value behavior with $\rho_{IL}^{N}(z) = 1$. Reprinted with permission from Ref. 102.

be attributed to the spatial orientation of flat-shaped $[DCA]^-$ anions, which enhances a more compact ion distribution near the solid/liquid interface.

This observation can be confirmed by the distribution of the individual ion species in the neat ILs as shown in Fig. 5.3. As can be seen, $[DCA]^-$ reveals a more ordered structure at short distance from the surface when compared to $[BF_4]^-$, thereby inducing a more compact ion layer structure. In more detail, $[DCA]^-$ ions orient parallel to the surface while $[BF_4]^-$ shows a wider first layer due to its spherical shape. The corresponding double-peak structure for $[BF_4]^-$ at the first and the second layers within $z \leq 0.7$ nm compared to $[DCA]^-$ can be attributed to the various orientations of the anion with the boron atom at the center preferably located at the center between the two peaks within each double peak. Thus, $[DCA]^-$ can be found in a more well-

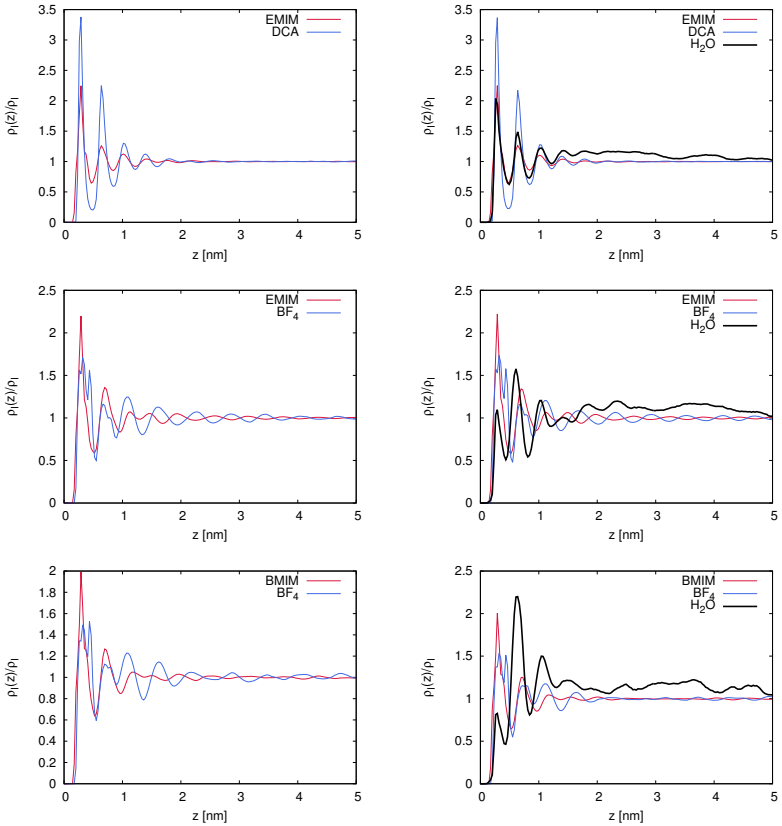

Figure 5.3: Normalized local atomic number density $\rho_{\mathrm{IL}}^{\mathrm{N}}(z)$ of the cation, anion and solute in (left) neat ILs and (right) at $x_{\mathrm{H_2O}} = 0.125$ at distances z from the surface for (top) $[\mathrm{EMIM}]^{+}[\mathrm{DCA}]^{-}$, (middle) $[\mathrm{EMIM}]^{+}[\mathrm{BF4}]^{-}$, and (bottom) $[\mathrm{BMIM}]^{+}[\mathrm{BF4}]^{-}$. Reprinted with permission from Ref. 102.

Table 5.1: Molecular volumes V_m and octanol–water partition coefficients $\log_{10}$ P for the individual ion species and water molecules as calculated by Ref. 137. $P = c^s_{C_8OH}/c^s_{H_2O}$ where $c^s_{C_8OH}$ and $c^s_{H_2O}$ denote the corresponding concentration of the ions in octanol and water phase. Molecular volumes are obtained by fitting the sum of fragment contributions for a training set of about twelve thousand molecules after optimization using the semiempirical AM1 method [47]. Reprinted with permission from Ref. 102.

Species	V_m [nm^3]	$\log_{10}$ P
$[EMIM]^+$	0.118	-3.10
$[BMIM]^+$	0.152	-2.04
$[DCA]^-$	0.056	-3.34
$[BF4]^-$	0.073	-2.60
H_2O	0.019	-0.29

ordered orientation parallel to the interfaces when compared to $[BF_4]^-$. Interesting is that the $[EMIM]^+$ distribution of $[EMIM]^+[DCA]^-$ is also more ordered than $[EMIM]^+$ from $[EMIM]^+[BF_4]^-$. Therefore, it can be inferred that the distribution of anions influences the distribution of cations and *vice versa*. Therefore, It can be assumed that the differences in the density profiles between these three ILs can be mainly assigned to the molecular size, as well as the planar ($[DCA]^-$) or spherical ($[BF_4]^-$) shape and arrangement of the anions.

Regarding this assumption, the values for the molecular volumes V_m of all ions (Tab. 5.1) support this assumption. The smaller sizes of $[DCA]^-$ and $[EMIM]^+$ in comparison to $[BF_4]^-$ and $[BMIM]^+$ are apparent and thus rationalize a higher local packing fraction for $[EMIM]^+[DCA]^-$ compared to the other ILs. Moreover, smaller ions also reveal a lower hydrophobicity, thereby showing the following ordering $[DCA]^- > [EMIM]^+ > [BF_4]^- >$

$[BMIM]^+$ with decreasing polarity. Hence, it can be expected that $[DCA]^-$ and $[EMIM]^+$ show a stronger water binding behavior compared to $[BF_4]^-$ and $[BMIM]^+$. Interestingly, the distribution of the ions does not significantly change for low water contents of $x_{H_2O} = 0.125$ compared to neat ILs as can be seen in Fig. 5.3, which can be observed in bulk IL/water mixtures in the previous chapter. The position of the ion layers remains nearly identical and the long-range decay of layering structure differs slightly.

To compare the water accumulation behavior at the IFs between different water concentrations and different ILs, the water fraction $K_{H_2O}(\Delta)$ in the first layer within distances $z \leq \Delta$ is calculated by

$$K_{H_2O}(\Delta) = \frac{\rho_{H_2O}(\Delta)}{\rho_{all}(\Delta)}, \tag{5.1}$$

where Δ denotes the distance at the first minimum in the local total number density $\rho_{all}(\Delta) = \rho_{IL}(\Delta) + \rho_{H_2O}(\Delta)$ with $\Delta = 0.38$ nm for $[EMIM]^+[DCA]^-$ and $\Delta = 0.44$ nm for $[EMIM]^+[BF_4]^-$ or $[BMIM]^+[BF_4]^-$ respectively, such that the molecules within the first layer are considered in the calculations. The result is shown in Fig. 5.4.

As intuitively understood, the water fraction increases with respect to the water concentrations. The water fraction is in the order of $[EMIM]^+[DCA]^-$ > $[EMIM]^+[BF_4]^-$ > $[BMIM]^+[BF_4]^-$. At high water concentrations, with the definition $K_{IL}(\Delta) = 1 - K_{H_2O}(\Delta)$, the local fraction of ions $K_{IL}(\Delta)$ at $x_{H_2O} \geq 0.98$ is the highest for $[BMIM]^+[BF_4]^-$ ($K_{IL}(\Delta) = 0.52$), followed

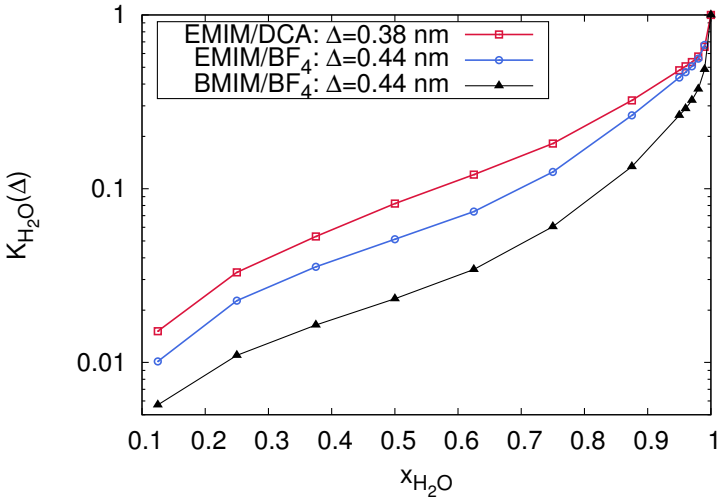

Figure 5.4: Fraction of water molecules $K_{H_2O}(\Delta)$ for all water mole fractions x_{H_2O} in the first solvent shell at wall distances $z \leq \Delta$. The results for $[EMIM]^+[DCA]^-$, $[EMIM]^+[BF4]^-$, and $[BMIM]^+[BF4]^-$, are shown in red (squares), blue (circles), and black (triangles), respectively. Reprinted with permission from Ref. 102.

by $[EMIM]^+[DCA]^-$ ($K_{IL}(\Delta) = 0.34$) and $[EMIM]^+[BF_4]^-$ ($K_{IL}(\Delta) = 0.33$). According to these values, a significant amount of ions accumulates at short distances in front of the surface. As a specific example, the local number densities of ions and water molecules for a very high water concentration at $x_{H_2O} \geq 0.980$ are shown in Fig. 5.5.

5.2.2 Translational order parameter

In order to explain theoretically the above mentioned observations about the accumulation of water/ions in front of the surface, a translational order parameter O_z^{IL} for species α, either combined anions and cations (index 'IL') or water molecules (index 'H_2O') is introduced to analyze how the ionic structure in front of the surface is ordered using the following equation [102]:

$$O_z^{IL} = \frac{2x_{IL}}{L_z} \int_0^{L_z/2} dz \left(\left[\gamma_{IL}(z) \ln \gamma_{IL}(z) \right] - \left[\gamma_{IL}(z) - 1 \right] \right), \qquad (5.2)$$

with $\gamma_\alpha(z) = \rho_\alpha(z)/\rho_\alpha^{bulk}$, which is closely related with the expression for the translational entropy as introduced in Ref. [204,226]. Note that, for a reliable evaluation of Eqn.(5.2), a bulk behavior with $\gamma_\alpha(z) \approx 1$ for $z \to L_z/2$ has to be guaranteed. In the simulations, this is guaranteed by setting enough large distances between the walls ($L_z = 14.5$ nm). As a consequence, the corresponding value of O_z^α provides an estimate for the degree of translational ordering with regard to the species α.

The corresponding values of O_z^{IL} in Fig. 5.6 for neat ILs ($x_{H_2O} = 0$)

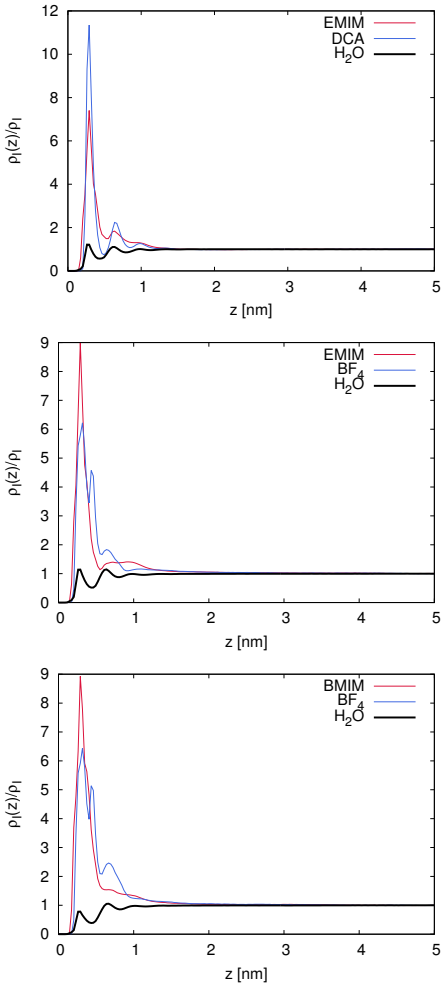

Figure 5.5: Normalized local atomic number density $\rho_{\mathrm{IL}}^{\mathrm{N}}(z)$ of the cation, anion and solute at $x_{\mathrm{H_2O}} = 0.980$ at distances z from the surface for (top) $[\mathrm{EMIM}]^{+}[\mathrm{DCA}]^{-}$, (middle) $[\mathrm{EMIM}]^{+}[\mathrm{BF4}]^{-}$, and (bottom) $[\mathrm{BMIM}]^{+}[\mathrm{BF4}]^{-}$. Reprinted with permission from Ref. 102.

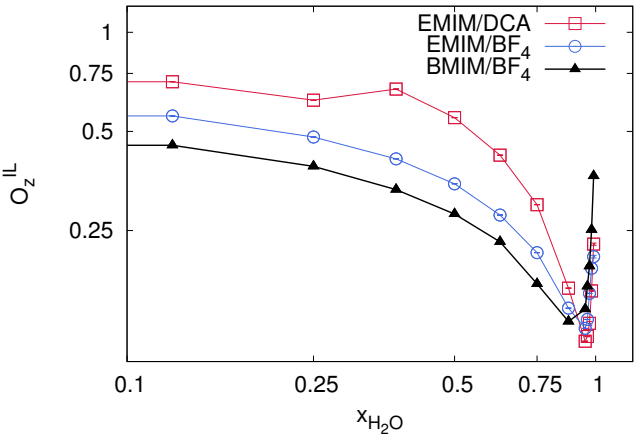

Figure 5.6: Order parameter values O_z^{IL} for combined ions at various water mole fractions x_{H_2O}. Reprinted with permission from Ref. 102.

are 0.82 for $[EMIM]^+[DCA]^-$, 0.63 for $[EMIM]^+[BF_4]^-$ and 0.51 for $[BMIM]^+[BF_4]^-$, which demonstrates that the highest degree of order of the ionic structure is given for $[EMIM]^+[DCA]^-$, followed by $[EMIM]^+[BF_4]^-$ and $[BMIM]^+[BF_4]^-$. Although the order parameter decreases significantly for all ILs with increasing water concentration, implying an increase of the translational entropy, the corresponding values reveal that up to a very high water concentration of $x_{H_2O} = 0.9$ the corresponding order between three different ILs remains identical to the case of neat ILs, namely $[EMIM]^+[DCA]^-$ > $[EMIM]^+[BF_4]^-$ > $[BMIM]^+[BF_4]^-$. In contrast, at higher water mole fractions $x_{H_2O} \geq 0.92$ the order parameter increases for all three ILs. A more detailed explanation for these observations and differences between the ILs will be presented in the reminder in this chapter. Further analysis of the order pa-

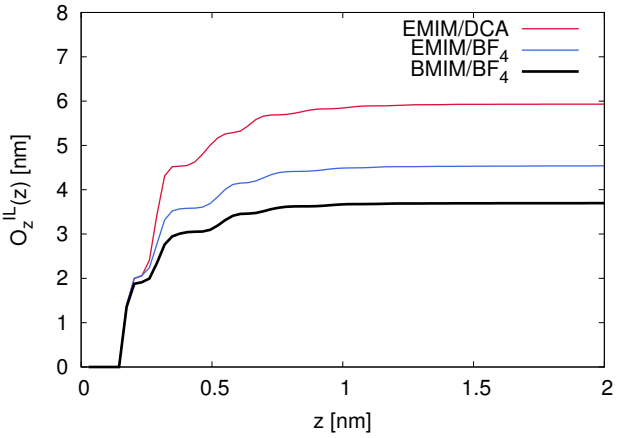

Figure 5.7: Running order parameter values O_z^{IL} for combined ions in neat ILs. Reprinted with permission from Ref. 102.

rameter with respect to the distance from the surface $O_z^{\alpha}(z)$ in Fig. 5.7 for neat ILs implies that the largest contributions to the integral in Eqn.(5.2) come from short distances of up to 1 nm in front of the surface. In contrast, the contributions from large distances are rather negligible such that O_z^{IL} converges to constant values for all $z > 1$ nm. This analysis reveals that the highest ordering of ion species and *vice versa* the lowest translational entropy[204] can be attributed to the ionic structure at the interfacial regions upt to $\sim$ 1 nm from the surface. Accordingly, the neat IL $[\text{EMIM}]^+[\text{DCA}]^-$ with the highest local ionic translational order, or the lowest translational entropy, is related to the highest water content. The correlation between the water fraction and the translational order parameter net differences at the interface remains valid up to water concentration of $x_{\text{H}_2\text{O}} \leq 0.75$, implying the robustness of this observation. This is an important indication that water accumulation at the interface follows the

order of the translational order parameter between different ILs. Accordingly, the water accumulates at the IF in order to increase the translational entropy, in other word, in order to decrease the free energy by increasing the mixing entropy up to the high solvent concentration of $x_{H_2O} = 0.75$. These observation agreed well with the experimental results [102].

As a result, following rational conclusions are drawn. At a low water concentration, the packing density as well as the ordering of the ions for all ILs is very high. The largest contributions to the translational order parameter come from the region at the interface in front of the surface. As a consequence, the translational entropy is very small there. However, the presence of water not only lowers the ion translation entropy, but also leads to a beneficial increase in the local mixing entropy at the interfaces. Accordingly, as the amount of water becomes larger, the entropy of mixing becomes larger partially compensating for the unfavorable translational entropy. This contribution is in the following order of $[EMIM]^+[DCA]^-$ > $[EMIM]^+[BF_4]^-$ > $[BMIM]^+[BF_4]^-$, respectively, rationalizing the high amount of water at the interface for highly ordered ILs. The reason for the highest ordering and packing fraction of $[EMIM]^+[DCA]^-$ is largely due to the small size, the planar shape, and the high polarity of the ions when compared to the other ILs (Tab. 5.1).

5.2.3 Kirkwood-Buff integrals

Further analysis is done by applying Kirkwood-Buff theory, namely, by calculating the Kirkwood-Buff integrals (KBIs) between the surface and the ions /water in the solution mixtures using the equation Eqn.(3.2). Note that, originally KBIs are calculated in three dimensional homogeneous bulk using radial distribution functions which converges to unity at the distance corresponding to the bulk. In order to apply KB integrals to the analysis of the structure in front of the surface, slight modification to incorporate the one-dimentional and distant-dependent nature of the local density profiles of the species in front of the surface is needed as follows [101,15,153,187] .

$$G_{W\alpha} = L_x L_y \int_0^{L_z/2} \mathrm{d}z \left[\gamma_\alpha(z) - 1\right] \tag{5.3}$$

Here, $G_{W\alpha}$ is the one dimensional KBI of the species α in front of the surface. L_x, L_y, and L_z are the simulation box length in x, y, and z direction respectively. $\gamma_\alpha(z)$ is the normalized density of species α as used in Eqn.(5.2), which converges to unity in the same manner as radial distribution functions. These values can be interpreted as excess volumes of species α at the IF compared to bulk. As discussed in the previous chapter, the preferential binding coefficient as an estimate for the hydration tendency of the surface is given by $\Gamma = \rho^0_{H_2O} \Delta V_{H_2O}$, where $\rho^0_{H_2O}$ denotes the total water density and $\Delta V_{H_2O} = G_{WH_2O} - G_{WIL}$ the corresponding differences between the water and the ion excess volumes. Positive values of Γ indicate a water attraction behavior and negative values a water

exclusion behavior of the surfaces, respectively. Since $\rho^0_{H_2O} \geq 0$, the positive or negative sign of Γ follows the sign of ΔV_{H_2O}. Therefore, $\Delta V_{H_2O} > 0$ implies a preferential attraction of water molecules to the surface, while $\Delta V_{H_2O} < 0$ points to an exclusion [187,144]. The corresponding results in Fig. 5.8 reveal positive values for ΔV_{H_2O} for all ILs below water concentrations $x_{H_2O} < 0.2$. The largest values of the excess volumes can be observed for $[BMIM]^+[BF_4]^-$. This finding is valid for low and moderate water content $x_{H_2O} < 0.5$ while for water concentrations at $x_{H_2O} > 0.9$ a steep decrease of ΔV_{H_2O} to highly negative values can be observed. The latter implies that a significant portion of water molecules is replaced by the ions as already shown in Fig. 5.5.

As a result for the high water concentration at $x_{H_2O} > 0.9$, as the water concentration increases, the role of the ILs changes from a solvent to solute, thereby changing accumulation tendency of the solute at the interface. The more hydrophobic properties of $[BMIM]^+$ and $[BF_4]^-$ when compared to the other species as represented by the octanol-water partition coefficients $\log_{10} P$ (Table. 5.1) as well as excess volumes in Fig. 5.8 prefer an accumulation of the ions at the interface in order to reduce the water-accessible surface area. In contrast, $[EMIM]^+$ and $[DCA]^-$ are more hydrophilic, which is in agreement with the lower accumulation tendency of $[EMIM]^+[DCA]^-$ compared to the other ILs. Thus, the accumulation behavior of the ions in water mixtures in front of the uncharged surfaces is mainly driven by hydrophobicity at the high water concentrations.

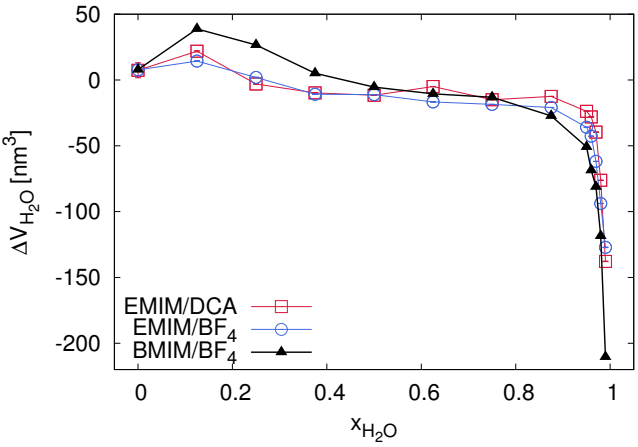

Figure 5.8: The differences in the excess volumes ΔV_{H_2O} for distinct water mole fractions x_{H_2O} in $[EMIM]^+[DCA]^-$ (red line with squares), $[EMIM]^+[BF4]^-$ (blue line with circles) and $[BMIM]^+[BF4]^-$ (black line with triangles). Reprinted with permission from Ref. 102.

5.3 Summary and Conclusions

The analysis done in this chapter reveals that the amount of water at solid/IL interfaces is higher for small and hydrophilic ion species compared to hydrophobic and large ions. This result is valid for all water concentration and can be explained by entropy-driven effects or the hydrophobicity of the ILs imposed by the molecular properties of the ions. In summary, the findings in this chapter shed more light on the hidden mechanism behind the distribution of water molecules in different ILs. Hydrophobic and bulkier ions show a lower packing fraction when compared to small and hydrophilic ions with highly ordered individual ion layers at up to high water concentrations. In terms of ILs with a high packing fraction, where water serves as solute, the presence of water

molecules results in the formation of a water-rich first shell in front of the interface due to the entropy driven accumulation. On the other hand, at high water concentrations, where water serves as solvent, the hydrophobicity of ions determines the accumulation of ions at the interface, which in turn determines the amount of water altered by hydrophobic ions at the interfacial area. The presence of water molecules at interfaces can be whether favorable or unfavorable, depending on the various technological applications. For example, for enzyme catalysis or electro catalysis, it is favorable to use hydrophilic ILs with small ions in order to increase the number of water molecules in front of the surface. On the other hand, at the interface between electrodes and electrolytes for battery devices water has to be reduced, bringing ILs with bulky and hydrophobic ions to the forefront. Finally, here, although the influence of uncharged interfaces is studied, similar effects can be observed for charged surfaces[64] and for other ILs[49]. The study in this chapter has highlighted similarities and differences, and has provided important insight into the underlying mechanisms of IL-water mixtures at interfaces, which leads to the optimal combination of water concentration and the IL species for specific purposes.

6

Ionic Liquids in Confinement between Charged Surfaces

6.1 Motivation

Here, the focus is given on unraveling the microstructural change of the IL-solute mixtures in front of charged surfaces with respect to the solute concentration. Specifically, the mixtures of $[EMIM]^+[DCA]^-$ as IL and wa-

ter/DMSO as solutes at solute concentrations in the range of $x_{sol} = 0$ to 1 confined between flat, charged surfaces with a surface charge of $\pm 0.2 C/m^2$ are studied. The molecular structures of the IL and solutes used in this chapter and the snapshots of the simulations are skeched in Fig. 6.1 and the further simulation details are explained in Appendix. A.3. As references, the same systems without surface charge are also studied. Due to the crucial importance of the solute accumulation at the interface (IFs) for the practical applications explained in Chapter. 1, the influence of the surface charge on the molecular structure of the IL mixtures in front of surface is studied. In the previous chapter 5, the influence of the physical existence of the surface on the the accumulation of solutes is studied using the translational order parameter and corresponding entropic effect, and also hydrophobicity and the size/shape of the ions. Focus here is given again on the influence of different water/DMSO concentrations on the microstructuring and accumulation of each species at the interfaces (IFs). Especially, the entropic contributions in the observed trends are directly obtained from the simulations using a lattice-gas theory. The results highlight the distinct differences in these properties of the water and DMSO mixtures and unravel the underlying mechanisms. The importance of the size and polarity of the molecules in guiding their microstructuring in front of the surfaces, as well as their interactions with the latter, namely the solute-surface interactions are pointed out. The analysis on the molecular accumulation at the interfaces, allows us to predict whether the accumulation is entropy or enthalpy driven, which has an impact in controlling the accumulation of molec-

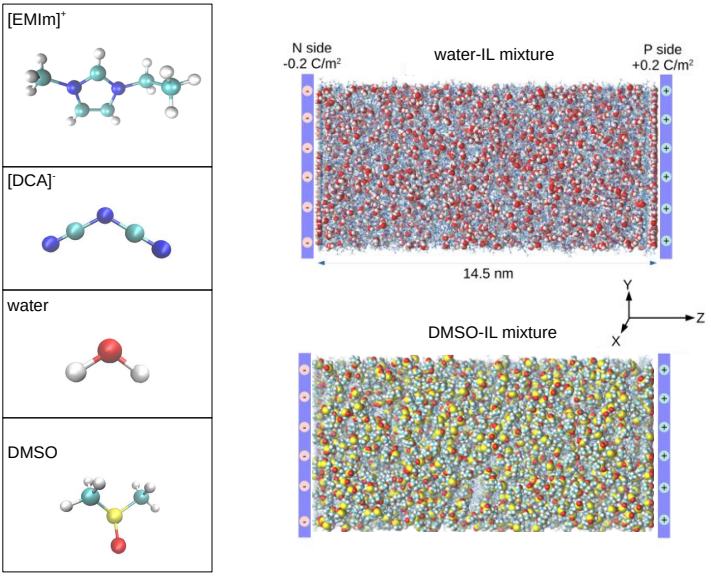

Figure 6.1: Left: ball & stick models of the IL ($[EMIm]^+$ cations and $[DCA]^-$ anions), as well as the water and DMSO. Right: a snapshot of an equilibrated IL-mixture with water (top) and DMSO (bottom) between two charged surfaces at a solute concentration of $x_{sol} = 0.500$. The axes, the charge on the IFs, and the distance between the IFs are depicted. 'N side' and 'P side' denote the negatively and positively charged IF, respectively. The hydrogen, oxygen, nitrogen, carbon, sulfur atoms are shown in white, red, blue, gray, and yellow, respectively.

ular species near the surfaces. Through the analysis, macroscopic properties, such as the electrochemical potential drop across the interfacial area and the conditions for obtaining a stable electrochemical window is discussed. The study in this chapter provides an essential understanding towards a careful design of electrochemical devices, namely the choice of the solutes and the concentration of them for specific applications.

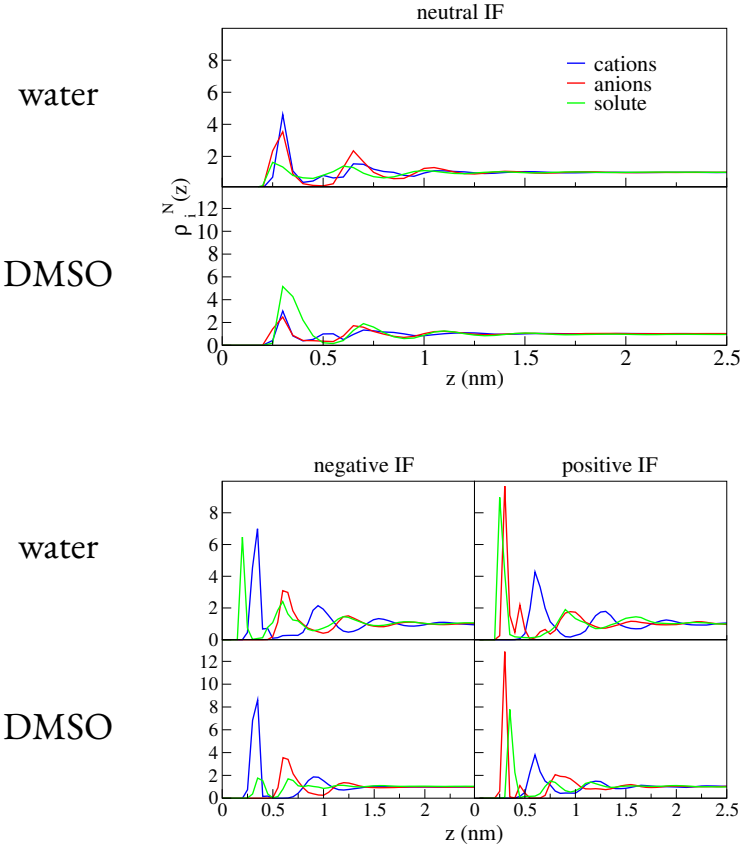

Figure 6.2: The normalized molecular density $\rho_i^N(z)$ of each species at a solute concentration of $x_{\text{sol}} = 0.5$ for water and DMSO mixtures with respect to the distance from the IF. The results are shown for neutral (top) and charged (bottom) surfaces as indicated by the labels. In the left panel due to the symmetric configuration for neutral surfaces only one is shown located at z=0 nm. The coloring of the lines corresponds to the species given in the legend.

6.2 Results

6.2.1 Density profiles at the interfaces

The analysis begins with the normalized molecular number density profiles of each species in the solution mixtures, as directly obtained from the MD simulations. The normalized molecular density is defined as $\rho_i^N(z) = \rho_i(z)/\rho_i^0$ with $\rho_i(z)$ the local number density at the position z (perpendicular to the IFs) and ρ_i^0 the bulk density of species i, respectively. The density is calculated with respect to the center of mass of each molecule and is given as a function of the distance z from the surfaces. According to this definition, $\rho_i^N(z)$ should converge to unity in the bulk near the center of the simulation box. Both in front of charged and neutral surfaces, distinct layers are formed, which agree with experimentally observed results[92]. A representative example of the layering structure in front of the neutral IFs at $x_{\text{sol}} = 0.5$ is shown in Fig.6.2(top) for both the water and DMSO mixtures. Inspection of these results reveals that in both cases three distinct layers are formed. The height of the peak for the solutes is about three times larger (≈ 6) for DMSO compared to water molecules (≈ 2). The ions show the opposite order, namely less ions accumulate in front of the surface in the DMSO mixtures compared to the water mixtures. The first peaks are located at $z_1 = 0.3$ nm for the cations and anions, at $z_1 = 0.25$ nm for water, and at $z_1 = 0.3$ nm for DMSO. Now, in order to evaluate the influence of the surface charge on the accumulation of the species close to the surfaces, the normalized density of each species in front

of both the negatively and positively charged surfaces are depicted on the bottom of Fig.6.2 again for a solute concentration of $x_{\mathrm{sol}} = 0.5$. The layering here differs from the case of the neutral IFs, as the position of the peaks shift to $z_1 = 0.3 \sim 0.35$ nm for the cations, 0.3 nm for anions, 0.2 nm for water, 0.4nm for DMSO close to the negative IF, and 0.3 nm for DMSO close to the positive IF. In the case of charged IFs, the relative heights of the first layer for all species show the opposite trend compared to the neutral IFs, namely in the water mixtures more ions and less solutes accumulate in front of the surfaces compared to the DMSO mixtures. These results show the formation of electric double layers (EDLs), which consist of the counter-ion-rich layer in front of the surface and the following co-ion-rich layer in front of both negatively and positively charged surfaces. The water molecules accumulate close to both IFs, while DMSO is depleted from the negative IF. The water molecules are much smaller than DMSO and can penetrate into the ion layers. The layers extend further towards the bulk, while more layers are formed in the water (up tp $z \approx 2$ nm) than in the DMSO mixtures (up to $z \approx 1.5$ nm).

In order to study the concentration dependency of the first layer in front of the surface, the normalized number density $\rho^N_{\mathrm{sol}}(z_1)$ of each species within the first layer at z_1 (z_1 for this calculation is explained above) close to each IF, with respect to the solute concentration x_{sol} are depicted in Fig.6.3. Interestingly, a clear difference is observed in the water and DMSO mixtures for both neutral (top) and charged IFs (bottom). Regarding the neutral surface, in the water mixtures, the number of ions increases in the first layer with an increas-

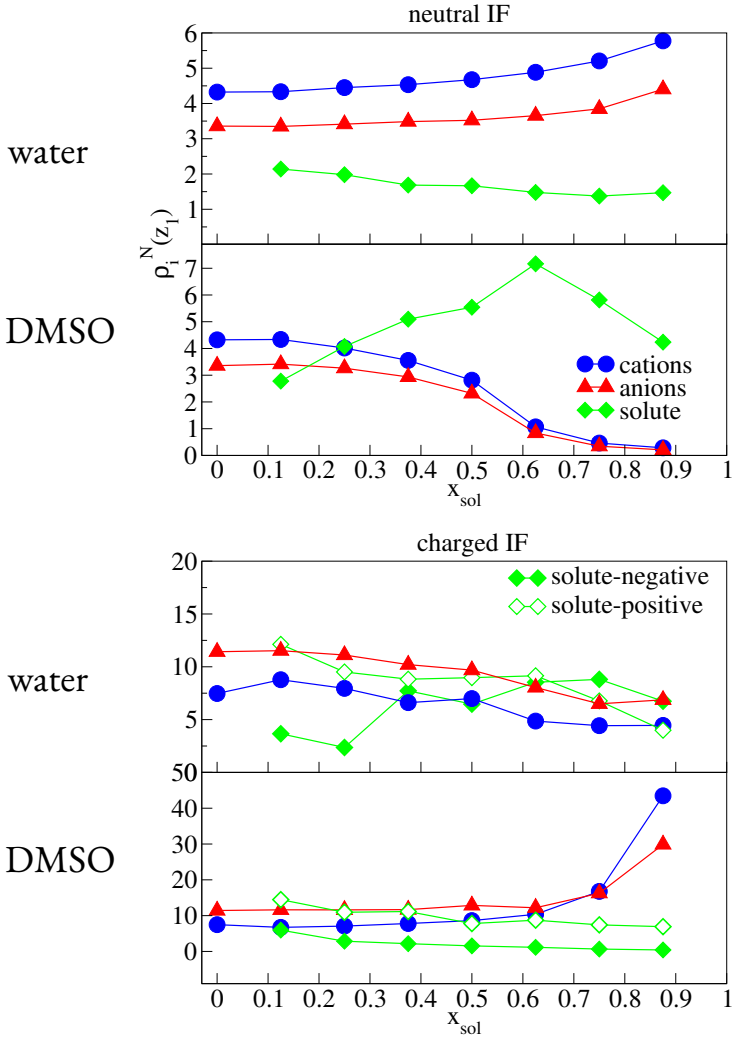

Figure 6.3: The normalized number density $\rho_{sol}^{N}(z_i)$ of each species within the first layer with respect to different solute concentration x_{sol} for water and DMSO mixtures with respect to the distance from the IF. The results are shown for neutral (top) and charged (bottom) surfaces as indicated by the labels. In the left panel due to the symmetric configuration for neutral surfaces only one is shown located at z=0 nm. The coloring of the lines corresponds to the species given in the legend.

ing concentration x_{sol}, while for the DMSO mixtures the number of ions, both cations or anions, within the first layer decreases. With increasing solute concentration, the number of water molecules within the first layer close to the IFs decreases with the concentration. In the DMSO mixtures, the number of DMSO species increase up to a concentration of $x_{sol} = 0.625$ and then drop. Accordingly, comparing water and DMSO mixtures underlines a reversed behavior in terms of the accumulation of each species within the first layer close to the neutral surface. This is a direct consequence of the different solute type, its size and polarity. These trends are inferred to be related with the discussion above on the molecular densities. In the case of the charged IFs shown on the bottom of this figure, the behavior of all molecular species closest to the surface is overall very different. Increasing the solute concentration x_{sol} leads to a decrease of the number of ions in front of the charged surfaces in the water mixtures and an increase in the DMSO mixtures, which is the opposite trend to the case of the neutral surface. Regarding the solute accumulation, in water this is enhanced at the negative side up to a concentration of $x_{sol} = 0.875$ and is depleted at the positive side. The DMSO accumulation is depleted both at the negative and positive IFs. This higher accumulation of the water molecules close to the negative IF is probably related with lower packing fraction of cations in front of the surface and the small size of water allowing them to penetrate into the cation layers. This distinct accumulation behavior is crucial for selected practical applications of IL-solute mixtures, depending on whether the accumulation of the specific molecular type is preferred or not

in front of the surface.

6.2.2 Entropy and molecular accumulation

In order to provide an insight into the fundamental mechanism of molecular accumulations at the IFs, the entropic contribution to the chemical potentials as provided in Eqns.(3.36), (3.37), (3.38) is calculated. For that, it is first necessary to estimate the term

$$\frac{n_i N_i}{N - n_+ N_+ - n_- N_- - n_s N_s} = \frac{\rho_i v_i / a_i}{1 - \rho_+ v_+ / a_+ - \rho_- v_- / a_- - \rho_s v_s / a_s}, \tag{6.1}$$

which can be found in Eqns.(3.34), (3.33), (3.35) for the chemical potentials, where N is the number of the total available sites, and N_i is the number of the species i, and n_i is the number of the sites occupied by a molecular species i, and ρ_i is the atomic number density of species $i = +, -, s$, for the cations, anions, and solute molecules, respectively. The molecular volume, v_i, is $v_+ = 0.116$ nm^3 for the cations, $v_+ = 0.0553$ nm^3 for the anions, $v_s = 0.0196$ nm^3 for water, and $v_s = 0.0717$ nm^3 for DMSO as obtained using van der Waals volumes and radii from the literature[19]. The number of atoms in each species, a_i, is $a_+ = 19$ for the $[EMIM]^+$ cations, $a_- = 5$ for $[DCA]^-$ anions, $a_s = 10$ for DMSO, and $a_s = 3$ for water. Using Eqn.(6.1), the entropic terms $-k_B T \Delta S_i$ in Eqns.(3.36), (3.37), and (3.38) are calculated in Fig. 6.4 (top) for neutral surfaces at distances in the range $0.125 \sim 0.375$ nm from the surfaces. These distances include the first peaks of the normal-

ized molecular number densities discussed above. Specifically, in water mixtures increasing entropy terms correspond to the ions and a decreasing term to the water molecules. In DMSO mixtures, a increasing entropy term corresponds to the DMSO and decreasing to the ions. These trends in both types of mixtures follow those for the normalized molecular densities in Fig.6.2(top). These results indicate the fact that the change in the accumulation behavior of molecules is governed by changes in the entropy. Combined with the result from the previous chapter, which reveals the entropy driven accumulation of water molecules near neutral surfaces, the accumulation of the molecular species close to the IFs is entropy driven even in DMSO mixtures.

Regarding the charged surfaces, the same entropy calculation is summarized in Fig.6.4 (bottom). Similar trends as for the normalized density in the first layer in Fig. 6.3 (bottom) are observed in both water and DMSO mixtures except for water and the anions in front of the positive surface, as for these the entropy terms increase with the solute concentration while the corresponding normalized densities decrease. The species except for anions at the positive IF in water mixtures, show a distinct behavior, as their trends are in average reversed compared to the neutral IFs. Regarding the DMSO-IL mixtures, the trends at the same concentration of $x_{\mathrm{sol}} = 0.5$ as in Fig.6.2(right) show a stronger accumulation of the ions at the charged IFs, followed by the DMSO molecules at positive and negative IFs, respectively. This is the same trend observed in the corresponding entropy terms for DMSO mixtures.

Overall, the analysis of entropy reveals the distinct difference in the en-

tropy contribution in the water accumulation in front of charged IFs as compared to DMSO mixtures. These results point to the fact that the accumulation of the species are entropy driven, except for the case of the water and the anion in front of the positive IFs. In these two exceptional cases, the accumulation is enthalpy driven. As discussed in Chapter 4, adding aprotic solute like DMSO does not change the molecular structuring at IFs, while a protic solute like water considerably changes this structuring by interacting strongly with the anions. The finding here unravels the underlying mechanism of the accumulation of molecular species at interfaces, allowing a proper selection of the species type in order to tune their interaction with surrounding molecules, thus their accumulations at the IFs. Through this choice, IFs and complex materials for desired applications can be designed.

6.2.3 Dipole moments of solutes and their interactions with IFs

The investigation up to this point, clearly discuss the entropic or enthalpic contributions for the accumulations of molecules at IFs. In order to obtain a deeper insight into the distinct features that the specific choice of molecular species can offer, the solute-surface interactions $\vec{d} \cdot \vec{E}^{IF}$ in Eqn.(3.38) are studied and the corresponding results are summarized in Fig.6.5. Here, the focus is given on the solute-surface electrostatic interactions, since the influence of the physical existence was already studied in the previous chapter. At a first glance, the solute-surface interactions are more or less of the same order

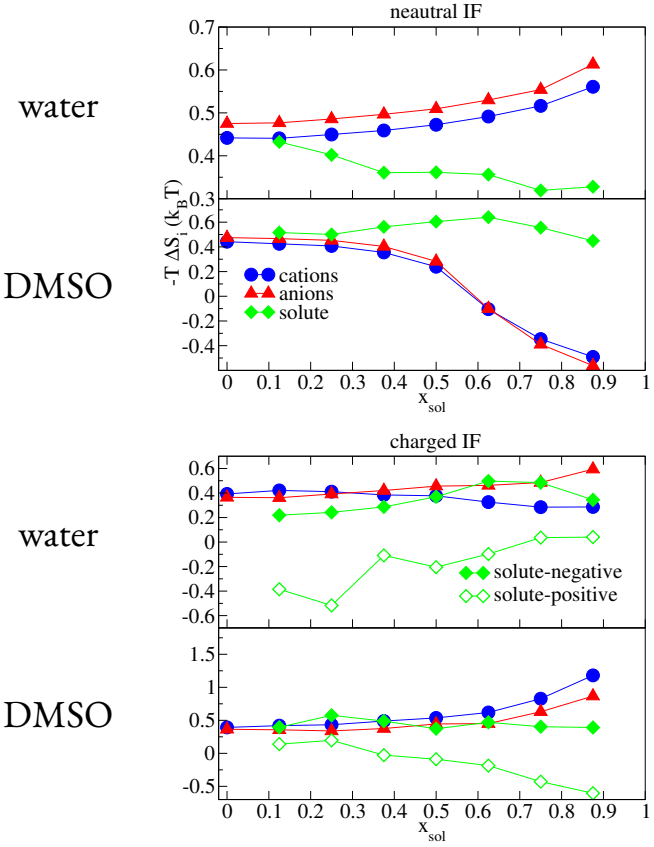

Figure 6.4: The entropy term at the first layer with respect to the solute concentration for (top) the neutral and (bottom) the charged IFs ((top) the water and (bottom) the DMSO mixtures for each panel), respectively. The symbols and coloring for the species follows the legend. For the charged IFs (bottom), filled and open symbols refer to the solute interactions with the negative and positive IF, respectively.

for all cases other than the water interaction with the negative IF. In the latter the solute-surface interactions are 2-4 times as strong as other cases. This feature, again, reflects the higher dielectric constant of water ($\varepsilon_r = 77.85$ at 299.15K[157]) compared to DMSO molecules ($\varepsilon_r = 46.39$ at 299.15K[157]) together with the weak interaction between cations accumulating at the negative IF and water[105]. As observed above, in the case of water mixtures Fig.6.2, the water molecules are closest to the negative IF, followed by the cations. Accordingly, water molecules can strongly interact only with the external field, namely the electrostatic field generated by the surface charge, since there is only weak interaction between water and cations. At the positive IF, though the water molecules are again closest to the surface, these are also more closer to the anions. As a result, the water molecules do not only interact with the IF, but also with the neighboring anion layer forming the hydrogen bonds with them. In the case of DMSO mixtures, the solute-surface interactions at the negative IF are less strong than the water mixtures due to the lower dielectric constant of DMSO and higher interaction with surrounding cations. DMSO, thus does not prefer to reorient in order to maximize its interactions with the charged surfaces. At the positive IF, the solute-surface interactions are about two times stronger, as the surrounding anions weakly interact with DMSO and the DMSO can reorient to interact wit the surface. These observations agree with the analysis discussed in Chapter. 4.

In order to analyze further the solute-surface interaction, the average normalized dipole moment of solutes are calculated. Due to the symmetric con-

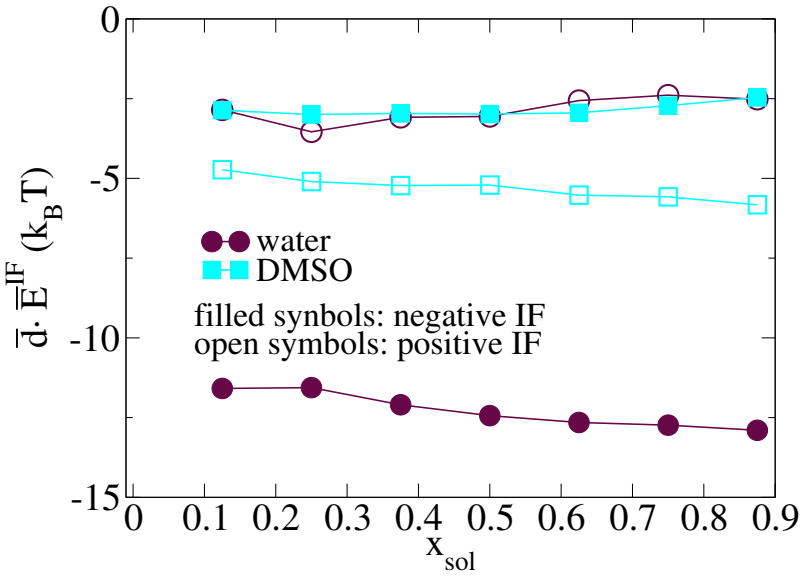

Figure 6.5: The solute-surface interactions for the charged IFs and the IL mixtures at different solute concentrations. The symbols for the solutes correspond to the legend. Filled and open symbols refer to the solute interactions with the negative and positive IF, respectively.

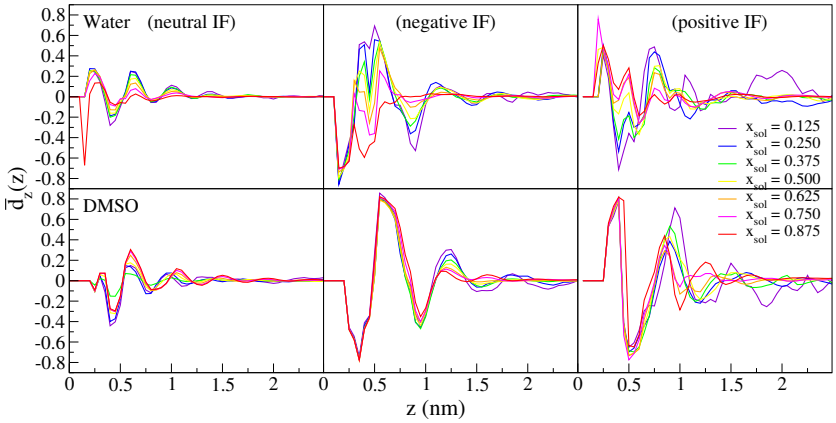

Figure 6.6: The z component of the average dipole moment $\overline{d_z(z)}$ of solutes in front of (left) neutral, (middle) negatively and (right) positively charged surfaces at different solute concentrations x_{sol} (see coloring in legend). The results are presented with respect to the distance z from the IF for (top) water and (bottom) DMSO mixtures. The color convention for the different $x$sol is denoted in the legend.

figuration along the x, y directions, the focus was given on the z component of the average dipole moment of the solutes with respect to their distance from the surface, which is given through:

$$\overline{d_z(z)} \quad = \quad \frac{1}{N}\sum_i \frac{\mu_{z,i}(z)}{|\vec{\mu}|}, \tag{6.2}$$

where $\mu_{z,i}$ is the z component of the dipole moment of the solute i, and $|\vec{\mu}|$ is the norm of the dipole moment of the solute, which is 2.35d for water and 4.416d for DMSO as calculated from the simulations. The sum is taken over N solute molecules located at the distance z from the surface.

The results shown in Fig. 6.6 reveal that, even in front of the neutral sur-

faces, the periodic orientational preference of solutes is observed. In water mixtures at neutral IFs, the first peak at $z = 0.2$ nm, corresponds to a positive average dipole moment for water up to a solute concentration of $x_{sol} = 0.750$. At this latter concentration, the first peak is shifted to $z = 0.15$ nm and corresponds to a negative value for the average dipole moment of water. This change indicates that the strong interaction of the hydrogen atoms of water with the anions is important up to high concentrations [105]. At these, the O-H bonds of the water molecules are directed towards the surface, namely free hydrogen atoms which do not form any hydrogen bonds are directed to the surface. At the highest water concentration $x_{sol} = 0.875$, most of the hydrogen atoms in water form hydrogen bonds either with anions or waters, which reflects the highly negative value of the z component of the water dipole moment at this concentration. In the case of DMSO mixtures at neutral surfaces, no modifications in the shape in DMSO occur, as DMSO interacts mostly through dispersion interactions with other molecules. These interactions are not highly influenced by changes in the solute concentration [105] as discussed in Chapter. 4.

In front of charged surfaces, the amplitude of the average normalized dipole moments is enhanced compared to the neutral surfaces due to the electrostatic interaction between solutes and the surfaces. As observed in Fig.6.2, the main differences between neutral surfaces and charged surfaces is the existence of the cation rich layer in front of the negatively charged surface and the anion rich layer in front of the positively charged surface. In water mixtures, in front of the negative IF, at a lower water concentration, the water dipole

moments point to the surface due to the strong electric field between the surface and the cation-rich layer at $z = 0.3$ nm. Furthermore, strong orientation of dipole moment opposite to the surface is observed between the cation-rich layer and the anion rich layer at $z = 0.6$ nm. At a high water concentration of $x_{\mathrm{sol}} = 0.875$, the dipole moments of water molecules are oriented towards the surface as water can penetrate through the ion layers and form clusters at the interface, forming a hydrogen bonded network. Within this network only weak interactions with the cations occur. This reflects the significant variations in the second peak ($z = 0.4 \sim 0.6$ nm) of the average normalized dipole moments when increasing the water concentration. Close to the positive IF, the water molecules interact with the anions at low water concentrations. At high water concentrations, water starts to form again clusters and hydrogen bonded networks with other water molecules. This observation is highly relevant to the interaction energy between the surface and the solute Φ_s^{IF} and $\vec{d} \cdot \vec{E}^{IF}$ in Eqn.(3.38) and reveals that the term $\vec{d} \cdot \vec{E}^{IF}$ is important only in the case of charged surfaces. It strongly influences the structuring of the ions in front of the charged surfaces, enhancing the differences in the solute-surface interactions between the positively and negatively charged surfaces as observed in Fig.6.5. In contrast, the DMSO mixtures do not show any significant changes with increasing the DMSO concentration in front of both positive and negative surfaces. As discussed in Ref. 105 the structuring of the ions at the IF is not strongly affected by changes in the DMSO concentration. The difference between the negative and positive IF for the DMSO mixtures in Fig. 6.5 may

be attributed to the strength of the second peaks ($\sim$ 0.5 nm), which weaken the average surface-solute interactions, since the height of the second peak at the negative IF ($\sim$ 0.85) is higher than at the positive IF ($\sim$ 0.8).

6.2.4 Electrostatic potential

For electrochemical applications, the electrostatic potential across the two IFs near the electrodes is very important to determine the electrochemical window. In order to access this, the charge distributions near the IFs are calculated at different solute concentrations in Fig. 6.7.

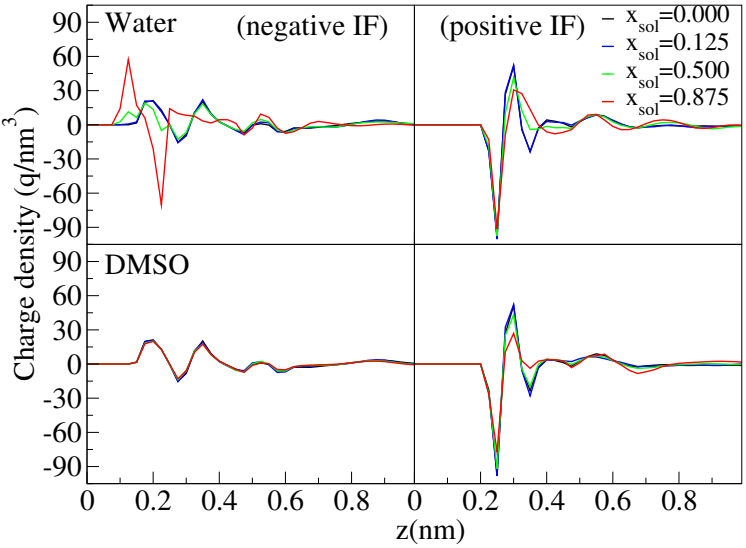

Figure 6.7: The charge distribution in water-$[EMIm]^+[DCA]^-$ (top) and DMSO-$[EMIm]^+[DCA]^-$ (bottom) mixtures near (left) the negatively charged surface and (right) the positively charged surface. The surface is located at $z = 0$ The solute concentrations are labelled according to the legends.

These results reveal the strong dependency on the solute concentration in the water mixtures at the negatively charged surface due to the accumulation of hydrogen atoms at the surface. At the positively charged IF, the influence of the solute concentration is more evident at the second layer and not at the first layer next to the surface. In the DMSO mixtures and the negative IF, due to the aprotic nature of DMSO, no influence of the solute concentration is observed. A small effect can, though, be observed mainly at the second layer close to the positive IF. With increasing solute concentration the counter-charge drops from about ± 50 q/nm^3 below $x_{\mathrm{sol}} = 0.5$ to half this value for the high concentration.

From the charge distributions in the mixtures, it is possible to calculate the electrostatic potential along the z direction $\Phi(z)$ in Eqns.(3.36) and (3.37) through

$$\Phi(z) = \int_0^z \int_0^z \frac{q}{\varepsilon_0} dz^2, \tag{6.3}$$

where q is the charge, ε_0 the dielectric constant and the integration is performed on surfaces across the distance connecting the two IFs. The respective results for both the water and DMSO mixtures are depicted in Fig.6.8. Note, that the reference potential is set at $z = 0$ near the negatively charged surface in each mixture. In the water mixtures, at the negatively charged surface, the lower the water concentration, the lower the potential. As the number of water molecules increases, the potential increases faster and reveals an abrupt peak

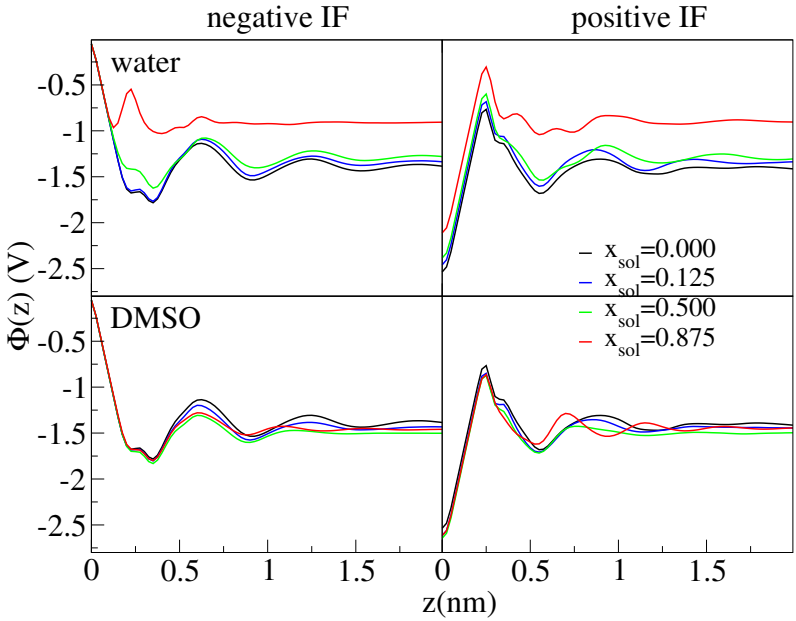

Figure 6.8: The electrostatic potential (from Eq.(6.3)) for the charged IFs, each positioned at z=0 nm. The results are shown for the water (top) and DMSO (bottom) mixtures, respectively as a function of the distances from the IFs and for a varying solute concentration range as labelled in the legend.

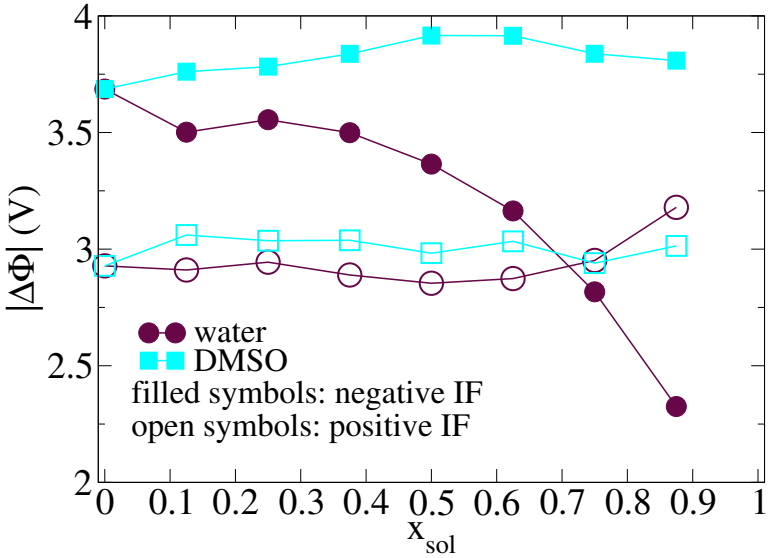

Figure 6.9: The electrostatic potential differences calculated by Eqn. 6.4 for (brown) for the water mixtures and (cyan) the DMSO mixtures.Filled and open symbols refer to the solute interactions with the negative and positive IF, respectively.

close to the surface. This peak can also be observed close to the negative IF, though there the trends are similar compared to lower solute concentrations. In the DMSO mixtures, only small variations in the electrostatic potential are observed with respect to the DMSO concentration. This holds for both IFs. The potential has a positive value at the negative IF, which drops to around $-1.5\ V$ towards the bulk, shows a peak around the first layer close to the IF, and decreasing to a negative value at the positive IF. These results, as also for the water mixtures, reveal an asymmetry between the two IFs, as the electrostatic potential does not have the same absolute value in both IFs.

In order to further elaborate on these trends, we focus on the absolute potential drop, $|\Delta\Phi|$, between the bulk and the surface at both IFs:

$$|\Delta\Phi| = |\Phi(z_{\mathrm{IF}}) - \Phi(z_{\mathrm{bulk}})|, \tag{6.4}$$

where $\Phi(z_{\mathrm{IF}})$ and $\Phi(z_{\mathrm{bulk}})$ are the electrostatic potentials at the IF and in the bulk respectively. For the latter, we refer to the part of the mixture, which is close to the midpoint between the IFs and has more bulk like properties corresponding the plateau in Fig. 6.8. The respective bulk position is set at $z_{\mathrm{bulk}} = 7.25$ nm. The results for both water and IL mixtures are shown in Fig.6.9. At first, it is obvious, that more distinct trends can be observed in the water mixtures at the negative IF. Calculating the potential drop from the positive IF towards the bulk shows a more or less steady behavior with a value just below 3 V apart from the higher solute concentration, for which this value in-

creases another $\sim$ 0.3 V. Taking as reference the negative surface, shows a large drop from about 3.7 V in the neat IL solution down to 2.3 V. In the DMSO mixtures, the potential drop from the negative and positive surfaces is close to 3.75 V and 3 V, respectively throughout the solute concentration range. Accordingly, a higher stability can be observed in the DMSO mixtures compared to the water mixtures. The underlying reason can be again due to the interaction of these solute molecules with surrounding molecules. The weak interaction of water with cations compared to DMSO becomes more evident as the solute concentration increases leading to a relatively strong reaction to the external field, leading to the high drop in the potential especially close to the negative IF. As already discussed above, the water molecules interact more strongly with the surface charge influencing the potential drop. In the end, the higher the water concentration, the larger the difference in the potential also compared to the neutral IFs, where no potential drop at the IF is expected.

6.3 Summary and Conclusions

Confined water-$[EMIm]^+[DCA]^-$ and DMSO-$[EMIm]^+[DCA]^-$ mixtures by two neutral or oppositely charged structureless walls with a surface charge of $0.2 C/m^2$ are studied. The influence of different water/DMSO concentrations on the microstructuring, accumulation and thermodynamics of each species is assessed. For the latter, the contribution of the entropy directly from the simulation results using a lattice-gas theory is evaluated. The results show a distinct

differences in these properties between water and DMSO mixtures. The results strongly indicate that the microstructuring of the molecular species in front of both neutral and charged surfaces are mainly governed by entropy changes throughout the solute concentration range. An exception from this trend was clear for water and the anions in front of the positively charged surface, where the strong interaction between anions and water play an important role suppressing the interaction of water with the positive surface. The observed potential drop was analyzed in detail with respect to the mixture type and concentration and the charged state of the surface. These potential drops is connected to the explicit solute-surface interactions in the confined IL mixtures. The investigation of these, revealing the significant role of the interaction between the surface charge and the dipole-moment of solutes, points to the observations that water reacts to the surface charge of the negatively charged surface, while DMSO reacts less strongly to the surface charge of the positively charged surface.

In view of practical applications, the different trends in the IL mixtures including water or DMSO, provide an essential understanding that allows a careful design of electrochemical devises. At first, the observation that in DMSO mixtures the accumulation of species at the charged IFs are still entropy driven suggests that DMSO, which has a larger molecular size than water, can be removed from the surface when the ILs are composed by large ions such as $[EMIM]^+$. On the other hand, removal of water from the surface is a challenging task due to the small size of the molecule. Water is a highly electronegative

molecule and, as indicated in Chapter. 4, interacts more strongly with the anions in front of positive IFs than with the positive IFs, which is a very important point for a stable electrochemical window in the confined solution. Overall, these results clearly show that the use of a large solute in combination with large ions can suppress the accumulation of solute molecules in front of charged surfaces. Through this choice, the interactions between surface charges and the solutes during the dilution of ILs can be avoided. Alternatively, solutes interacting strongly with ions can be chosen in order to reduce the interactions between surfaces and the solutes. This is an important aspect for the chemical stability of IL mixtures when adding solutes in order to increase their conductivity. In the end, the modelling and analysis discussed here provides valuable insight into the choice of the molecular type and size in tailoring the cation-anion combination in IL mixture. A proper choice can significantly assist and accelerate the design of IL mixtures with desired properties in view of specific purposes and applications.

7

Catalysts in Supported Ionic Liquid Phase (SILP) System

7.1 Motivation

Here, a more complex system with IL and solvent mixtures in confinement within mesoporous media is studied. The system of interest is the supported ionic liquid phase (SILP), where catalysts are immobilized into the ionic liq-

uid phase formed on top of functionalized silica surface in mesoporous media. Since this system consists of solute(catalyst), solvent(heptane), surface, surface charge, and ILs at the surface, the knowledge which is acquired through the study in previous chapters can be utilized. This template shows good reaction rates, improved selectivity, improved catalyst stability. Despite these advantages, knowledge about their underlying reason on a microscopic scale is missing. To this end, the purpose is set to assist in reaching an optimal configuration of such a system by MD simulations. For this purpose, the microscopic views of the following should be elucidated:

1. the immobilization of catalysts within the IL phase
2. the interaction of catalysts with other species
3. the dynamics of the molecules within a pore
4. the influence of the pore size
5. the influence of the IL concentration

In this thesis, the items 1, 2, and 3 are discussed. To this end, the focus is given on a biphasic solvent of heptane and $[BMIM]^+[OTF]^-$ within a nanopore in which catalysts are placed. Substrates (or reactants) are initially placed within the heptane solution. The system set-up is depicted in FIG.7.1. The study starts with a force field development for the Ru-based catalyst using density functional theory (DFT) calculations. Then, its solvation behavior within a bulk two-phase system of heptane and an IL is studied. Moreover, in order to

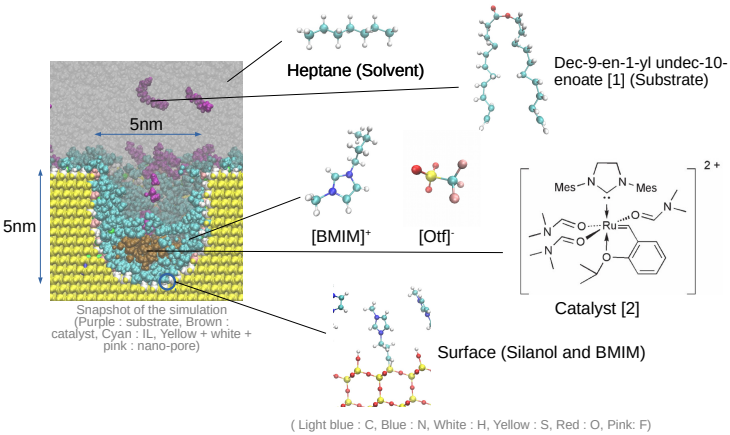

Figure 7.1: The setup of the supported ionic liquid phase (SILP).The color conventions are written in light grey color.

analyze the confinement effect, the static and dynamic properties of the confined system are investigated. The simulation details are summarized in Appendix. A.4.

7.2 Results

7.2.1 Modeling the system

Force-field for the Ru-catalyst

The OPLS/AA force field used for the IL, the heptane, and the substrates does not include a parameterization for the Ru-catalyst. Therefore, the respective parameters for the Ru-catalyst have to be developed based on quantum-mechanical/*ab initio* calculations within the density functional theory as im-

plemented in the ORCA quantum chemistry code [139]. Specifically, the parameters for the Ru-catalyst are generated using the B3LYP [94] exchange-correlation functional with the D3BJ dispersion correction [75] and the def2-TZVP basis set [219]. For the self consistent field (SCF) calculation the Pulay method [155] is utilized. The partial charges on the atoms are calculated through the CHELPG program [23,197]. Under these methods, the geometry of the catalyst is relaxed and the equilibrium structural properties is used for the force-field parameterization. All the partial charges on each atom are in the end multiplied by the rescaling factor of 0.8 to match the reduced charge force field for ILs. A semi-rigid model in which all bonds are constrained by the same harmonic potential, is employed. The same values of Lennard-Jones parameters as Ref. [236] are assigned to each atoms due to the similarity of the catalyst molecules used in these research. The optimized structure with the labels of each atom in the Ru-catalyst, as well as exact parameters of bond length, angles, partial charges are given in Appendix. A.4.

Bulk solutions

The purpose of the bulk phase simulations is to observe that the catalyst is dissolved into the IL phase and that heptane and the IL form a stable two-phase system with the catalyst residing in the IL phase. The detail of system compositions are summarized in Table. A.6. All the molecules, namely the catalytic molecules, the IL ions, and heptane, are randomly inserted into the 3D-periodic box. Snapshots of the simulations for the two types of bulk solutions

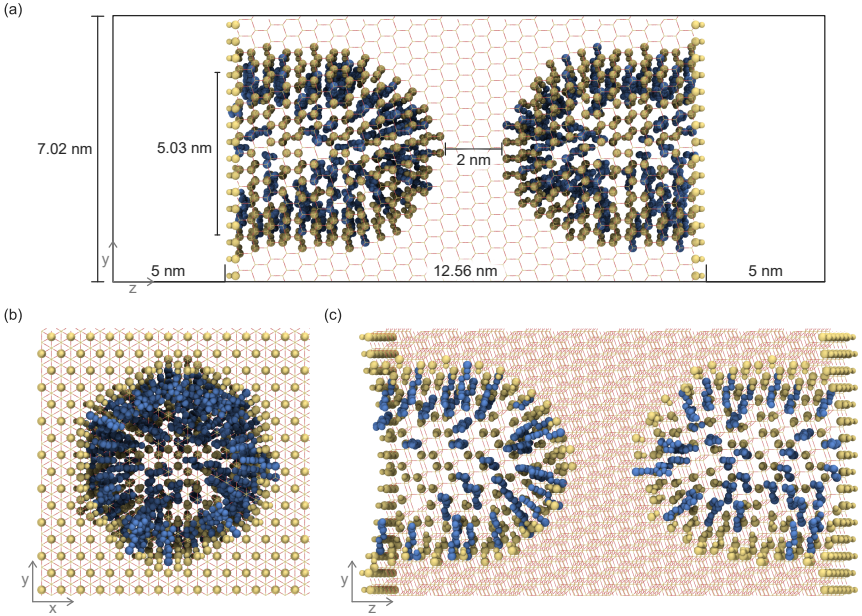

Figure 7.2: Pore model with two cavities generated with PoreMS [109,108]. (a) Side view of the simulation box indicating the length of the central silica block, the pore diameter, the cavity separation distance, and the solvent reservoirs. (b) Front and (c) side view of the carved silica block. The chemistry of the outer surface is based on the (111) face of β-cristobalite silica. The exterior planar and the interior curved surface are covered with Im-groups, which are randomly distributed on the silica surface. Further structural details are specified in Table A.7. Color code: Si, yellow lines; O, red lines; Im-groups, blue; silanol groups, yellow. Copyright 2021 Wiley. Used with permission from Ref. 103.

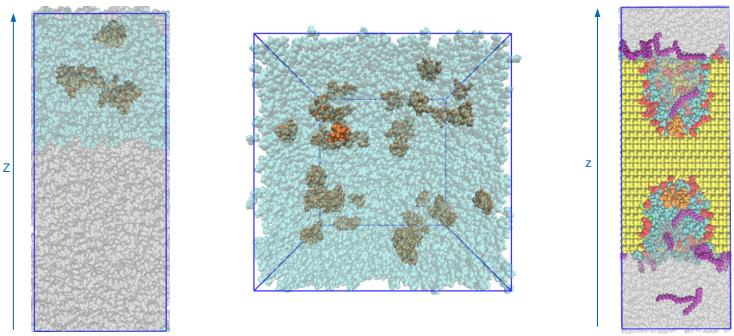

Figure 7.3: Snapshots of the simulations of the bulk solutions. (a) The two phase IL/heptane bulk system with the catalysts in the IL phase. (b) The bulk IL solution including the catalysts. (c) The confined setup of the pore with the solution, the catalysts, and the substrates. The IL, heptane, catalysts, substrates, pore, and chloride ions are colored in cyan, silver, orange, purple, yellow, and green, respectively. (Note, that due to the presence of the IL solution, the orange color of the catalysts in (a) and (b) is altered a bit.) Copyright 2021 Wiley. Used with permission from Ref. 103.

are depicted in (a) and (b) in Fig.7.3.

Confined catalyst within a nanopore

The geometry of the nanopore is created using the PoreMS Python package [109] Version 0.2.0 [108]. The nanopore consists of two capsule-shaped cavities at a distance of 2 nm carved out of a β-cristobalite block. The cavities are constructed by combining a cylinder with half a sphere of the same diameter of 5 nm. Two bulk reservoirs are attached on each of the exterior surfaces, representing the (111) face of β-cristobalite. The interior pore surfaces have been functionalized with $[BMIm]^+$ molecules with a coverage of 1.66 $\mu molm^{-2}$ and a residual hydroxilation of 7.75 $\mu molm^{-2}$. The exterior surface is left unchanged with a hydroxilation degree of 8.79 $\mu molm^{-2}$. The constructed pore system is depicted in Fig. 7.2 , while the structural details of this system are listed in Table A.7.

7.2.2 Catalysts in the bulk solutions

First, in order to study the fundamental properties of the IL-heptane mixtures, the results related to the catalysts in the two-phase IL/heptane solution (Fig. 7.3(a)) and then the catalysts in the bulk IL solution (Fig. 7.3(b)) are studied. For the former, the purpose is to observe that the heptane and the IL remain in two separated phases and do not mix. The catalyst remains throughout the simulation time within the IL part of the two-phase solution. In order

to quantify these results, the mass densities are calculated for all the species, heptane, IL cation, IL anion, catalyst in the two-phase bulk solution. For the calculation of the mass density, the simulation box is divided into slices and the average density of each slice is calculated. The results are depicted in Fig.7.4(a) and are shown along the z-axis, which is perpendicular to the interface between the IL and the heptane phase. It can be clearly observed that the heptane and IL do not mix and form two phases. Some small fluctuations in the mass density can only be observed at the interface (at $z \approx 7.5$ nm) due to the fluctuation of molecules at this area. Furthermore, the peak in the mass density of the catalysts lies well within the IL solution. Accordingly, it can be inferred that the catalysts are dissolved within the IL and not within the heptane phase. This is expected as the catalysts are divalent cations and strongly interact through electrostatic interactions with the ionic species of the IL showing an attraction towards the anions of the IL solution. Moreover, in order to confirm this observation theoretically, the free energies of the catalyst and substrate with respect to the position in the two phase heptane and ILs are calculated using umbrella sampling[203] with the weighted histogram analysis method[112] in Fig. 7.5 (a) and (b). Note that, due to the slow dynamics of the IL species and the catalysts, umbrella sampling is used to enhance the sampling along the reaction coordinates. In umbrella sampling, the molecules are restrained by harmonic potentials (bias potentials) at each reaction coordinate so that enough sampling is obtained by independent simulations at different reaction coordinates. After these independent simulations, the free energy along this reaction coordinate

can be calculated from the combined statistics of these simulations using the weighted histogram analysis method. Thereafter, in order to obtain the true free energy, the applied bias potentials are subtracted from the calculated free energy in the end. These results highlight again that the substrate has lower free energy in the heptane phase, while the catalyst has lower free energy in the IL phase. Therefore, it can be concluded that the substrates stay in the heptane phase and the catalysts stay in the IL phase. Furthermore, a close look at the profile reveals that the heptane and the catalysts have the minimum free energy at the interface between heptane and ILs. Especially when the surface is placed (Fig. 7.5 (c)), catalysts remain at the interface due to the electrostatic repulsion between the catalysts and the surface, which is positively charged due to the cationic surface functional groups. Therefore, it can be concluded that the catalytic reaction may occur at the heptane/IL interface whenever the two phase heptane-IL is formed.

In order to investigate the diffusion properties of all species in the bulk solutions, the time evolution of the mean squared displacement (MSD) of all species is calculated, since this quantity provides a very good estimation of the mobility of each species as discussed in Chapter. 3. The MSDs for the two phase bulk system are depicted in Fig.7.4(b). Inspection of this figure clearly shows that the heptane molecules diffuse much faster than the other ionic species (IL cations, IL anions, catalysts), which is important for delivering the substrates fast. This is physically intuitive due to the fact that there is less electrostatic interaction between the neutral species such as the heptane molecules

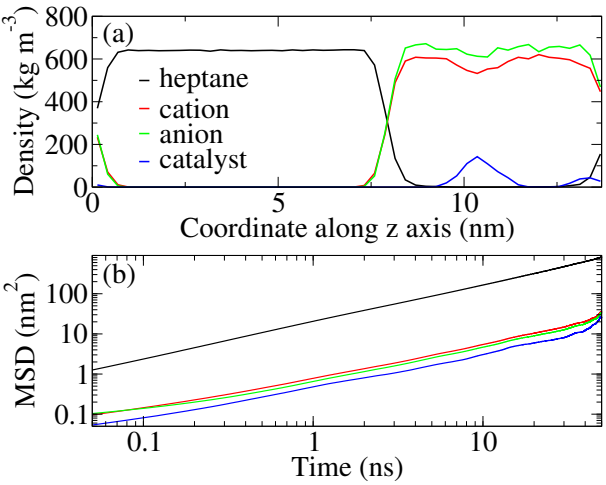

Figure 7.4: Results for the two phase bulk system with the catalysts in the IL phase. (a) The mass density profile of each species in the system along the z axis, which is perpendicular to the interface between two phases in the two phase system in bulk. (b) The mean square displacements (MSD) of each species. The species types and their combinations are labelled according to the legend. Copyright 2021 Wiley. Used with permission from Ref. 103.

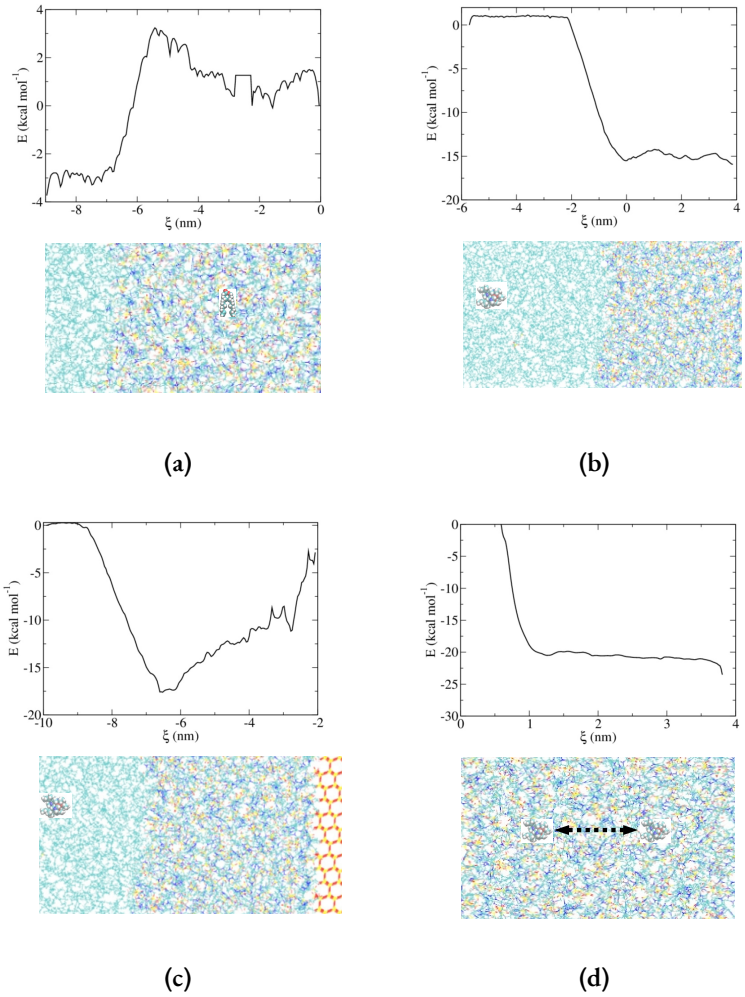

Figure 7.5: The free energy calculations for (a) the substrate in two phase heptane-ILs, (b) the catalyst in two phase heptane-ILs, (c) the catalyst in two phase heptane-ILs with a surface, and (d) the catalyst in bulk IL. The reaction coordinates ξ are expressed by the figures (cyan color: heptane, mixed color: IL, yellow & red: pore surface) under the each plots. For (a), (b), and (c), ξ is the position of the molecule in the figure. For (d) ξ is the distance between two catalysts (expressed by the arrow).

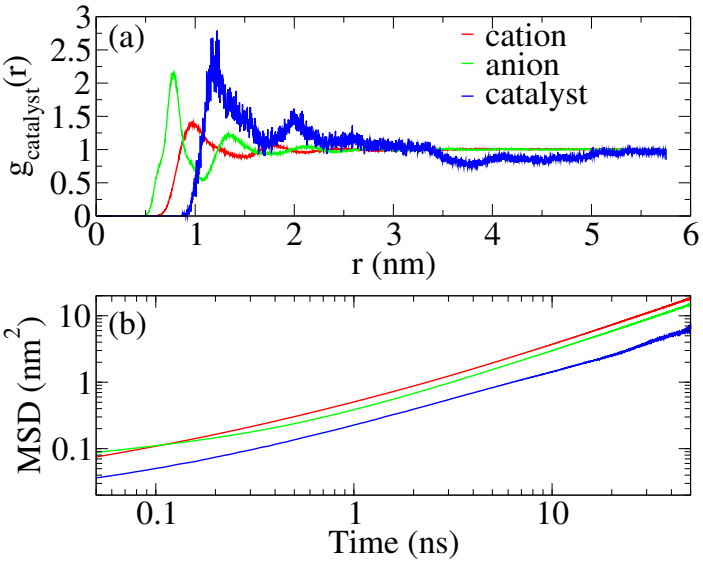

Figure 7.6: Results for the catalysts in the bulk IL solution. (a) The center of mass radial distribution (rdf) around the catalysts. (b) The mean square displacements (MSD) of each species. The species types and their combinations are labelled according to the legend. Copyright 2021 Wiley. Used with permission from Ref. 103.

and the substrates. The IL cations and IL anions show a very similar diffusion, with former moving a little faster within the IL phase. This observation is in agreement with previous studies, investigating the various factors that control diffusion in ionic liquids [206,205,34]. On the other hand, the Ru-catalysts diffuse slower than the IL species due to their stronger electrostatic interaction with the surrounding IL ions. Note that, not so smooth MSD curve for the catalysts arises from the small number of the catalytic molecules in the solution and the corresponding poor statistics in gathering the respective data, as compared to the other species (refer to Table. A.6).

In order to study the solvation of the catalysts within the IL phase and address issues of clustering and aggregation, the bulk IL simulations with the catalysts placed in bulk IL are performed. For this solution, the center of mass radial distribution functions (rdfs) is calculated between the catalyst and all the species (IL cation, IL anion, catalyst). As revealed from Fig.7.6(a), the anions form the first solvation shell around the catalyst due to the electrostatic interaction between oppositely charged molecular species in the solution. The cations which are positively charged follow in the second solvation shell. The catalysts accumulate around the second solvation shell, which is mostly occupied by the cations. These trends can be explained by the stronger electrostatic repulsion between the divalent catalysts and the weaker repulsion between the catalysts and the IL cations. In this way, the order of the peaks in the rdf for the reference catalyst follows the strength of interactions between the different species: the first peak corresponds to the anions (attraction to catalysts), the second peak to the cations (weaker repulsion to catalysts, but attraction to IL anions), and the third shell to the catalysts (stronger repulsion to catalysts, weaker repulsion to IL cations). This observation of the repulsion between catalysts are confirmed by the free energy calculation depicted in Fig. 7.5 (d), where the free energy with respect to the distance between two catalysts in a bulk IL solution is calculated. As this figure clearly shows, the free energy decrease with increasing distance between two catalyst molecules. Therefore, it is concluded that the catalysts do not aggregate within the IL phase, which is important for retaining the homogeneous catalytic reactions.

The MSD dynamics of the IL and the catalysts in Fig.7.6(b) show the trends as the two phase system in Fig.7.4(b). A small decrease in the MSD can be observed in the case of the IL species as compared to the two phase solution. The reason could be attributed to the fact that the IL species have smaller electrostatic interactions with the heptane molecules at the interface than with their own IL species in the bulk, thereby leading to a slightly higher diffusion in the two phase system close to the interface. The same decrease in the MSD and the diffusion can be seen also in the case of the catalysts for the same reason as the catalysts interact weakly with heptane at the heptane/IL interaface. Note that, due to the increased number of catalytic molecules, the statistics in gathering the data for the MSD is better for the case of the bulk simulation, thus the curve shows the expected linear behavior at longer times.

7.2.3 Confined catalysts within the nanopore

The main system of interest, namely the confined catalysts within nanopores (Fig. 7.3(c)) are studied. In this system, substrates are also randomly placed within the heptane solution. Note that, to neutralize the cationic surface functional groups, corresponding number of chloride atoms are placed in the system. The mass density profiles of all species along the axis perpendicular to the pore surface are calculated in a same manner as in the previous section. Initially, the pore is filled only with the ILs and the heptane phase covered only in the reservoir part. As the simulation runs, the heptane molecules enter the pore and move towards the bottom of the pore close to the catalyst as the black

curve in Fig.7.7(a) indicates. However, the heptane phase does not reach the bottom of the pore ($z = 10$ and 12 nm) where the ILs form a layer on the pore surface. Nevertheless, the partial filling of the pore with the heptane allows for the substrates to diffuse into the pore and reach the catalysts in order to eventually interact with the catalytic centers. The results show that the substrates accumulate further away from the catalyst on the pore. This can be explained by the fact that the surface area of the heptane-IL interface is larger outside of the pore compared to the inside of the pore. Therefore, the density of substrates at the pore exit shows the high density. Nevertheless, at many instances the substrates approach and interact with the catalytic centers, but overall they can be found at the heptane-IL interface as explained in terms of the free energy calculations. The IL species (cations and anions) accumulate at the inner surface of the pore, as these interact strongly with the positively charged functional groups on the pore surface. A close inspection of the cation and anion curves shows a larger accumulation of the cations closer to the positively functionalized surface, which at first seems counter intuitive. However, this process is similar as in the case of electrical double layers (EDL), where the counter-ion and co-ion rich layers are formed in front of charged surfaces as observed in the previous chapter. Even for a positive charge on the surface the bulkier (and fewer) cations accumulate closer to the surface with the help by the surrounding anions. The accumulation is especially evident at the bottom half of the pore. Note, that the density results are shown with respect to the axis perpendicular to the pore. Therefore, this perspective accumulates the 3D results on a

2D representation within the pore. Accordingly, the IL phase and the heptane do not coexist as falsely assumed by this representation, but still show a phase separation within the pore as can be visually observed in Fig. 7.3(c). Note that, compared to the bulk phase simulation, the pressure was slightly elevated in the pore phase simulation, thereby leading to the slightly higher density of heptane outside the pore. The chloride ions can also be found mainly close to the pore walls in order to play their role as counter-ions in that region. The catalysts (blue curve) remain in the IL phase within the pore during the whole simulation, which indicates that these molecules are well dissolved into IL phase inside of the pore and are immobilized by the IL solution accumulating on the pore surface.

Regarding the dynamics, the dynamics of the IL cations, IL anions, and catalysts in confinement are significantly slowed down compared to the bulk simulations discussed above. The MSDs for these species in Fig.7.7(b) clearly show a 10-fold decrease compared to the bulk simulations in Fig.7.6(b). This points to the role of confinement within the nanometer-sized pore for the linker-free immobilization of the catalyst. From all species in the solution, the catalysts show the slowest diffusion revealing the fact that these are more or less immobilized in the pore. This immobilization is made possible by the presence of the IL solution. (Note again that the poor statistics of the few catalysts in the solution leads to the low resolution of the MSD curve for large times). The chloride ions and the IL anions have a similar diffusion followed by a slightly larger diffusion of the IL cations. On the other hand, the heptane molecules

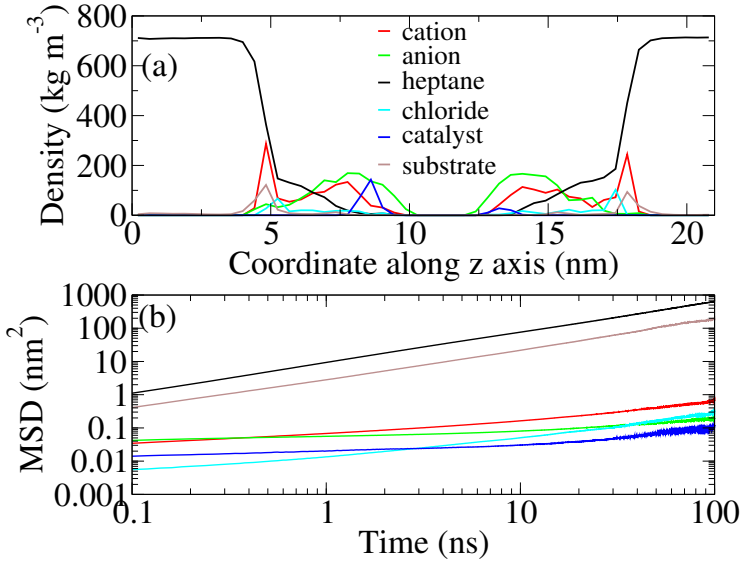

Figure 7.7: Results for the catalysts in confinement within the pore. (a) The mass density profile of each species in the system along the z axis perpendicular to the surface of the pore in the confined system with pores. (b) The mean squared displacement (MSD) of each species for the confined (solution, catalysts, substrates) system within the nanopore. The species types and their combinations are labelled according to the legends. Copyright 2021 Wiley. Used with permission from Ref. 103.

show a diffusion of the same order as in the two phase solution in Fig.7.4, which allows for the substrates with a diffusion of a similar order, flow into the pore. Accordingly, the substrates can diffuse through the heptane phase and reach the catalyst inside of the pore. This is very important for catalytic reactions to take place inside the pore. In short, the simulation results indicate that the heptane diffuses together with the substrates into the pore without mixing with the IL. The substrates can access the catalytic center, whose diffusion is strongly suppressed by the confinement and the presence of the IL ions. This is an expected mechanism of the catalytic reaction within the framework of the SILP technology. Note that, in this thesis, the focus is given on capturing the essential conditions before the catalytic reaction occurs in order to optimize the environment for the confined geometry. Therefore, the catalytic reaction is not simulated.

7.3 Summary and Conclusions

In this chapter, three different systems, namely two-phase bulk solution, a bulk IL solution, and a confined solution of heptane, IL, catalysts, and substrates within a nanometer sized pore, are studied. The purpose is to model a two-phase SILP system and understand the mechanism of dissolution of catalysts in the IL phase under confinement as well as the catalytic reaction between substrates and catalysts. The two phase simulation of heptane and IL shows a stable phase separation between heptane and IL, as well as the dissolution of

the catalysts in IL phase. This is an essential part for the success of the SILP technology, namely the immobilization of catalysts by the IL solution. Furthermore, according to the bulk IL simulations, the catalysts within the bulk IL solution do not show any aggregation, which is also essential for the reaction to take place homogeneously on the surface of the pore. Further analysis on the free energies reveals that the catalysts and the substrates meet each other at the heptane-IL interfaces, leading to the highly possible occurrence of the catalytic reactions there. With these two steps related to the bulk solutions, whether the conditions for the catalytic reaction in the IL solution can be reached, is estimated. To confirm this observation, the confined system with the pore filled with the heptane solution, the catalysts, and the substrates is studied. The mobility of the catalysts are significantly slowed down due to the electrostatic interaction between the catalysts, the IL species (cations and anions) and the functionalized pore surface. The respective results clearly show the dissolved and immobilized catalysts in the IL phase within the pore. The IL ions are slowed down significantly in the confined space due to the electrostatic interaction between the surface silanol group and the positively charged functional groups, which leads to the slow down of the catalysts due to the electrostatic interaction with the IL species. The heptane phase shows a considerably larger mobility and enters the pore together with the substrate molecules. The latter can thus reach the catalysts in the pore, thereby allowing for the catalytic reaction between the substrates and the catalysts can occur at the heptane-IL interface. In the end, the pore is filled with a two phase solution of IL and heptane,

with the catalysts remaining in the IL phase on the surface and the substrates mostly diffusing in the heptane phase, but occasionally moving closer to the catalysts which are expected to remain near the heptane-IL interface. The simulations thus provide the information about the local substrate concentrations within the pore, that are important for an overall analysis of the catalytic cycle.

In this chapter the important role of the electrostatic interactions between the surface of the pore and ILs, and also between the ILs and the catalysts for the dissolution of the catalysts into the IL phase, as well as their mobility, is confirmed. The purpose is again not to model the whole cycle of the catalytic reaction itself, but to study the conditions that are important for the catalysis eventually to take place. For this purpose the whole system before the reaction is set up, that pave the way for more in-depth investigation and analysis. These results will allow to selectively set the conditions in the solution and the pore in order to accelerate the catalytic process. These conditions may be the density of the surface groups, the pore size, and type of IL solution, the chemistry of the catalytic centers, the concentration of the ILs, etc. In fact, the results indicate the flexible material design as far as the two-phase heptane and IL on the surface is guaranteed. This may allow various pore sizes and pore geometries, since the catalytic reactions take place at the heptane-IL interface in any case.

8

Summary and Conclusions

In this thesis, the study started with the simple system of bulk IL-water/DMSO mixtures at different solute concentrations, where the preferential interactions between different species were studied using the framework of Kirkwood-Buff theory and the effective interaction energy. The results showed a fairly good agreement with experimental observations which highlights the validity of the

simulation methods used in this study. In the end, the analysis underlined that the strong influence of the protic solutes such as water on the ionic liquids compared to the aprotic solutes such as DMSO. Further analysis on the interfacial properties of IL-water/DMSO mixtures revealed the higher contribution from the entropic change to the accumulation of the molecules in front of flat surfaces, whether the surfaces are charged or not. These results point to the importance of the shape and the size of the molecules for the interfacial structures of the IL-solute mixtures, also to the surface-charge-dependent molecular accumulation in front of the surface. For the practical application, it was shown that the larger aprotic solutes can be used to avoid the accumulation of the solutes at the surface, which may hinder the potential of ILs as electrolytes. In the end, using the knowledge obtained through the study of the simple systems above, the study of the more complex and realistic system, namely catalysis in the supported ionic liquid phase, was carried out. The complex system was successfully modeled. Through the analysis on the dynamics and static properties, the main finding was the preferential occurrence of the catalytic reaction at the solvent/IL interface, which leads to the flexible design of the mesoporous material irrelevant to the size and the shape of the pores assuming the bi-phase of solvent/IL is formed on the pore surface. All the study conducted here can be used further to pave the way of the rational design of the IL mixtures for the selected practical applications, where the properties of the IL mixtures at the surface are highly relevant to the total performance and efficient use of materials, which will contribute to tackling the environmental issues such as CO_2

reduction or efficient energy conversion in the end.

A

Simulation Details

A.1 Ionic Liquids in Bulk

The details of the simulations performed in Chapter.4 are summarized here. All atomistic Molecular Dynamics (MD) simulations are performed for 1-ethyl-3-methylimidazolium dicyanamide $[EMIM]^+[DCA]^-$,

at various solute mole fractions ranging from $x_{sol} = 0$ (pure IL) to $x_{sol} = 0.875$ (highly diluted IL solution). Specifically, the mole fractions x_{sol} ={0, 0.125, 0.250, 0.375, 0.500, 0.625, 0.75, 0.875, 1.00} are considered for the bulk solutions. For the initial configurations, computational boxes of dimensions 6.3 nm - 6.5 nm in the periodic x, y, z-directions were used in which all species were randomly inserted using the software package PACKMOL [130]. The corresponding numbers of molecules and ions for the respective mole fractions are shown in Table A.1. Further details of MD parameters are summarized in Table. A.2.

Table A.1: The number of molecules and the box sizes for the MD simulations for (a) DMSO-$[EMIM]^+[DCA]^-$ and (b) water-$[EMIM]^+[DCA]^-$ mixtures. The box size is the length of the equilibrated system.

(a)

	Mole fraction of solute x_{sol}								
	0	0.125	0.250	0.375	0.500	0.625	0.750	0.875	1
Number of ions n_i	1000	1000	1000	1000	1000	750	550	320	0
Number of solute molecules n_{sol}	0	143	333	600	1000	1250	1650	2240	3000
Box length in x,y,z directions (nm)	6.41	6.55	6.71	6.93	7.24	6.99	6.96	7.02	7.07

(b)

	Mole fraction of solute x_{sol}								
	0	0.125	0.250	0.375	0.500	0.625	0.750	0.875	1
Number of ions n_i	1000	1000	1000	1000	1000	750	550	320	0
Number of solute molecules n_{sol}	0	143	333	600	1000	1250	1650	2240	3170
Box length in x,y,z directions (nm)	6.41	6.45	6.49	6.55	6.65	6.17	5.80	5.33	4.56

Table A.2: The MD parameters for the simulations performed in Chapter. 4.

Software package	:	GROMACS 5.1.3[208,154,2]			
Force field (OPLS/AA)					
$[EMIM]^+[DCA]^-$	:	From Ref. 33			
DMSO	:	From Ref. 30			
Water	:	SPC/E[95]			
Electrostatic interaction					
Type	:	particle mesh Ewald (PME)[45,54]			
PME order	:	4			
Fourier spacing	:	0.16 nm			
Cut-off radius	:	1.0 nm			
Van der Waals interaction					
Type	:	Cut-off			
Cut-off radius	:	1.0 nm			
Bonds					
Constraint	:	All-bonds			
Algorithm	:	LINCS[81]			
		Energy minimization	Equilibration (NVT)	Equilibration (NpT)	Production run (NpT)
Integrator	:	Conjugate gradient	Leapfrog	Leapfrog	Leapfrog
Time step	:	-	2 fs	2 fs	2 fs
Simulation time	:	-	10 ns	10 ns	300 ns
Temperature coupling					
Coupling method	:	-	Velocity-rescaling[28]	Velocity-rescaling	Velocity-rescaling
Coupling constant	:	-	0.1 ps	0.1 ps	0.1 ps
Reference temperature	:	-	300 K	300 K	300 K
Pressure coupling					
Coupling method	:	-	-	Berendsen[16]	Parrinello-Rahman[147]
Coupling constant	:	-	-	2 ps	2 ps
Reference pressure	:	-	-	1 bar	1 bar
Compressibility	:	-	-	4.5×10^{-5}bar^{-1}	4.5×10^{-5} bar^{-1}
Output control					
Energies	:	-	-	-	1 ps
Positions	:	-	-	-	10 ps
Velocities	:	-	-	-	10 ps

A.2 Ionic Liquids in Confinement between Neutral Surfaces

The details of the simulations performed in Chapter.5 are summarized here. All atomistic molecular dynamics (MD) simulations are performed for IL-water mixtures with different water weight fractions $x_{H_2O} = \{0.000, 0.125, 0.250. 0.375, 0.15, 0.500, 0.625, 0.750, 0.875, 0.95, 0.96, 0.97, 0.98, 0.99\}$ in distinct ILs $[EMIM]^+[DCA]^-$, $[EMIM]^+[BF_4]^-$ and $[BMIM]^+[BF_4]^-$. The IL-water mixtures are randomly inserted into rectangular simulation boxes of dimensions 6.3 nm – 6.5 nm in periodic x, y–direction and 14.5 nm in z–direction using the software package PACKMOL[130]. The z–direction was constrained by two impenetrable silicon walls with Lennard-Jones (LJ) 9-3 potentials. The semi-isotropic Parrinello-Rahman barostat[147] (periodic x– and the y–dimensions with fixed z–dimension) is used to fix the box length in z direction. In order to avoid unrealistic interactions behind the surfaces, a 3D-Ewald summation method with the correction term[227] was used assuming empty boxes with a height of three times the box length in the z-direction behind each surface. The MD parameters are summarized in Table. A.3. The numbers of the molecules in the simulation box are summarized in Table. A.4 (a).

Table A.3: The MD parameters for the simulations performed in Chapter. 5 and Chapter. 6.

Software package	:	GROMACS 5.1.3 [208,154,2]			
Force field (OPLS/AA)					
$[EMIM]^+[DCA]^-$	:	From Ref. 33			
$[EMIM]^+[BF_4]^-$	:	From Ref. 33			
$[BMIM]^+[BF_4]^-$	:	From Ref. 33			
DMSO	:	From Ref. 30			
Water	:	SPC/E [95]			
Electrostatic interaction					
Type	:	particle mesh Ewald (PME) [45,54]			
PME order	:	4			
Fourier spacing	:	0.16 nm			
Cut-off radius	:	1.0 nm			
Van der Waals interaction					
Type	:	Cut-off			
Cut-off radius	:	1.0 nm			
Bonds					
Constraint	:	All-bonds			
Algorithm	:	LINCS [81]			
		Energy minimization	Equilibration (NVT)	Equilibration (NpT)	Production run (NpT)
Integrator	:	Conjugate gradient	Leapfrog	Leapfrog	Leapfrog
Time step	:	-	2 fs	2 fs	2 fs
Simulation time	:	-	10 ns	10 ns	200 ns for neutral surfaces (500 ns for $x_{H_2O} = 0$) 300 ns for charged surfaces
Temperature coupling					
Coupling method	:	-	Velocity-rescaling [28]	Velocity-rescaling	Velocity-rescaling
Coupling constant	:	-	0.1 ps	0.1 ps	0.1 ps
Reference temperature	:	-	300 K	300 K	300 K
Pressure coupling (z direction)					
Coupling method	:	-	-	Berendsen [16]	Parrinello-Rahman [147]
Coupling constant	:	-	-	2 ps	2 ps
Reference pressure	:	-	-	1 bar	1 bar
Compressibility	:	-	-	4.5×10^{-5}bar^{-1}	4.5×10^{-5} bar^{-1}
Output control					
Energies	:	-	-	-	1 ps
Positions	:	-	-	-	10 ps
Velocities	:	-	-	-	10 ps

A.3 Ionic Liquids in Confinement between Charged Surfaces

The details of the simulations performed in Chapter.6 are summarized here. The simulation setups are as same as in Table. A.3 except for the simulation time for the production runs is extended from 200 ns to 300 ns. For the charged surfaces, the surface charge is implemented by image charges on the surfaces so that the absolute value of the charge density equals approximately 0.2 C/m^2. The left and right surfaces were negatively and positively charged, respectively

Table A.4: The number of molecules and the box sizes for the MD simulations of water-$[EMIM]^+[DCA]^-$ mixtures and DMSO-$[EMIM]^+[DCA]^-$ mixtures for different solute concentrations. 'NIF' and 'CIF' refer to the neutral and charged IFs, respectively.

Mixture	Mole fraction of solvent x_{sol}							
	0	0.125	0.250	0.375	0.500	0.625	0.750	0.875
water-$[EMIM]^+[DCA]^-$ **water-$[EMIM]^+[BF_4]^-$** **water-$[BMIM]^+[BF_4]^-$**								
Number of ions N_i	2500	2310	2257	2187	2090	1946	1710	1254
Number of solutes N_{sol}	0	330	752	1312	2090	3243	5130	8778
Box length in x/y directions (nm) (NIF)	6.82	6.61	6.61	6.60	6.58	6.56	6.53	6.46
Box length in x/y directions (nm) (CIF)	6.78	6.57	6.57	6.56	6.55	6.54	6.51	6.46
DMSO-$[EMIM]^+[DCA]^-$								
Number of ions N_i	2500	2310	2190	2000	1760	1422	1110	640
Number of solutes N_{sol}	0	330	730	1200	1760	2370	3330	4480
Box length in x/y directions (nm) (NIF)	6.82	6.76	6.83	6.86	6.87	6.77	6.93	6.99
Box length in x/y directions (nm) (CIF)	6.78	6.72	6.80	6.82	6.83	6.75	6.92	7.00

(see Fig.6.1). The corresponding numbers of molecules and ions for the respective mole fractions are shown in Table A.4.

A.4 Catalysts in Supported Ionic Liquid Phase (SILP) System

The details of simulations performed in Chapter.7 are summarized here.

A.4.1 Simulation Details

Atomistic Molecular Dynamics (MD) simulations are performed for different model systems. First, a two-phase system made of 1-Butyl-3-methylimidazolium trifluoromethanesulfonate $[BMIM]^+[Otf]^-$ and heptane is performed. Then a Ru-catalyst is placed within this two-phase bulk solution and its diffusion is monitored. At a next step, only a bulk IL solution with the Ru-catalyst is considered in order to investigate configurational aspects of the catalysts in the solution. Having gained an insight from the behavior in bulk, the Ru-catalysts, as well as substrates are placed within a nanometer-sized pore and follow the dynamics of the system. The surface of the pore are covered by silanol groups, resembling a fully hydroxylated surface[88]. The inner walls of the pore have been functionalized with imidazolium (Im) molecules, in order to tune the polarity of the pore and its interaction with the IL solution. In the solution within the pore, chloride ions were added to play the role of counterions and neutralize the surface functional groups inside of the pore. The corresponding structures of all molecules considered in this work are shown in Fig.4.1.

For the atomistic MD simulations the reduced charged model ($\times$ 0.8) for

the IL is employed. Therefore, the partial charges of other ionic species including the surface functional group, chloride atoms and the own developed Ru-catalyst also uniformly reduced by the factor of 0.8 [86,170]. This approach is commonly used to study bulk IL solutions. However, alternative approaches do exist (refer to [42,159]. In order to resemble typical experimental conditions [9], all simulations were conducted at $T = 353$ K. For the confined system, the simulation was extended for 100 ns under the (NVT) ensemble. The simulations of the bulk solutions, were performed under the (NPT) ensemble and the total time of the NPT simulation was 50 ns. The details of the simulation parameteres are summerized in Table. A.5. Furthermore, the exact details and geometries of the computational boxes are given in Table A.7 as well as in Fig. 7.2. For the random insertion of molecules, the software package PACKMOL [130] for the bulk simulations was used. The corresponding numbers of molecules and ions are shown in Table A.6 for each type of simulations.

A.4.2 Chemical Structure of the Ru-catalyst

Chemical structure of the Ru-catalyst is sketched in Fig. A.1.

Table A.5: The MD parameters for the simulations performed in Chapter. 7.

Software package	:	GROMACS 5.1.3 [208,154,2]			
Force field (OPLS/AA)					
$[BMIM]^+[OTF]^-$	:	From Ref. 170			
Surface functional group	:	From Ref. 170			
Heptane	:	From Ref. 95			
Substrate	:	From Ref. 95			
Electrostatic interaction					
Type	:	particle mesh Ewald (PME) [45,54]			
PME order	:	4			
Fourier spacing	:	0.16 nm			
Cut-off radius	:	1.0 nm			
Van der Waals interaction					
Type	:	Cut-off			
Cut-off radius	:	1.0 nm			
Bonds					
Constraint	:	Hydrogen-bonds			
Algorithm	:	LINCS [81]			
		Energy minimization	Equilibration (NVT)	Bulk (NpT)	Confined (NVT)
Integrator	:	Conjugate gradient	Leapfrog	Leapfrog	Leapfrog
Time step	:	-	2 fs	2 fs	2 fs
Simulation time	:	-	20 ns	50 ns	100 ns
Temperature coupling					
Coupling method	:	-	Velocity-rescaling [28]	Velocity-rescaling	Velocity-rescaling
Coupling constant	:	-	0.1 ps	0.1 ps	0.1 ps
Reference temperature	:	-	353 K	353 K	353 K
Pressure coupling					
Coupling method	:	-	-	Parrinello-Rahman [147]	-
Coupling constant	:	-	-	2 ps	-
Reference pressure	:	-	-	1 bar	-
Compressibility	:	-	-	4.5×10^{-5}bar^{-1}	-
Output control					
Energies	:	-	-	-	1 ps
Positions	:	-	-	-	10 ps
Velocities	:	-	-	-	10 ps

Table A.6: Number of the species in the simulation boxes for the different type of simulations. Copyright 2021 Wiley. Used with permission from Ref. 103.

	two phase in bulk	bulk IL	confined system with pores
$[BMIM]^+$	500	4000	200
$[Otf]^-$	510	4080	210
Heptane	1000	-	1885
Catalyst	5	40	5
Substrates	-	-	20
Cl^-	-	-	165

Table A.7: Properties of the generated cavity pore model. Copyright 2021 Wiley. Used with permission from Ref. 103.

	Interior	Exterior
Silica block *xyz*-dimensions (nm)	7.08; 7.02; 12.56	
Simulation box *xyz*-dimensions (nm)	7.08; 7.02; 22.55	
Pore drilling direction	z	
Pore diameter (nm)	5.03	
Surface roughness (nm)	0.08	0.00
Cavity separation distance (nm)	2.00	
Solvent reservoir *z*-dimension (nm)		5.00
Inner pore volume (nm^3)	2×86.86	
Solvent reservoir volume (nm^3)		2×248.49
Surface area (nm^2)	2×82.34	2×29.85
Surface chemistry before functionalization		
Number of single silanol groups	654	252
Number of geminal silanol groups	140	32
Number of siloxane bridges	0	0
Total number of OH groups	934	316
Overall hydroxylation ($\mu mol\ m^{-2}$)	9.42	8.79
Surface chemistry after functionalization		
Number Im groups	165	0
Im groups density ($\mu mol\ m^{-2}$)	1.66	0.00
Bonded-phase density ($\mu mol\ m^{-2}$)	1.66	0.00
Number of residual OH groups	769	316
Residual hydroxylation ($\mu mol\ m^{-2}$)	7.75	8.79

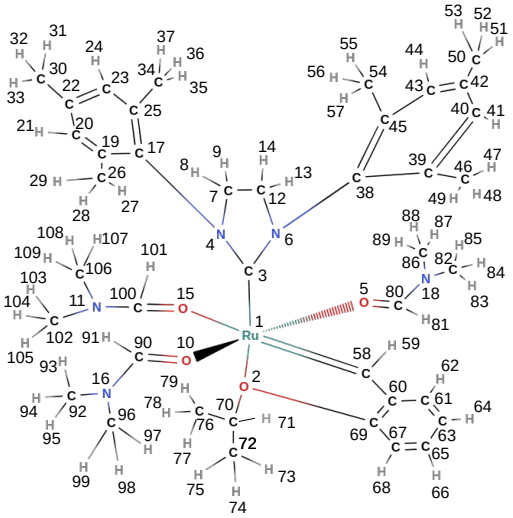

Figure A.1: The chemical structure of the Ru catalyst. The number on each atom corresponds to the atom labels described in Table A.8. The hydrogen, carbon, nitrogen, and ruthenium atoms are labelled as H, C, N, and Ru, respectively. Copyright 2021 Wiley. Used with permission from Ref. 103.

A.4.3 The force field parameters for the Ru-catalyst

Table A.8: The force-field parameters (partial charges, bonds-lengths and bond-angles) for the Ru-catalyst. The atom labels are depicted in Fig.A.1. The numbers in the bond and angle labels correspond to the atom labels of that figure. Copyright 2021 Wiley. Used with permission from Ref. 103

atom label	atom name	partial charge (e)	bond label	bond length (nm)	angle label	bond angle (°)
1	Ru1	0.7863296	1 - 2	0.2392	3 - 1 - 2	166.81
2	O1	-0.2447064	1 - 3	0.2005	5 - 1 - 2	83.97
3	C1	-0.3421256	1 - 5	0.2051	15 - 1 - 2	84.41
4	N1	0.3702056	1 - 15	0.2090	58 - 1 - 2	76.84
5	O2	-0.2785264	1 - 58	0.1856	10 - 1 - 2	97.77
6	N2	0.2548328	1 - 10	0.2300	1 - 2 - 69	108.03
7	C2	-0.1175416	3 - 4	0.1348	1 - 2 - 70	129.53
8	H1	0.0817368	3 - 6	0.1351	5 - 1 - 3	96.78
9	H2	0.0912664	4 - 17	0.1428	15 - 1 - 3	98.73
10	O3	-0.349272	4 - 7	0.1475	58 - 1 - 3	90.09
11	N3	0.2447184	7 - 8	0.1090	10 - 1 - 3	95.34
12	C3	-0.112416	7 - 9	0.1090	1 - 3 - 4	126.79
13	H3	0.092568	7 - 12	0.1525	1 - 3 - 6	125.34
14	H4	0.0912408	12 - 13	0.1091	15 - 1 - 5	158.17
15	O4	-0.1584904	12 - 14	0.1090	58 - 1 - 5	99.85
16	N4	0.1694488	6 - 12	0.1477	10 - 1 - 5	80.57
17	C4	-0.6333536	6 - 38	0.1432	1 - 5 - 80	127.11
18	N5	0.25618	38 - 39	0.1396	58 - 1 - 15	95.40
19	C5	0.5409208	38 - 45	0.1404	10 - 1 - 15	82.77
20	C6	-0.481388	39 - 46	0.1506	1 - 15 - 100	128.13

21	H5	0.1526712	39 - 40	0.1397	10 - 1 - 58	174.48
22	C7	0.4426312	46 - 47	0.1091	1 - 58 - 60	120.99
23	C8	-0.4683016	46 - 48	0.1093	1 - 58 - 59	125.14
24	H6	0.1560968	46 - 49	0.1088	1 - 10 - 90	128.64
25	C9	0.4555552	40 - 41	0.1084	6 - 3 - 4	107.54
26	C10	-0.5066496	40 - 42	0.1389	3 - 4 - 17	129.16
27	H7	0.1298112	42 - 50	0.1504	3 - 4 - 7	113.60
28	H8	0.1288472	50 - 51	0.1091	3 - 6 - 12	113.24
29	H9	0.1501136	50 - 52	0.1091	3 - 6 - 38	129.32
30	C11	-0.427176	50 - 53	0.1093	7 - 4 - 17	117.12
31	H10	0.1076528	42 - 43	0.1396	4 - 17 - 25	119.45
32	H11	0.13308	43 - 44	0.1084	4 - 17 - 19	118.80
33	H12	0.1204384	43 - 45	0.1389	4 - 7 - 8	109.94
34	C12	-0.3940928	45 - 54	0.1502	4 - 7 - 9	110.09
35	H13	0.1254768	54 - 55	0.1091	4 - 7 - 12	102.63
36	H14	0.071236	54 - 56	0.1089	9 - 7 - 8	108.06
37	H15	0.1084232	54 - 57	0.1092	12 - 7 - 8	112.82
38	C13	-0.6217128	17 - 25	0.1396	12 - 7 - 9	113.20
39	C14	0.5407528	17 - 19	0.1400	7 - 12 - 13	113.04
40	C15	-0.5471624	19 - 26	0.1504	7 - 12 - 14	113.13
41	H16	0.1767272	26 - 27	0.1093	7 - 12 - 6	102.87
42	C16	0.4754224	26 - 28	0.1089	14 - 12 - 13	107.88
43	C17	-0.5286416	26 - 29	0.1088	6 - 12 - 13	109.85
44	H17	0.1718472	19 - 20	0.1391	6 - 12 - 14	109.99
45	C18	0.537564	20 - 21	0.1084	38 - 6 - 12	115.65
46	C19	-0.425668	20 - 22	0.1395	6 - 38 - 39	120.23
47	H18	0.1299544	22 - 23	0.1391	6 - 38 - 45	118.15
48	H19	0.1074888	22 - 30	0.1503	45 - 38 - 39	121.18

49	H20	0.0968672	30 - 31	0.1094	38 - 39 - 46	122.96
50	C20	-0.3555192	30 - 32	0.1091	38 - 39 - 40	118.27
51	H21	0.0919568	30 - 33	0.1089	38 - 45 - 43	118.42
52	H22	0.0965112	23 - 24	0.1084	38 - 45 - 54	121.11
53	H23	0.1155288	23 - 25	0.1392	40 - 39 - 46	118.73
54	C21	-0.4324256	25 - 34	0.1503	39 - 46 - 47	110.26
55	H24	0.1167016	34 - 35	0.1093	39 - 46 - 48	111.21
56	H25	0.1132192	34 - 36	0.1090	39 - 46 - 49	112.33
57	H26	0.1116272	34 - 37	0.1090	39 - 40 - 41	118.65
58	C22	-0.2556728	10 - 90	0.1241	39 - 40 - 42	122.02
59	H27	0.0875152	90 - 91	0.1091	48 - 46 - 47	106.76
60	C23	0.0850016	90 - 16	0.1327	49 - 46 - 47	107.93
61	C24	-0.148792	16 - 92	0.1455	49 - 46 - 48	108.13
62	H28	0.1282112	92 - 93	0.1088	42 - 40 - 41	119.27
63	C25	-0.130076	92 - 94	0.1091	40 - 42 - 50	120.92
64	H29	0.1335952	92 - 95	0.1092	40 - 42 - 43	118.11
65	C26	-0.0257104	16 - 96	0.1457	42 - 50 - 51	111.78
66	H30	0.1252088	96 - 97	0.1085	42 - 50 - 52	111.71
67	C27	-0.2669712	96 - 98	0.1091	42 - 50 - 53	110.36
68	H31	0.1529472	96 - 99	0.1091	43 - 42 - 50	120.91
69	C28	0.1954352	15 - 100	0.1249	52 - 50 - 51	108.70
70	C29	0.4448232	100 - 101	0.1090	53 - 50 - 51	106.95
71	H32	0.0102504	100 - 11	0.1320	53 - 50 - 52	107.12
72	C30	-0.4417632	11 - 102	0.1457	42 - 43 - 44	119.20
73	H33	0.098828	11 - 106	0.1459	42 - 43 - 45	121.95
74	H34	0.1286264	102 - 103	0.1089	45 - 43 - 44	118.84
75	H35	0.1109544	102 - 104	0.1092	43 - 45 - 54	120.47
76	C31	-0.4670712	102 - 105	0.1084	45 - 54 - 55	110.94

77	H36	0.1446664	106 - 107	0.1088	45 - 54 - 56	110.55
78	H37	0.1304984	106 - 108	0.1091	45 - 54 - 57	111.87
79	H38	0.1039544	106 - 109	0.1091	56 - 54 - 55	108.38
80	C32	-0.0619744	2 - 69	0.1368	57 - 54 - 55	107.46
81	H39	0.1189752	2 - 70	0.1467	57 - 54 - 56	107.47
82	C33	-0.3707976	69 - 60	0.1416	19 - 17 - 25	121.36
83	H40	0.1323056	69 - 67	0.1387	17 - 25 - 23	118.39
84	H41	0.1392272	60 - 58	0.1438	17 - 25 - 34	121.37
85	H42	0.1336048	58 - 59	0.1090	17 - 19 - 26	121.28
86	C34	-0.2686904	60 - 61	0.1406	17 - 19 - 20	118.16
87	H43	0.1222616	61 - 62	0.1083	19 - 26 - 27	110.44
88	H44	0.1121408	61 - 63	0.1382	19 - 26 - 28	110.74
89	H45	0.107424	63 - 64	0.1081	19 - 26 - 29	112.41
90	C35	0.085796	63 - 65	0.1393	20 - 19 - 26	120.46
91	H46	0.0533928	65 - 66	0.1082	28 - 26 - 27	106.92
92	C36	-0.3504184	65 - 67	0.1394	29 - 26 - 27	107.43
93	H47	0.1207312	67 - 68	0.1079	29 - 26 - 28	108.70
94	H48	0.1342344	70 - 71	0.1088	19 - 20 - 21	118.82
95	H49	0.1337824	70 - 72	0.1516	19 - 20 - 22	121.97
96	C37	-0.2700856	70 - 76	0.1514	22 - 20 - 21	119.17
97	H50	0.107728	72 - 73	0.1092	20 - 22 - 23	118.13
98	H51	0.1148888	72 - 74	0.1090	20 - 22 - 30	120.62
99	H52	0.1165976	72 - 75	0.1090	30 - 22 - 23	121.25
100	C38	-0.091316	76 - 77	0.1088	22 - 23 - 24	119.29
101	H53	0.118888	76 - 78	0.1091	22 - 23 - 25	121.87
102	C39	-0.3296504	76 - 79	0.1089	22 - 30 - 31	111.29
103	H54	0.1279848	5 - 80	0.1251	22 - 30 - 32	111.09
104	H55	0.1258904	80 - 81	0.1090	22 - 30 - 33	111.53

105	H56	0.116664	80 - 18	0.1317	32 - 30 - 31	106.89
106	C40	-0.3103728	18 - 82	0.1457	33 - 30 - 31	107.95
107	H57	0.1176832	18 - 86	0.1458	33 - 30 - 32	107.89
108	H58	0.125248	86 - 87	0.1085	25 - 23 - 24	118.83
109	H59	0.1249208	86 - 88	0.1090	23 - 25 - 34	120.22
			86 - 89	0.1091	25 - 34 - 35	111.00
			82 - 83	0.1088	25 - 34 - 36	112.03
			82 - 84	0.1090	25 - 34 - 37	111.06
			82 - 85	0.1090	36 - 34 - 35	107.08
					37 - 34 - 35	106.62
					37 - 34 - 36	108.81
					10 - 90 - 91	120.85
					10 - 90 - 16	124.47
					16 - 90 - 91	114.68
					90 - 16 - 92	121.18
					90 - 16 - 96	121.61
					16 - 92 - 93	109.71
					16 - 92 - 94	110.32
					16 - 92 - 95	110.14
					96 - 16 - 92	117.17
					94 - 92 - 93	109.24
					95 - 92 - 93	108.86
					95 - 92 - 94	108.53
					16 - 96 - 97	109.05
					16 - 96 - 98	109.85
					16 - 96 - 99	109.89
					98 - 96 - 97	109.61
					99 - 96 - 97	109.84

99 - 96 - 98	108.58
15 - 100 - 101	120.75
15 - 100 - 11	124.09
11 - 100 - 101	115.15
100 - 11 - 102	122.11
100 - 11 - 106	120.79
106 - 11 - 102	117.09
11 - 102 - 103	109.15
11 - 102 - 104	110.17
11 - 102 - 105	109.42
11 - 106 - 107	109.86
11 - 106 - 108	110.00
11 - 106 - 109	110.02
104 - 102 - 103	108.94
105 - 102 - 103	108.91
105 - 102 - 104	110.22
108 - 106 - 107	109.01
109 - 106 - 107	109.19
109 - 106 - 108	108.73
70 - 2 - 69	121.01
2 - 69 - 60	114.10
2 - 69 - 67	125.37
2 - 70 - 71	107.07
2 - 70 - 72	108.60
2 - 70 - 76	107.33
67 - 69 - 60	120.52
69 - 60 - 58	118.95
69 - 60 - 61	118.63

69 - 67 - 65	119.13
69 - 67 - 68	121.93
60 - 58 - 59	113.72
61 - 60 - 58	122.38
60 - 61 - 62	118.50
60 - 61 - 63	121.02
63 - 61 - 62	120.47
61 - 63 - 64	120.62
61 - 63 - 65	119.14
65 - 63 - 64	120.24
63 - 65 - 66	119.78
63 - 65 - 67	121.52
67 - 65 - 66	118.70
65 - 67 - 68	118.94
72 - 70 - 71	110.40
76 - 70 - 71	108.64
76 - 70 - 72	114.49
70 - 72 - 73	110.95
70 - 72 - 74	110.05
70 - 72 - 75	110.33
70 - 76 - 77	111.41
70 - 76 - 78	109.09
70 - 76 - 79	110.50
74 - 72 - 73	108.14
75 - 72 - 73	108.64
75 - 72 - 74	108.66
78 - 76 - 77	108.95
79 - 76 - 77	108.68

79 - 76 - 78	108.13
5 - 80 - 81	120.93
5 - 80 - 18	123.32
18 - 80 - 81	115.74
80 - 18 - 82	121.05
80 - 18 - 86	121.69
86 - 18 - 82	117.11
18 - 82 - 83	109.87
18 - 82 - 84	109.77
18 - 82 - 85	109.94
18 - 86 - 87	109.34
18 - 86 - 88	109.51
18 - 86 - 89	109.62
88 - 86 - 87	109.98
89 - 86 - 87	109.61
89 - 86 - 88	108.76
84 - 82 - 83	108.85
85 - 82 - 83	109.36
85 - 82 - 84	109.03

References

[1] NIST Computational Chemistry Comparison and Benchmark Database NIST Standard Reference Database Number 101 Release 21, August 2020, Editor: Russell D. Johnson III. DOI:10.18434/T47C7Z.

[2] M. J. Abraham, T. Murtola, R. Schulz, S. Páll, J. C. Smith, B. Hess, and E. Lindahl. Gromacs: High performance molecular simulations through multi-level parallelism from laptops to supercomputers. *SoftwareX*, 1:19–25, 2015.

[3] D. Ajloo, M. Sangian, M. Ghadamgahi, M. Evini, and A. A. Saboury. Effect of two imidazolium derivatives of ionic liquids on the structure and activity of adenosine deaminase. *Int. J. Biol. Macromol.*, 55:47–61, 2013.

[4] J.-M. Andanson, E. Bordes, J. Devémy, F. Leroux, A. A. H. Pádua, and M. F. C. Gomes. Understanding the role of co-solvents in the dissolution of cellulose in ionic liquids. *Green Chem.*, 16:2528–2538, 2014.

[5] H. C. Andersen. Molecular dynamics simulations at constant pressure and/or temperature. *The Journal of Chemical Physics*, 72(4):2384–2393, 1980.

[6] J. L. Anthony, E. J. Maginn, and J. F. Brennecke. Solution thermodynamics of imidazolium-based ionic liquids and water. *J. Phys. Chem. B*, 105(44):10942–10949, 2001.

[7] M. Apostolopoulou, M. S. Santos, M. Hamza, T. Bui, I. G. Economou, M. Stamatakis, and A. Striolo. Quantifying Pore Width Effects on Diffusivity via a Novel 3D Stochastic Approach with Input from Atomistic Molecular Dynamics Simulations. *J. Chem. Theory Comput.*, 15(12):6907–6922, Dec. 2019.

[8] N. Argaman and G. Makov. Density functional theory: An introduction. *American Journal of Physics*, 68(1):69–79, 2000.

[9] B. Autenrieth, E. B. Anderson, D. Wang, and M. R. Buchmeiser. Reactivity of the dicationic ruthenium– alkylidene complex [ru(dmf)$_3$(imesh$_2$)(=ch— 2—(2—pro)—c$_6$h$_4$)]$^{2+}$(bf$_4^-$)$_2$] in ring-opening metathesis and cyclopolymerization. *Macromol. Chem. Phys.*, 214:33–40, 2013.

[10] F. Bardak, D. Xiao, L. G. Hines, P. Son, R. A. Bartsch, E. L. Quitevis, P. Yang, and G. A. Voth. Nanostructural organization in acetonitrile/ionic liquid mixtures: Molecular dynamics simulations and optical kerr effect spectroscopy. *ChemPhysChem*, 13(7):1687–1700, 2012.

[11] B. M. Baynes and B. L. Trout. Proteins in mixed solvents: a molecular-level perspective. *J. Phys. Chem. B*, 107(50):14058–14067, 2003.

[12] A. D. Becke. Perspective: Fifty years of density-functional theory in chemical physics. *The Journal of Chemical Physics*, 140(18):18A301, 2014.

[13] A. Beckmann and F. J. Keil. Increasing yield and operating time of slp-catalyst processes by flow reversal and instationary operation. *Chem. Eng. Sci.*, 58:841–847, 2003.

[14] A. Ben-Naim. Inversion of the kirkwood–buff theory of solutions: application to the water–ethanol system. *J. Chem. Phys.*, 67(11):4884–4890, 1977.

[15] A. Ben-Naim. *Statistical Thermodynamics for Chemists and Biochemists*. Springer Science & Business Media, Berlin, Germany, 2013.

[16] H. J. C. Berendsen, J. P. M. Postma, W. F. van Gunsteren, A. DiNola, and J. R. Haak. Molecular dynamics with coupling to an external bath. *The Journal of Chemical Physics*, 81(8):3684–3690, 1984.

[17] C. E. S. Bernardes, K. Shimizu, and J. N. C. Lopes. Solvent effects on the polar network of ionic liquid solutions. *J. Phys. Cond. Matter*, 27(19):194116, 2015.

[18] A. Boţan, F.-J. Ulm, R. J.-M. Pellenq, and B. Coasne. Bottom-up model of adsorption and transport in multiscale porous media. *Phys. Rev. E*, 91:032133, 2015.

[19] A. Bondi. van der waals volumes and radii. *J. Phys. Chem.*, 68:441–451, 1964.

[20] P. Bonhôte, A.-P. Dias, N. Papageorgiou, K. Kalyanasundaram, , and M. Gra1tzel. Hydrophobic, highly conductive ambient-temperature molten salts. *Inorg. Chem.*, 35:1168–1178, 1996.

[21] F. Borghi and A. Podestà. Ionic liquids under nanoscale confinement. *Adv. Phys. X*, 5:1736949, 2020.

[22] M. Born and R. Oppenheimer. Zur quantentheorie der molekeln. *Ann. Phys.*, 389:457–484, 1927.

[23] C. M. Breneman and K. B. Wiberg. Determining atom-centered monopoles from molecular electrostatic potentials. the need for high sampling density in formamide conformational analysis. *J. Comput. Chem.*, 11(3):361–373, 1990.

[24] Z. Brkljača, M. Klimczak, Z. Miličević, M. Weisser, N. Taccardi, P. Wasserscheid, D. M. Smith, A. Magerl, and A.-S. Smith. Complementary Molecular Dynamics and X-ray Reflectivity Study of an Imidazolium-Based Ionic Liquid at a Neutral Sapphire Interface. *J. Phys. Chem. Lett.*, 6(3):549–555, Feb. 2015.

[25] M. Bru, R. Dehn, J. H. Teles, S. Deuerlein, M. Danz, I. B. Müller, and M. Limbach. Ruthenium carbenes supported on mesoporous silicas as highly active and selective hybrid catalysts for olefin metathesis reactions under continous flow. *Chem. Eur. J.*, 19:11661–11671, 2013.

[26] P. R. Burney, E. M. Nordwald, K. Hickman, J. L. Kaar, and J. Pfaendtner. Molecular dynamics investigation of the ionic liquid/enzyme interface: Application to engineering enzyme surface charge. *Prot. Struct. Funct. Bionform.*, 83(4):670–680, 2015.

[27] G. Bussi, D. Donadio, and M. Parrinello. Canonical sampling through velocity rescaling. *The Journal of Chemical Physics*, 126(1):014101, 2007.

[28] G. Bussi, D. Donadio, and M. Parrinello. Canonical sampling through velocity rescaling. *J. Chem. Phys.*, 126(1):014101, 2007.

[29] S. F. M. C. Nanjundiah and V. R. Koch. Differential capacitance measurements in solvent-free ionic liquids at hg and c interfaces. *J. Electrochem. Soc.*, 144:3392–3397, 1997.

[30] C. Caleman, P. J. van Maaren, M. Hong, J. S. Hub, L. T. Costa, and D. van der Spoel. Force field benchmark of organic liquids: Density, enthalpy of vaporization, heat capacities, surface tension, isothermal compressibility, volumetric expansion coefficient, and dielectric constant. *J. Chem. Theory Comput.*, 8(1):61–74, 2012.

[31] L. Cammarata, S. Kazarian, P. Salter, and T. Welton. Molecular states of water in room temperature ionic liquids. *Phys. Chem. Chem. Phys.*, 3(23):5192–5200, 2001.

[32] J. Canongia Lopes, M. F. Costa Gomes, P. Husson, A. A. Pádua, L. P. N. Rebelo, S. Sarraute, and M. Tariq. Polarity, viscosity, and ionic conductivity of liquid mixtures containing [c4c1im][ntf2] and a molecular component. *J. Phys. Chem. B*, 115(19):6088–6099, 2011.

[33] J. N. Canongia Lopes, J. Deschamps, and A. A. Pádua. Modeling ionic liquids using a systematic all-atom force field. *J. Phys. Chem. B*, 108(6):2038–2047, 2004.

[34] J. Cascão, W. Silva, A. S. D. Ferreira, and E. J. Cabrita. Ion pair and solvation dynamics of [bmim][bf_4] + water system. *Magn. Reson. Chem.*, 56:127–139, 2018.

[35] V. V. Chaban and O. V. Prezhdo. Ionic and molecular liquids: Working together for robust engineering. *J. Phys. Chem. Lett.*, 4(9):1423–1431, 2013.

[36] D. L. Chapman. Li. a contribution to the theory of electrocapillarity. *The London, Edinburgh, and Dublin Philosophical Magazine and Journal of Science*, 25:475–481, 1913.

[37] R. Chitra and P. E. Smith. Preferential interactions of cosolvents with hydrophobic solutes. *J. Phys. Chem. B*, 105(46):11513–11522, 2001.

[38] D. Constantinescu, H. Weingärtner, and C. Herrmann. Protein denaturation by ionic liquids and the hofmeister series: A case study of aqueous solutions of ribonuclease a. *Angew. Chem. Int. Ed.*, 46(46):8887–8889, 2007.

[39] D. Constatinescu, C. Herrmann, and H. Weingärtner. Patterns of protein unfolding and protein aggregation in ionic liquids. *Phys. Chem. Chem. Phys.*, 12(8):1756–1763, 2010.

[40] R. Cortes-Huerto, K. Kremer, and R. Potestio. Kirkwood-buff integrals in the thermodynamic limit from small-sized molecular dynamics simulations. *J. Chem. Phys.*, 145(14):141103, 2016.

[41] E. Courtenay, M. Capp, C. Anderson, and M. Record. Vapor pressure osmometry studies of osmolyte-protein interactions: implications for the action of osmoprotectants in vivo and for the interpretation of "osmotic stress" experiments in vitro. *Biochemistry*, 39(15):4455–4471, 2000.

[42] K. Cui, A. Yethiraj, and J. R. Schmidt. Influence of charge scaling on the solvation properties of ionic liquid solutions. *J. Phys. Chem. B*, 123:9222–9229, 2019.

[43] T. Cui, A. Lahiri, T. Carstens, N. Borisenko, G. Pulletikurthi, C. Kuhl, and F. Endres. Influence of water on the electrified ionic liquid/solid interface: A direct observation of the transition from a multilayered structure to a double-layer structure. *J. Phys. Chem. C*, 120(17):9341–9349, 2016.

[44] Y. Danten, M. I. Cabaco, and M. Besnard. *J. Phys. Chem. A*, 113:2873–2889, 2009.

[45] T. Darden, D. York, and L. Pedersen. Particle mesh ewald: An n· log (n) method for ewald sums in large systems. *J. Chem. Phys.*, 98(12):10089–10092, 1993.

[46] R. Datta and R. G. Rinker. Supported liquid-phase catalysis: I. a theoretical model for transport and reaction. *J. Catal.*, 95:181–192, 1985.

[47] M. J. Dewar, E. G. Zoebisch, E. F. Healy, and J. J. Stewart. Development and use of quantum mechanical molecular models. 76. am1: A

new general purpose quantum mechanical molecular model. *J. Am. Chem. Soc.*, 107(13):3902–3909, 1985.

[48] D. Diddens, V. Lesch, A. Heuer, and J. Smiatek. *to be submitted*, 2016.

[49] D. Diddens, V. Lesch, A. Heuer, and J. Smiatek. Aqueous ionic liquids and their influence on peptide conformations: Denaturation and dehydration mechanisms. *Phys. Chem. Chem. Phys.*, pages 20430–20440, 2017.

[50] B. Docampo-Álvarez, V. Gómez-González, T. Méndez-Morales, J. Carrete, J. R. Rodríguez, Ó. Cabeza, L. J. Gallego, and L. M. Varela. Mixtures of protic ionic liquids and molecular cosolvents: A molecular dynamics simulation. *J. Chem. Phys.*, 140(21):214502, 2014.

[51] B. Doliwa and A. Heuer. Cage effect, local anisotropies, and dynamic heterogeneities at the glass transition: A computer study of hard spheres. *Phys. Rev. Lett.*, 80(22):4915, 1998.

[52] J. Dupont, R. F. de Souza, and P. A. Z. Suarez. Ionic liquid (molten salt) phase organometallic catalysis. *Chem. Rev.*, 102:3667–3692, 2002.

[53] F. Endres, N. Borisenko, R. H. S. Z. El Abedin, and R. Atkin. The interface ionic liquid(s)/electrode(s): In situ stm and afm measurements. *Faraday Discuss*, 154:221–233, 2012.

[54] U. Essmann, L. Perera, M. L. Berkowitz, T. Darden, H. Lee, and L. G. Pedersen. A smooth particle mesh ewald method. *J. Chem. Phys.*, 103(19):8577–8593, 1995.

[55] D. M. P. *et al*. Stable silicon-ionic liquid interface for next-generation lithium-ion batteries. *Nature Communications*, 6, 2015.

[56] E. D. B. *et al*. Co2 capture by a task-specific ionic liquid. *J. Am. Chem. Soc.*, 124(6):926–927, 2002.

[57] F. D. F. *et al*. Water sorption by anhydrous ionic liquids. *Green Chem.*, 13:1712, 2011.

[58] H. L. N. *et al*. Thermal properties of imidazolium ionic liquids. *Thermochimica Acta*, pages 97–102, 2000.

[59] J. G. H. *et al*. Characterization and comparison of hydrophilic and hydrophobic room temperature ionic liquids incorporating the imidazolium cation. *Green Chemistry*, 3(7):156–164, 2001.

[60] M. M. *et al*. Ionic liquid electrolytes for safer lithium batteries. *Journal of The Electrochemical Society*, 164(1):A6026–A6031, 2017.

[61] R. F. S. *et al*. Room temperature dialkylimidazolium ionic liquid-based fuel cells. *Electrochemistry Communications*, 5(8):728–731, 2003.

[62] W. S. *et al*. The effect of dissolved water on the viscosities of hydrophobic room-temperature ionic liquids. *Phys. Chem. Chem. Phys.*, 14:15897–15908, 2012.

[63] B. Fazio, A. Triolo, and G. D. Marco. Local organization of water and its effect on thestructural heterogeneities in room-temperature ionicliquid/$h_2$omixtures. *J. Raman Spectrosc.*, 39:233–237, 2008.

[64] G. Feng, X. Jiang, R. Qiao, and A. A. Kornyshev. Water in ionic liquids at electrified interfaces: The anatomy of electrosorption. *ACS Nano*, 8(11):11685–11694, 2014.

[65] E. Fermi. Un metodo statistico per la determinazione di alcune prioprietà dell'atomo. endiconti. *Accademia Nazionale dei Lincei*, 6:602–607, 1927.

[66] M. Foroutana, S. M. Fatemi, and F. Esmaeilian. A review of the structure and dynamics of nanoconfined water and ionic liquids via molecular dynamics simulation. *Eur. Phys. J. E*, 40:19, 2017.

[67] G. Franciò, U. Hintermair, and W. Leitner. Unlocking the potential of supported liquid phase catalysts with supercritical fluids: low temperature continuous flow catalysis with integrated product separation. *Phil. Trans. R. Soc. A*, 373:20150005, 2015.

[68] M. Fyta and R. R. Netz. Ionic force field optimization based on single-ion and ion-pair solvation properties: Going beyond standard mixing rules. *J. Chem. Phys.*, 136(12):124103, 2012.

[69] S. Gabriel and J. Weiner. Ueber einige abkömmlinge des propylamins. *Ber.*, 21(2):2669–2679, 1888.

[70] P. Ganguly and N. F. van der Vegt. Convergence of sampling kirkwood–buff integrals of aqueous solutions with molecular dynamics simulations. *J. Chem. Theory Comput.*, 9(3):1347–1355, 2013.

[71] A. García, I. I. Slowing, and J. W. Evans. Pore diameter dependence of catalytic activity: p-nitrobenzaldehyde conversion to an aldol product in amine-functionalized mesoporous silica. *J. Chem. Phys.*, 149:024101, 2018.

[72] A. García, I. I. Slowing, and J. W. Evans. Pore diameter dependence of catalytic activity: *p* -nitrobenzaldehyde conversion to an aldol product in amine-functionalized mesoporous silica. *J. Chem. Phys.*, 149(2):024101, July 2018.

[73] M. B. Gee, N. R. Cox, Y. Jiao, N. Bentenitis, S. Weerasinghe, and P. E. Smith. A kirkwood-buff derived force field for aqueous alkali halides. *J. Chem. Theory Comput.*, 7(5):1369–1380, 2011.

[74] F. Goettmann and C. Sanchez. How does confinement affect the catalytic activity of mesoporous materials. *J. Mater. Chem.*, 17:24–30, 2007.

[75] S. Grimme, S. Ehrlich, and L. Goerigk. Effect of the damping function in dispersion corrected density functional theory. *J. Comput. Chem.*, 32:1456–1465, 2011.

[76] D. Hall. Kirkwood-buff theory of solutions. an alternative derivation of part of it and some applications. *Transact. Farad. Soc.*, 67:2516–2524, 1971.

[77] C. Hanke, N. Atamas, and R. Lynden-Bell. Solvation of small molecules in imidazolium ionic liquids: a simulation study. *Green Chem.*, 4(2):107–111, 2002.

[78] N. Hansen and F. J. Keil. Multiscale modeling of reaction and diffusion in zeolites: From the molecular level to the reactor. *Soft Mater.*, 10:179–201, 2012.

[79] M. Haumann and P. Wasserscheid. Supported liquid phase catalysis. In B. Cornils, W. A. Herrmann, M. Beller, and R. Paciello, editors, *Applied Homogeneous Catalysis with Organometallic Compounds: A Com-*

prehensive Handbook in Four Volumes, pages 999–1067. Wiley-VCH, Weinheim, 3rd edition, 2018.

[80] R. Hayes, S. Imberti, G. G. Warr, and R. Atkin. How water dissolves in protic ionic liquids. *Angew. Chem. Int. Ed.*, 51(30):7468–7471, 2012.

[81] B. Hess, H. Bekker, H. J. C. Berendsen, and J. G. E. M. Fraaije. LINCS: A linear constraint solver for molecular simulations. *J. Comput. Chem.*, 18:1463–1472, 1997.

[82] J. D. Holbrey and K. R. Seddon. The phase behaviour of 1-alkyl-3-methylimidazolium tetrafluoroborates; ionic liquids and ionic liquid crystals. *J. Chem. Soc. Dalton Trans.*, pages 2133–2140, 1999.

[83] W. G. Hoover. Canonical dynamics: Equilibrium phase-space distributions. *Phys. Rev. A*, 31:1695–1697, Mar 1985.

[84] P. Huber. Soft matter in hard confinement: Phase transition thermodynamics, structure, texture, diffusion and flow in nanoporous media. *J. Phys.: Condens. Matter*, 27:103102, 2015.

[85] J. G. Huddleston, A. E. Visser, W. M. Reichert, H. D. Willauer, G. A. Broker, and R. D. Rogers. Characterization and comparison of hydrophilic and hydrophobic room temperature ionic liquids incorporating the imidazolium cation. *Green Chem.*, 3(4):156–164, 2001.

[86] P. A. Hunt. Quantum chemical modeling of hydrogen bonding in ionic liquids. *Top. Curr. Chem. (Z)*, 375(59), 2017.

[87] F. Huo, Z. Liu, and W. Wang. Cosolvent or antisolvent? a molecular view of the interface between ionic liquids and cellulose upon addition of another molecular solvent. *J. Phys. Chem. B*, 117:11780–11792, 2013.

[88] M. Ide, M. El-Roz, E. De Canck, A. Vicente, T. Planckaert, T. Bogaerts, I. Van Driessche, F. Lynen, V. Van Speybroeck, F. Thybault-Starzyk, and P. Van Der Voort. Quantification of silanol sites for the most common mesoporous ordered silicas and organosilicas: total versus accessible silanols. *Phys. Chem. Chem. Phys.*, 15:642–650, 2013.

[89] Y. Jeon, J. Sung, D. Kim, C. Seo, H. Cheong, Y. Ouchi, R. Ozawa, and H.-o. Hamaguchi. Structural change of 1-butyl-3-methylimidazolium tetrafluoroborate+ water mixtures studied by infrared vibrational spectroscopy. *J. Phys. Chem. B*, 112(3):923–928, 2008.

[90] J.-C. Jiang, K.-H. Lin, S.-C. Li, P.-M. Shih, K.-C. Hung, S. H. Lin, and H.-C. Chang. Association structures of ionic liquid/dmso mixtures studied by high-pressure infrared spectroscopy. *J. Chem. Phys.*, 134:044506, 2011.

[91] W. Jiang, Y. Wang, and G. A. Voth. Molecular dynamics simulation of nanostructural organization in ionic liquid/water mixtures. *J. Phys. Chem. B*, 4:6, 2007.

[92] M. Jitvisate and J. R. T. Seddon. Local structure and flow properties of ionic liquids on charged and inert substrates. *J. Phys. Chem. C*, 120:4860–4865, 2016.

[93] M. Jitvisate and J. R. T. Seddon. Near-wall molecular ordering of dilute ionic liquids. *J. Phys. Chem. C*, 121:18593–18597, 2017.

[94] E. R. Johnson and A. D. Beckea. A post-hartree-fock model of intermolecular interactions: Inclusion of higher-order corrections. *J. Chem. Phys.*, 124:174104, 2006.

[95] W. L. Jorgensen, D. S. Maxwell, and J. Tirado-Rives. Development and testing of the opls all-atom force field on conformational energetics and properties of organic liquids. *J. Am. Chem. Soc.*, 118(45):11225–11236, 1996.

[96] H. Katayanagi, K. Nishikawa, H. Shimozaki, K. Miki, P. Westh, and Y. Koga. Mixing schemes in ionic liquid- h20 systems: A thermodynamic study. *J. Phys. Chem. B*, 108(50):19451–19457, 2004.

[97] H. Kato, K. Nishikawa, H. Murai, T. Morita, and Y. Koga. Chemical potentials in aqueous solutions of some ionic liquids with the 1-ethyl-3-methylimidazolium cation. *J. Phys. Chem. B*, 112(42):13344–13348, 2008.

[98] F. J. Keil. Molecular modelling for reactor design. *Annu. Rev. Chem. Biomol. Eng.*, 9:201–227, 2018.

[99] A. Khan and C. Zhao. Enhanced performance in mixture dmso/ionic liquid electrolytes:toward rechargeable li–o2batteries. *Electrochemistry Communications*, 49:1–4, 2014.

[100] A. L. Kiratidis and S. J. Miklavcic. Density functional theory of confined ionic liquids: A survey of the effects of ion type, molecular charge distribution, and surface adsorption. *J. Chem. Phys.*, 150:184502, 2019.

[101] J. G. Kirkwood and F. P. Buff. The statistical mechanical theory of solutions. i. *J. Chem. Phys.*, 19(6):774–777, 1951.

[102] T. Kobayashi, A. Kemna, M. Fyta, B. Braunschweig, and J. Smiatek. Aqueous mixtures of room-temperature ionic liquids: Entropy-driven accumulation of water molecules at interfaces. *J. Phys. Chem. C*, 123(22):13795–13803, 2019.

[103] T. Kobayashi, H. Kraus, N. Hansen, and M. Fyta. Confined ru-catalysts in a two-phase heptane/ionic liquid solution: Modeling aspects. *ChemCatChem*, 13(2):739–746, 2021.

[104] T. Kobayashi, J. E. Reid, S. Shimizu, M. Fyta, and J. Smiatek. The properties of residual water molecules in ionic liquids: A comparison between direct and inverse Kirkwood–Buff approaches. *Phys. Chem. Chem. Phys.*, 19:18924–18937, 2017.

[105] T. Kobayashi, J. Smiatek, and M. Fyta. Energetic arguments on the microstructural analysis in ionic liquids. *Adv. Theory Simul.*, 2021.

[106] W. Kohn and L. J. Sham. Self-consistent equations including exchange and correlation effects. *Phys. Rev.*, 140:A1133–A1138, Nov 1965.

[107] A. A. Kornyshev. Double-layer in ionic liquids: paradigm change? *J. Phys. Chem. B*, 111:5545–5557, 2007.

[108] H. Kraus and N. Hansen. Porems: 0.2.0, https://doi.org/10.5281/zenodo.3984865,. 2020.

[109] H. Kraus, J. Rybka, A. Höltzel, N. Trebel, U. Tallarek, and N. Hansen. Porems: a software tool for generating silica pore models with user-defined surface functionalisation and pore dimensions. *Molecular Simulation*, 47(4):306–316, 2021.

[110] R. Krishna. Describing the Diffusion of Guest Molecules Inside Porous Structures. *J. Phys. Chem. C*, 113(46):19756–19781, Nov. 2009.

[111] P. Krüger, S. K. Schnell, D. Bedeaux, S. Kjelstrup, T. J. Vlugt, and J.-M. Simon. Kirkwood–buff integrals for finite volumes. *J. Phys. Chem. Lett.*, 4(2):235–238, 2012.

[112] S. Kumar, J. M. Rosenberg, D. Bouzida, R. H. Swendsen, and P. A. Kollman. The weighted histogram analysis method for free-energy calculations on biomolecules. i. the method. *Journal of Computational Chemistry*, 13(8):1011–1021, 1992.

[113] P. G. Kusalik and G. Patey. The thermodynamic properties of electrolyte solutions: Some formal results. *J. Chem. Phys.*, 86(9):5110–5116, 1987.

[114] P. G. Kusalik and G. Patey. On the molecular theory of aqueous electrolyte solutions. i. the solution of the rhnc approximation for models at finite concentration. *J. Chem. Phys.*, 88(12):7715–7738, 1988.

[115] P. G. Kusalik and G. Patey. On the molecular theory of aqueous electrolyte solutions. ii. structural and thermodynamic properties of different models at infinite dilution. *J. Chem. Phys.*, 89(9):5843–5851, 1988.

[116] P. G. Kusalik and G. Patey. On the molecular theory of aqueous electrolyte solutions. iii. a comparison between born–oppenheimer and mcmillan–mayer levels of description. *J. Chem. Phys.*, 89(12):7478–7484, 1988.

[117] J. Lebowitz and J. Percus. Long-range correlations in a closed system with applications to nonuniform fluids. *Phys. Rev.*, 122(6):1675, 1961.

[118] S.-Y. Lee, A. Ogawa, M. Kanno, H. Nakamoto, T. Yasuda, and M. Watanabe. Nonhumidified intermediate temperature fuel cells using protic ionic liquids. *J. Am. Chem. Soc.*, 132(28):9764–9773, 2010.

[119] V. Lesch, A. Heuer, C. Holm, and J. Smiatek. Solvent effects of 1-ethyl-3-methylimidazolium acetate: Solvation and dynamic behavior of polar and apolar solutes. *Phys. Chem. Chem. Phys.*, 17(13):8480–8490, 2015.

[120] V. Lesch, A. Heuer, C. Holm, and J. Smiatek. Properties of apolar solutes in alkyl imidazolium-based ionic liquids: The importance of local interactions. *ChemPhysChem*, 17(3):387–394, 2016.

[121] V. Lesch, A. Heuer, B. R. Rad, M. Winter, and J. Smiatek. Atomistic insights into deep eutectic electrolytes: The influence of urea on the electrolyte salt litfsi in view of electrochemical applications. *Phys. Chem. Chem. Phys.*, 18(41):28403–28408, 2016.

[122] V. Lesch, A. Heuer, V. A. Tatsis, C. Holm, and J. Smiatek. Peptides in the presence of aqueous ionic liquids: Tunable co-solutes as denaturants or protectants? *Phys. Chem. Chem. Phys.*, 17(39):26049–26053, 2015.

[123] A. Lewandowski and A. Swiderska-Mocek. Ionic liquids as electrolytes for li-ion batterie – an overview of electrochemical studies. *J. Power Sources*, 194(26):601–609, 2009.

[124] X. Liu, T. J. H. Vlugt, and A. Bardow. Maxwell–stefan diffusivities in binary mixtures of ionic liquids with dimethyl sulfoxide (dmso) and h20. *The Journal of Physical Chemistry B*, 115(26):8506–8517, 2011. PMID: 21627315.

[125] H. Livbjerg, T. S. Christensen, T. T. Hansen, and J. Villadsen. Theoretical foundation of cluster formation in supported liquid-phase catalysts. *Sādhanā*, 10:185–216, 1987.

[126] A. Maiti, A. Kumar, and R. D. Rogers. *Phys. Chem. Chem.Phys.*, 14:5139–5146, 2012.

[127] E. L. Margelesfky, R. K. Zeidan, and M. E. Davis. Cooperative catalysis by silica-supported organic functional groups. *Chem. Soc. Rev.*, 37:1118–1126, 2008.

[128] F. Marras, J. Wang, M.-O. Coppens, and J. N. H. Reek. Ordered mesoporous materials as solid supports for rhodium-diphosphine catalysts with remarkable hydroformulation activity. *Chem. Comm.*, 46:6587–6589, 2010.

[129] L. Martin, H. Martinez, M. Ulldemolins, B. Pecquenard, and F. L. Cras. Evolution of the si electrode/electrolyte interface in lithium batteries

characterized by xps and afm techniques: The influence of vinylene carbonate additive. *Solid State Ionics*, 215:36–44, 2012.

[130] L. Martínez, R. Andrade, E. G. Birgin, and J. M. Martínez. Packmol: a package for building initial configurations for molecular dynamics simulations. *J. Comput. Chem.*, 30(13):2157–2164, 2009.

[131] G. J. Martyna, M. E. Tuckerman, D. J. Tobias, and M. L. Klein. Explicit reversible integrators for extended systems dynamics. *Molecular Physics*, 87(5):1117–1157, 1996.

[132] D. McFarlane, J. Sun, J. Golding, P. Meakin, and M. Forsyth. High conductivity molten salts based on the imide ion. *Electrochim. Acta*, 45:1271–1278, 2000.

[133] T. Méndez-Morales, J. Carrete, O. Cabeza, L. J. Gallego, and L. M. Varela. Molecular dynamics simulation of the structure and dynamics of water–1-alkyl-3-methylimidazolium ionic liquid mixtures. *J. Phys. Chem. B*, 115(21):6995–7008, 2011.

[134] T. Méndez-Morales, J. Carrete, M. García, O. Cabeza, L. J. Gallego, and L. M. Varela. Dynamical properties of alcohol + 1-hexyl-3-methylimidazolium ionic liquid mixtures: A computer simulation study. *J. Phys. Chem. B*, 115(51):15313–15322, 2011.

[135] N. M. Micaêlo and C. M. Soares. Protein structure and dynamics in ionic liquids. insights from molecular dynamics simulation studies. *J. Phys. Chem. B*, 112(9):2566–2572, 2008.

[136] S. Micciulla, J. Michalowsky, M. A. Schroer, C. Holm, R. von Klitzing, and J. Smiatek. Concentration dependent effects of urea binding to poly (n-isopropylacrylamide) brushes: a combined experimental and numerical study. *Phys. Chem. Chem. Phys.*, 18(7):5324–5335, 2016.

[137] Molinformation-Cheminformatics. https://www.molinspiration.com/cgi-bin/properties. last accessed on February 25th, 2019.

[138] M. Moreno, F. Castiglione, A. Mele, C. Pasqui, and G. Raos. Interaction of water with the model ionic liquid [bmim][bf4]: Molecular dynamics simulations and comparison with nmr data. *J. Phys. Chem. B*, 112(26):7826–7836, 2008.

[139] F. Neese. The orca program system. *WIREs Comput. Mol. Sci.*, 2:73–78, 2012.

[140] K. E. Newman. Kirkwood–buff solution theory: derivation and applications. *Chem. Soc. Rev.*, 23(1):31–40, 1994.

[141] A. Noda, S. M. K. H. Md. A. B. H. Susan, K Kudo, and M. Watanabe. Brønsted acid-base ionic liquids as proton-conducting nonaqueous electrolytes. *J. Phys. Chem. B*, 107(17):4024–4033, 2003.

[142] S. Nosé. A molecular dynamics method for simulations in the canonical ensemble. *Molecular Physics*, 52(2):255–268, 1984.

[143] S. Nosé and M. Klein. Constant pressure molecular dynamics for molecular systems. *Molecular Physics*, 50(5):1055–1076, 1983.

[144] E. A. Oprzeska-Zingrebe and J. Smiatek. Aqueous ionic liquids in comparison with standard co-solutes. *Biophys. Rev.*, pages 1–16, 2018.

[145] J. M. Otero-Mato, H. Montes-Campos, O. Cabeza, D. Diddens, A. Ciach, L. J. Gallego, and L. M. Varela. 3d structure of the electric double layer of ionic liquid–alcohol mixtures at the electrochemical interface. *Phys. Chem. Chem. Phys.*, 20(48):30412–30427, 2018.

[146] M. Parrinello and A. Rahman. Polymorphic transitions in single crystals: A new molecular dynamics method. *Journal of Applied Physics*, 52(12):7182–7190, 1981.

[147] M. Parrinello and A. Rahman. Polymorphic transitions in single crystals: A new molecular dynamics method. *J. Appl. Phys.*, 52(12):7182–7190, 1981.

[148] R. Patel, M. Kumari, and A. B. Khan. Recent advances in the application of ionic liquids in protein stability and activity: A review. *Appl. Biochem. Biotechnol.*, 172:3701–3720, 2014.

[149] J. K. S. Patrick Yee and E. J. Maginn. State of hydrophobic and hydrophilic ionic liquids in aqueous solutions: Are the ions fully dissociated? *J. Phys. Chem. B*, 117:12556–12566, 2013.

[150] E. Perit, P. Ray, A. Hansen, F. Malberg, S. Grimme, and B. Kirchner. Finding the best density functional approximation to describe interaction energies and structures of ionic liquids in molecular dynamics studies. *J. Chem. Phys.*, 148:193835, 2018.

[151] S. Perkin. Ionic liquids in confined geometries. *Phys. Chem. Chem. Phys.*, page 5052–5062, 2012.

[152] V. Pierce, M. Kang, M. Aburi, S. Weerasinghe, and P. E. Smith. Recent applications of kirkwood-buff theory to biological systems. *Cell. Biochem. Biophys.*, 50:1–22, 2008.

[153] V. Pierce, M. Kang, M. Aburi, S. Weerasinghe, and P. E. Smith. Recent applications of kirkwood-buff theory to biological systems. *Cell. Biochem. Biophys.*, 50:1–22, 2008.

[154] S. Pronk, S. Páll, R. Schulz, P. Larsson, P. Bjelkmar, R. Apostolov, M. R. Shirts, J. C. Smith, P. M. Kasson, D. van der Spoel, B. Hess, and E. Lindahl. Gromacs 4.5: A high-throughput and highly parallel open source molecular simulation toolkit. *Bioinformatics*, 29(7):845, 2013.

[155] P. Pulay. Convergence acceleration of iterative sequences. the case of SCF iteration. *Chem. Phys. Lett.*, 73:393–398, 1980.

[156] E. Pump, Z. Cao, M. K. Samantaray, A. Bendjeriou-Sedjerari, L. Cavallo, and J.-M. Basset. Exploiting confinement effects to tune selectivity in cyclooctane metathesis. *ACS Catal.*, 7:6581–6586, 2017.

[157] I. Płowaś, J. Świergiel, and J. Jadżyn. Relative static permittivity of dimethyl sulfoxide + water mixtures. *Journal of Chemical & Engineering Data*, 58(6):1741–1746, 2013.

[158] G. Rai and A. Kumar. Probing thermal interactions of ionic liquids with dimethyl sulfoxide. *ChemPhysChem*, 13:1927 – 1933, 2012.

[159] F. Ramondo, L. Gontrani, and M. Campetella. Coupled hydroxyl and ether functionalisation in ean derivatives: the effect of hydrogen bond donor/acceptor groups on the structural heterogeneity studied with x-ray diffractions and fixed charge/polarizable simulations. *Phys. Chem. Chem. Phys.*, 21:11464–11475, 2019.

[160] J. E. S. J. Reid, R. J. Gammons, J. M. Slattery, A. J. Walker, and S. Shimizu. Interactions in water–ionic liquid mixtures: Comparing protic and aprotic systems. *J. Phys. Chem. B*, 121:599–609, 2017.

[161] J. E. S. J. Reid, A. J. Walker, and S. Shimizu. Residual water in ionic liquids: Clustered or dissociated? *Phys. Chem. Chem. Phys.*, 17(22):14710–14718, 2015.

[162] R. C. Remsing, Z. Liu, I. Sergeyev, and G. Moyna. Solvation and aggregation of n,n′-dialkylimidazolium ionic liquids: A multinuclear nmr spectroscopy and molecular dynamics simulation study. *The Journal of Physical Chemistry B*, 112(25):7363–7369, 2008. PMID: 18512980.

[163] E. Rilo, L. M. Varela, and O. Cabeza. Density and derived thermodynamic properties of 1-ethyl-3-methylimidazolium alkyl sulfate ionic liquid binary mixtures with water and with ethanol from 288 k to 318 k. *J. Chem. Eng. Data*, 57(8):2136–2142, 2012.

[164] J. B. Rollins, B. D. Fitchett, , and J. C. Conboy. Structure and orientation of the imidazolium cation at the room-temperature ionic liquid/sio2 interface measured by sum-frequency vibrational spectroscopy. *J. Phys. Chem. B*, 111:4990–4999, 2007.

[165] B. A. Rosen, W. Zhu, G. Kaul, A. Salehi-Khojin, and R. I. Masel. Water enhancement of co_2 conversion on silver in 1-ethyl-3-methylimidazolium tetrafluoroborate. *J. Electrochem. Soc.*, 160(2):H138–H141, 2013.

[166] J. Rösgen, B. M. Pettitt, and D. W. Bolen. Uncovering the basis for nonideal behavior of biological molecules. *Biochemistry*, 43(45):14472–14484, 2004.

[167] J. Rösgen, B. M. Pettitt, and D. W. Bolen. Protein folding, stability, and solvation structure in osmolyte solutions. *Biophys. J.*, 89(5):2988–2997, 2005.

[168] J. Rösgen, B. M. Pettitt, and D. W. Bolen. An analysis of the molecular origin of osmolyte-dependent protein stability. *Protein Sci.*, 16(4):733–743, 2007.

[169] E. Ruckenstein and I. L. Shulgin. Effect of salts and organic additives on the solubility of proteins in aqueous solutions. *Adv. Coll. Interface Sci.*, 123:97–103, 2006.

[170] S. V. Sambasivarao and O. Acevedo. Development of opls-aa force field parameters for 68 unique ionic liquids. *J. Chem. Theory Comput.*, 5(4):1038–1050, 2009.

[171] S. K. Schnell, P. Englebienne, J.-M. Simon, P. Krüger, S. P. Balaji, S. Kjelstrup, D. Bedeaux, A. Bardow, and T. J. Vlugt. How to apply the kirkwood–buff theory to individual species in salt solutions. *Chem. Phys. Lett.*, 582:154–157, 2013.

[172] S. K. Schnell, T. J. Vlugt, J.-M. Simon, D. Bedeaux, and S. Kjelstrup. Thermodynamics of small systems embedded in a reservoir: a detailed analysis of finite size effects. *Mol. Phys.*, 110(11-12):1069–1079, 2012.

[173] C. Schröder. Proteins in ionic liquids: Current status of experiments and simulations. *Top. Curr. Chem.*, 375(2):25, 2017.

[174] C. Schröder, J. Hunger, A. Stoppa, R. Buchner, and O. Steinhauser. On the collective network of ionic liquid/water mixtures. ii. decomposition and interpretation of dielectric dpectra. *J. Chem. Phys.*, 129(18):184501, 2008.

[175] C. Schröder, G. Neumayr, and O. Steinhauser. On the collective network of ionic liquid/water mixtures. iii. structural analysis of ionic liquids on the basis of voronoi decomposition. *J. Chem. Phys.*, 130(19):194503, 2009.

[176] C. Schröder, T. Rudas, G. Neumayr, S. Benkner, and O. Steinhauser. On the collective network of ionic liquid/water mixtures. i. orientational structure. *J. Chem. Phys.*, 127(23):234503, 2007.

[177] U. schröder *et al*. Water-induced accelerated ion diffusion : voltammetric studies in 1-methyl-3-[2,6-(s)-dimethylocten-2-yl]imidazolium tetraÑuoroborate, 1-butyl-3-methylimidazolium tetraÑuoroborate and hexaÑuorophosphate ionic liquids. *New J. Chem.*, 24:1009–1015, 2000.

[178] M. A. Schroer, J. Michalowsky, B. Fischer, J. Smiatek, and G. Grübel. Stabilizing effect of tmao on globular pnipam states: preferential attraction induces preferential hydration. *Phys. Chem. Chem. Phys.*, 18(46):31459–31470, 2016.

[179] J. M. Schurr, D. P. Rangel, and S. R. Aragon. A contribution to the theory of preferential interaction coefficients. *Biophys. J.*, 89(4):2258–2276, 2005.

[180] K. R. Seddon, A. Stark, and M.-J. Torres. Influence of chloride, water, and organic solvents on the physical properties of ionic liquids. *Pure Appl. Chem.*, 72(12):2275–2287, 2000.

[181] M. Senske, D. C. Aruxandei, M. Havenith, H. Weingärtner, C. Herrmann, and S. Ebbinghaus. Thermodynamic fingerprints of the hofmeister series-protein interactions with ionic liquids. *Biophys. J.*, 110(3):212a, 2016.

[182] W. Shi and E. J. Maginn. Atomistic simulation of the absorption of carbon dioxide and water in the ionic liquid 1-n-hexyl-3-methylimidazolium bis(trifluoromethylsulfonyl)imide ([hmim][tf2n]). *J. Phys. Chem. B*, 112(7):2045–2055, 2008.

[183] S. Shimizu. Estimating hydration changes upon biomolecular reactions from osmotic stress, high pressure, and preferential hydration experiments. *Proc. Natl. Acad. Sci. USA*, 101(5):1195–1199, 2004.

[184] S. Shimizu and D. J. Smith. Preferential hydration and the exclusion of cosolvents from protein surfaces. *J. Chem. Phys.*, 121(2):1148–1154, 2004.

[185] T. Singh and A. Kumar. Cation–anion–water interactions in aqueous mixtures of imidazolium based ionic liquids. *Vib. Spectrosc.*, 55(1):119–125, 2011.

[186] J. Smiatek. Osmolyte effects: Impact on the aqueous solution around charged and neutral spheres. *J. Phys. Chem. B*, 118(3):771–782, 2014.

[187] J. Smiatek. Aqueous ionic liquids and their influence on protein structures: An overview on recent theoretical and experimental insights. *J. Phys. Condens. Matter*, 29:233001, 2017.

[188] J. Smiatek. Enthalpic contributions to solvent–solute and solvent–ion interactions: Electronic perturbation as key to the understanding of molecular attraction. *J. Chem. Phys.*, 150:174112, 2019.

[189] J. Smiatek. Specific ion effects and the law of matching solvent affinities: A conceptual density functional theory approach. *J. Phys. Chem. B*, 124:2191–2197, 2020.

[190] J. Smiatek. Theoretical and computational insight into solvent and specific ion effects for polyelectrolytes: The importance of local molecular interactions. *Molecules*, 25:1661, 2020.

[191] P. E. Smith. Computer simulation of cosolvent effects on hydrophobic hydration. *J. Phys. Chem. B*, 103(3):525–534, 1999.

[192] P. E. Smith. Cosolvent interactions with biomolecules:relating computer simulation data to experimental thermodynamic data. *J. Phys. Chem. B*, 108:18716–18724, 2004.

[193] P. E. Smith. Chemical potential derivatives and preferential interaction parameters in biological systems from kirkwood-buff theory. *Biophys. J.*, 91(3):849–856, 2006.

[194] P. E. Smith, E. Matteoli, and J. P. O'Connell. *Fluctuation theory of solutions: applications in chemistry, chemical engineering, and biophysics*. CRC Press, 2013.

[195] C. Spickermann, J. Thar, S. Lehmann, S. Zahn, J. Hunger, R. Buchner, P. Hunt, T. Welton, and B. Kirchner. Why are ionic liquid ions mainly associated in water? a car–parrinello study of 1-ethyl-3-methylimidazolium chloride water mixture. *J. Chem. Phys.*, 129(10):104505, 2008.

[196] T. Steiner. C–h o hydrogen bonding in crystals. *Crystallography Reviews*, 9:2-3:177–228, 2003.

[197] P. J. Stephens, F. J. Devlin, C. F. Chabalowski, and M. J. Frisch. Ab initio calculation of vibrational absorption and circular dichroism spectra using density functional force fields. *J. Phys. Chem.*, 98:11623–11627, 1994.

[198] R. Stepić, C. R. Wick, V. Strobel, D. Berger, N. Vučemilović-Alagić, M. Haumann, P. Wasserscheid, A. Smith, and D. M. Smith. Mechanism of the Water–Gas Shift Reaction Catalyzed by Efficient Ruthenium-Based Catalysts: A Computational and Experimental Study. *Angew. Chem. Int. Ed.*, 58(3):741–745, Jan. 2019.

[199] T. Takamuku, H. Hoke, A. Idrissi, B. A. Marekha, M. Moreau, Y. Honda, T. Umeckya, and T. Shimomurad. Microscopic interactions of the imidazolium-based ionic liquid with molecular liquids depending on their electron-donicity. *Phys. Chem. Chem. Phys.*, 16:23627–23638, 2014.

[200] U. Tallarek, D. Hlushkou, J. Rybka, and A. Höltzel. Multiscale Simulation of Diffusion in Porous Media: From Interfacial Dynamics to Hierarchical Porosity. *J. Phys. Chem. C*, 123(24):15099–15112, June 2019.

[201] Z. Terranova and S. Corcelli. Molecular dynamics investigation of the vibrational spectroscopy of isolated water in an ionic liquid. *J. Phys. Chem. B*, 118(28):8264–8272, 2014.

[202] L. H. Thomas. The calculation of atomic fields. *Mathematical Proceedings of the Cambridge Philosophical Society*, 23(5):542–548, 1927.

[203] G. Torrie and J. Valleau. Nonphysical sampling distributions in monte carlo free-energy estimation: Umbrella sampling. *Journal of Computational Physics*, 23(2):187–199, 1977.

[204] T. M. Truskett, S. Torquato, and P. G. Debenedetti. Towards a quantification of disorder in materials: Distinguishing equilibrium and glassy sphere packings. *Phys. Rev. E*, 62(1):993, 2000.

[205] S. Tsuzuki. Factors controlling the diffusion of ions in ionic liquids. *ChemPhysChem*, 13:1664–1670, 2012.

[206] S. Tsuzuki, W. Shinoda, H. Saito, M. Mikami, H. Tokuda, and M. Watanabe. Molecular dynamics simulations of ionic liquids: Cation and anion dependence of self-diffusion coefficients of ions. *J. Phys. Chem. B*, 113:10641–10649, 2009.

[207] P. Tundo and A. Perosa. Multiphasic heterogeneous catalysis mediated by catalyst-philic liquid phases. *Chem. Soc. Rev.*, 36:532–550, 2007.

[208] D. Van Der Spoel, E. Lindahl, B. Hess, G. Groenhof, A. E. Mark, and H. J. Berendsen. Gromacs: fast, flexible, and free. *J. Comput. Chem.*, 26(16):1701–1718, 2005.

[209] J. Villadsen and H. Livejerg. Supported liquid-phase catalysts. *Catal. Rev.-Sci. Eng.*, 17:203–272, 1978.

[210] N. Vučemilović-Alagić, R. D. Banhatti, R. Stepić, C. R. Wick, D. Berger, M. U. Gaimann, A. Baer, J. Harting, D. M. Smith, and A.-S. Smith. Insights from molecular dynamics simulations on structural organization and diffusive dynamics of an ionic liquid at solid and vacuum interfaces. *J. Colloid Interface Sci.*, 553:350–363, Oct. 2019.

[211] P. Walden. Molecular weights and electrical conductivity of several fused salts. *Bull. Acad. Imper. Sci. St. Petersburg*, 8:405–422, 1914.

[212] J. Wang, Q. Ma, Y. Wang, Z. Li, Z. Li, and Q. Yuan. New insights into the structure-performance relationships of mesoporous materials in analytical science. *Chem. Soc. Rev.*, 47:8766–8803, 2018.

[213] N.-N. Wang, Q.-G. Zhang, F.-G. Wu, Q.-Z. Li, and Z.-W. Yu. Hydrogen bonding interactions between a representative pyridinium-based ionic liquid [bupy][bf4] and water/dimethyl sulfoxide. *The Journal of Physical Chemistry B*, 114(26):8689–8700, 2010. PMID: 20550148.

[214] Y. Wang, H. Li, and S. Han. A theoretical investigation of the interactions between water molecules and ionic liquids. *J. Phys. Chem. B*, 110(48):24646–24651, 2006.

[215] Z. Wang, H. Li, R. Atkin, and C. Priest. Influence of water on the interfacial nanostructure and wetting of [rmim][ntf2] ionic liquids at mica surfaces. *Langmuir*, 32(35):8818–8825, 2016.

[216] P. Wasserscheid and W. Keim. Ionic liquids—new "solutions" for transition metal catalysis. *Angew. Chem. Int. Ed.*, 39:3772–3789, 2000.

[217] P. Wasserscheid and T. Welton. *Ionic liquids in synthesis*. John Wiley & Sons, 2008.

[218] S. Weerasinghe and P. E. Smith. A kirkwood–buff derived force field for sodium chloride in water. *J. Chem. Phys.*, 119(21):11342–11349, 2003.

[219] F. Weigend and R. Ahlrichs. Balanced basis sets of split valence, triple zeta valence and quadruple zeta valence quality for h to rn: Design and assessment of accuracy. *Phys. Chem. Chem. Phys.*, 7:3297–305, 2005.

[220] J. A. WidegranLaesecke and J. W. Magee. The effect of dissolved water on the viscosities of hydrophobic room-temperature ionic liquids. *Chem. Commun.*, pages 1610–1612, 2005.

[221] J. A. Widegren, A. Laesecke, and J. W. Magee. The effect of dissolved water on the viscosities of hydrophobic room-temperature ionic liquids. *Chem. Commun.*, pages 1610–1612, 2005.

[222] J. A. Widegren, A. Laeseckea, and J. W. Magee. The effect of dissolved water on the viscosities of hydrophobic room-temperature ionic liquids. *Chem. Commun.*, page 1610, 2005.

[223] J. A. Widegrena, E. M. Saurerb, K. N. Marshc, and J. W. Mageea. Electrolytic conductivity of four imidazolium-based room-temperature ionic liquids and the effect of a water impurity. *J. Chem. Thermodynamics*, 37:569–575, 2005.

[224] J. S. Wilkes and M. J. Zaworotko. Air and water stable 1-ethyl-3-methylimidazolium based ionic liquids. *J. Chem. Soc., Chem. Commun.*, 0:965–967, 1992.

[225] X. Wu, Z. Liu, S. Huang, and W. Wang. Molecular dynamics simulation of room-temperature ionic liquid mixture of [bmim][bf_4] and acetonitrile by a refined force field. *Phys. Chem. Chem. Phys.*, 7(14):2771–2779, 2005.

[226] Z. Yan, S. V. Buldyrev, and H. E. Stanley. Relation of water anomalies to the excess entropy. *Phys. Rev. E*, 78(5):051201, 2008.

[227] I.-C. Yeh and M. L. Berkowitz. Ewald summation for systems with slab geometry. *J. Chem. Phys.*, 111(7):11780–11792, 1999.

[228] A. Yochelis, M. B. Singh, and I. Visoly-Fisher. Coupling bulk and near-electrode interfacial nanostructuring in ionic liquids. *Chem. Mater.*, 27:4169–4179, 2015.

[229] C. Yu and J. He. Synergetic catalytic effects in confined spaces. *Chem. Comm.*, 48:4933–4940, 2012.

[230] A. A. K. Zachary A.H. Goodwin. Underscreening, overscreening and double-layer capacitance. *Electrochemistry Communications*, 82:129–133, 2017.

[231] F. Zaera. Probing liquid/solid interfaces at the molecular level. *Chem. Rev.*, 112:2920–2986, 2012.

[232] S. Zahn, K. Wendler, L. Delle Site, and B. Kirchner. Depolarization of water in protic ionic liquids. *Phys. Chem. Chem. Phys.*, 13(33):15083–15093, 2011.

[233] N. Zhang, W. Li, C. Chen, and J. Zuo. Molecular dynamics simulation of aggregation in dimethyl sulfoxide–water binary mixture. *Comput. Theo. Chem.*, 1017:126–135, 2013.

[234] H. Zhao. Protein stabilization and enzyme activation in ionic liquids: specific ion effects. *J. Chem. Technol. Biotechnol.*, 91:25–50, 2015.

[235] Y. Zhao, J. Wang, H. Wang, Z. Li, X. Liu, and S. Zhang. Is there any preferential interaction of ions of ionic liquids with dmso and h20? a comparative study from md simulation. *The Journal of Physical Chemistry B*, 119(22):6686–6695, 2015. PMID: 25970011.

[236] F. Ziegler, J. Teske, I. Elser, M. Dyballa, W. Frey, H. Kraus, N. Hansen, J. Rybka, U. Tallarek, and M. R. Buchmeiser. Olefin Metathesis in Confined Geometries: A Biomimetic Approach toward Selective Macrocyclization. *J. Am. Chem. Soc.*, 141(48):19014–19022, Dec. 2019.